Sunyaev-Zel'dovich Observations Using Large-Format Millimeter Arrays

Thesis by

Nicole G. Czakon

In Partial Fulfillment of the Requirements

for the Degree of

Doctor of Philosophy

California Institute of Technology

Pasadena, California

2013

(Defended May 17, 2013)

This thesis is dedicated to my family:

To Dad, for instilling in me the love of knowledge.

To Mom, for teaching me how to be practical.

To Winston, for introducing me to the world of sports, legos, and home-made

flamethrowers.

To Tippy, for showing me that girls could climb trees, mow lawns, and win arguments.

To Christina, for making me grow up and for keeping me young.

iv

Acknowledgements

The work presented here would never have been possible without the inspirational and selfless leadership of my advisor Sunil Golwala. I am genuinely appreciative of his encouragement and support in everything I have pursued. Even at Caltech, where exceptionalism quickly becomes routine, Sunil's ability to manage all the various technical aspects of a submillimeter camera project is rare. I would also like to thank Jonas Zmuidzinas for his wisdom and knowledge of all things detectors. Jonas inspired me to join the group after giving a talk at JPL on a new kind of submillimeter detector, the millimeter-wave kinetic inductance detector (MKID). There is not enough I could say about Jack Sayers to merit the gratitude I feel to him for holding the beacon for the analysis presented in this thesis. He and Sunil laid the instrumentational, observational, and analysis groundwork, from which I built my analysis.

There are several people that I would like to thank for teaching me the ropes in the lab and for providing the motivational support through the seemingly never-ending Helium fills. Everyone has been (for the most part) genuinely helpful. I am grateful to James Schlaerth for his patience in answering all of my stupid questions and for always being in his office when I called. I am indebted to Tasos Vayonakis for teaching me cryogenics and submillimeter instrumentation. I must also thank both James and Tasos for making Democam purr like a kitten so that when I worked with it, I could spend more of my time testing MKIDs and less time trouble-shooting cryogenic problems. I would like to thank Matt Hollister for always being available for a little chat, and for his encyclopedic knowledge of all things cryogenic. Seth, thanks for taking over the lab work so that I could pursue analysis. I can't wait to see that first MUSIC cluster image!

Starting in late 2010, my thesis project became predominantly observational in nature.

Abstract

Galaxy clusters are the largest gravitationally bound objects in the observable universe, and they are formed from the largest perturbations of the primordial matter power spectrum. During initial cluster collapse, matter is accelerated to supersonic velocities, and the baryonic component is heated as it passes through accretion shocks. This process stabilizes when the pressure of the bound matter prevents further gravitational collapse. Galaxy clusters are useful cosmological probes, because their formation progressively freezes out at the epoch when dark energy begins to dominate the expansion and energy density of the universe. A diverse set of observables, from radio through X-ray wavelengths, are sourced from galaxy clusters, and this is useful for self-calibration. The distributions of these observables trace a cluster's dark matter halo, which represents more than 80% of the cluster's gravitational potential. One such observable is the Sunyaev-Zel'dovich effect (SZE), which results when the ionized intercluster medium blueshifts the cosmic microwave background via Compton scattering. Great technical advances in the last several decades have made regular observation of the SZE possible. Resolved SZE science, such as is explored in this analysis, has benefitted from the construction of large-format camera arrays consisting of highly sensitive millimeter-wave detectors, such as *Bolocam*. *Bolocam* is a submillimeter camera, sensitive to 140 GHz and 268 GHz radiation, located at one of the best observing sites in the world: the Caltech Submillimeter Observatory on Mauna Kea in Hawaii. *Bolocam* fielded 144 of the original spider web NTD bolometers used in an entire generation of ground-based, balloon-borne, and satellite-borne millimeter wave instrumention. Over approximately six years, our group at Caltech has developed a mature galaxy cluster observational program with *Bolocam*. This thesis describes the construction of the instrument's full cluster catalog: BOXSZ. Using this catalog, I have scaled the *Bolocam* SZE measurements with X-ray mass approximations in

an effort to characterize the SZE signal as a viable mass probe for cosmology. This work has confirmed the SZE to be a low-scatter tracer of cluster mass. The analysis has also revealed how sensitive the SZE-mass scaling is to small biases in the adopted mass approximation. Future *Bolocam* analysis efforts are set on resolving these discrepancies by approximating cluster mass jointly with different observational probes.

Contents

List of Figures

List of Tables

List of Constants

Physical Constants

Speed of Light	c	3.0×10^5 km/s
Boltzmann's Constant	k_B	8.6×10^{-5} eV/K
Proton Mass	m_p	1.67×10^{-24} g
Megaparsec	Mpc	3.09×10^7 km
Solar Mass	$M_\odot$	1.99×10^{30} kg
Gravitational Constant	G	4.302×10^{-9} Mpc/$M_\odot$(km/s)^2
Electronvolt	eV	1.602×10^{-19} J
Jansky	Jy	10^{-26} W/m^2/Hz
Hubble Constant	H_0	70 (km/s)/Mpc
Hubble Parameter	h	H_0/[100 (km/s)/Mpc] = 0.7
Hubble Distance	D_H	c/H_0 = 3.0h^{-1} Gpc = 4.3 Gpc
Cluster Temperature Unit	1 keV/k_B	11.6$\times 10^6$ Kelvin
Cluster Pressure Unit	keV/cm^3	1.6×10^{-10} pascals = 1.6×10^{-15} atm
Cluster Gas Density Unit	protons/cm^3	10^6 protons/ m^3
Present Density of the Universe	$\rho_{c,0}$	$\sim 10^{-29}$ g/cm^3 or $\sim 6m_p$/m^3
Typical atmospheric density (STP)	1.25kg/m^3	$\sim 10^{27} m_p$/m^3

Chapter 1

Cosmology

Galaxy clusters are fascinating objects because they exhibit so many cosmological phenomena. Following the Big Bang, quantum density flucutations seed the hierarchical accretion of matter, which leads to all large-scale structure formation. Galaxy clusters are the most massive end-products of this process, and their continued growth is prevented in the epoch when dark energy drives the accelerated expansion of the universe. Dark matter comprises more than 80% of the gravitationally bound cluster matter and dictates many of the physical properties of galaxy clusters. This section gives an overview of the salient aspects of cluster formation and the astrophysical processes which enable their observation.

1.1   To Make a Long Story Short...

In the first decades of the 20th century, Albert Einstein developed special relativity in response to curious inconsistencies in Maxwell's theory of electromagnetism in a given inertial reference frame[80]. He discovered that these inconsistencies can be resolved by setting the speed of light to be constant in all inertial reference frames and by treating time as a fourth dimension to create a 4-dimensional "distance," which is invariant with respect to a moving reference frame. Einstein, however, was bothered by his formulation of special relativity in that it did not adequately describe the equivalence of inertial mass and gravitational mass. He therefore generalized Maxwell's field equations to account for this via a curvature of space-time, which makes gravity a local phenomenon. The Russian physicist, Alexander Friedmann, discovered that the solution to Einstein's field equations allowed for either ex-

panding, contracting, or static space, and, by extension, universe[94]. Unsatisfied with this answer, Einstein added the cosmological constant to the field equations in order to force the universe into a static state:

$$R_{\mu\nu} - \frac{1}{2}g_{\mu\nu}R + g_{\mu\nu}\Lambda = \frac{8\pi G}{c^4}T_{\mu\nu}, \tag{1.1}$$

where the curvature of space is introduced via $R_{\mu\nu}$, the Ricci curvature tensor, and R, the scalar curvature. The stress-energy tensor, $T_{\mu\nu}$, represents matter and energy, which induces the curvature on the left-hand side of the equation. The term $g_{\mu\nu}$ is the metric, which characterizes the space-time parameters of a given reference frame. The G and c terms are the gravitational constant and the speed of light, respectively.

Although the initial observations confirming a non-static solution to Einstein's field equations (i.e., an expanding universe) are often attributed to Edwin Hubble, it was, in fact, the Belgian priest, Georges Lemaitre, who, as a graduate student in 1927, first proposed the concept and derived "Hubble's" law. In this work, he presented the first calculation of the "Hubble" constant based on observational data[155]. Lemaitre would eventually follow this idea all the way to its origin, formulating a theory of the "primeval atom"[156] which Fred Hoyle mockingly dubbed: "The Big Bang." Lemaitre also suggested that cosmic rays were left over fossils from the initial explosion. While Lemaitre was on to the right idea, the lack of alternative observational data led this idea to a dead end.[1] Einstein seemed resistant at first to Lemaitre's idea, but further observational studies conducted by Edwin Hubble in 1929 [123] confirmed of the expansion of the universe and led Einstein to recant and call his cosmological constant kludge his "biggest blunder."

Another major milestone in the theory of an expanding universe was made in 1948, when Alpher et al. [7] noted that the relative observed abundances of light elements could be explained via the mechanism of an expanding universe. This is known as Big-Bang nucleosynthesis (BBN). In 1965 Dicke et al. [67] continued the investigation into this theory and considered the point at which an expanding universe would sufficiently cool to allow neutral

---

[1]Interestingly, unambiguous observational evidence of the precise origin of cosmic rays has become available only very recently from observations using the VERITAS[11] and Fermi [3] telescopes, which confirm that cosmic ray particles originate from supernovae remnants.

hydrogen to form (recombination). At this point, blackbody radiation would decouple and provide an observable relic of the "primordial fireball." Dicke initiated the development of a telescope to search for the relic blackbody radiation of the recombination process. During this process, however, he received a phone call from Arno Penzias and Robert Wilson about a mysterious noise measured with their eponymous Dicke radiometer[293]. Dicke knew that this was exactly the Cosmic Background Radiation (CMB) that he was searching for. While the Penzias and Wilson result gives only one data point at 4 GHz, a 3 Kelvin blackbody peaks at about 160 GHz. The COsmic Background Explorer (COBE), launched in 1989, measured the full spectrum of the CMB at 34 equally-spaced frequencies, using the Far-InfraRed Absolute Spectrophotometer (FIRAS). Mather et al. [173] and Fixsen & Mather [90] use this data to confirm the CMB as the most perfect black body ever measured in nature—deviating by less than 50 parts per million from a perfect 2.725 ± 0.001 K black body between ∼60-600 GHz.[2] This result is consistent with the Big Bang model, because it indicates that at some point the universe was dense enough to be filled uniformly with thermalized matter. As will soon be demonstrated, the CMB provides much more information about the early universe than this.

If the universe began as a primordial fireball, there must have been a quantum mechanical noise mechanism, which, at some point, broke the translational symmetry of matter to allow structure formation. Andrei Sakharov [249] predicted in 1966 that adiabatic compression would be opposed by the associated increase in the plasma pressure and generate acoustic waves. The hot (compressed) regions and the cold (rarefied) regions would imprint themselves accordingly on the temperature of CMB. This concept was further developed in 1970 by Sunyaev & Zel'dovich [270] and independently by Peebles & Yu [215] in the same year. After FIRAS' liquid Helium supply ran out, COBE's Differential Microwave Radiometer (DMR) experiment continued to the map the sky for another three years at 31.5 GHz, 53 GHz, and 90 GHz. The differential measurement removed all common signal, and Bennett et al. [22] confirmed $36 \pm 5\mu$K temperature fluctuations when the maps were smoothed to 7

---

[2]Fixsen et al. [91] recently report an excess of tens of mK in the ∼1-10 GHz region of the CMB spectrum using measurements from the Absolute Radiometer for Cosmology, Astrophysics and Diffuse Emission (ARCADE 2.) The physical origin of this radiation is still unknown (e.g., Ysard & Lagache [299], Holder [120]).
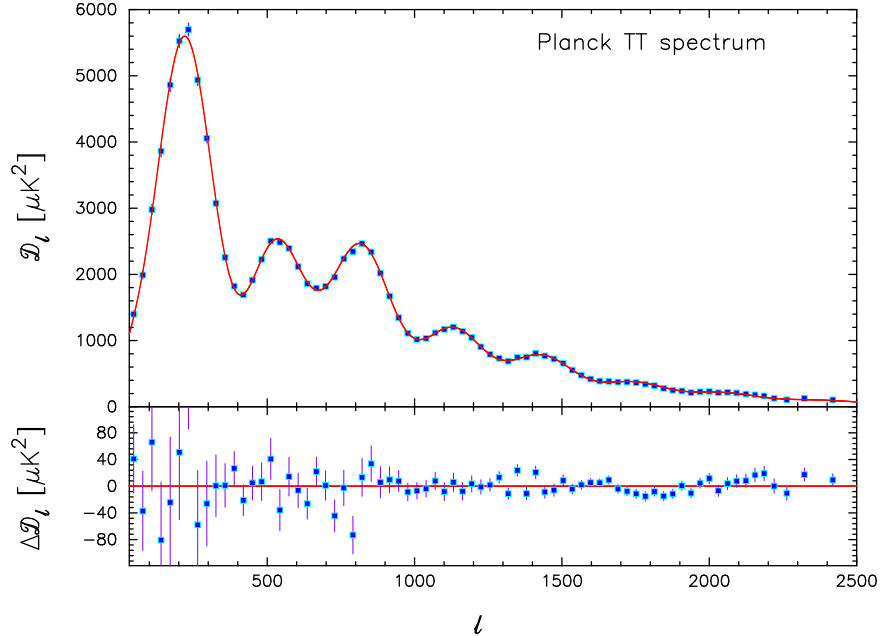
Figure 1.1 The temperature angular power spectrum of the CMB measured by Planck Collaboration et al. [226]. The red curve represents the best-fit spectrum to the data points, using the standard cosmological model with cold dark matter and a cosmological constant (ΛCDM), and is further described in the text. The bottom figure shows the residuals of the data with the model. Figure taken from Planck Collaboration et al. [226].

(angular) degrees.

At recombination, fluctuations in the CMB will peak at half-wavelength harmonics of an acoustic compression-rarefraction cycle. These are known as the acoustic peaks, and the scale at which they occur is set by the speed of sound. The observed angular separation of two points separated by a given physical scale, however, depends on the curvature of space and distance through which the signal travels. Two CMB Balloon experiments, BOOMERANG [63] and MAXIMA [110], unambiguously measured the position of the lowest-order acoustic peak, and, by combining this with new measurements of the Hubble constant using the Hubble Space Telescope (Freedman [93]), confirmed that space is flat to within a few percent. The recent measurement of the CMB by the Planck Collaboration [226] is presented in Figure 1.1. In combination with auxiliary cosmological data, Planck Collaboration et al. [226] confirm that space is flat to less than seven tenths of a percentile. The CMB contains much more information that is beyond the scope of this thesis, and for a well-presented review of all of these processes, see Hu & Dodelson [122].

At about the same time that the CMB community discovered that the universe is flat, two teams, one led by Saul Perlmutter [217] and the other by Adam Riess and Brian Schmidt [243] discovered that supernovae (with well-defined luminosities) are accelerating away at a faster rate than expected. These observations can be made consistent with the observed flatness of the universe by setting the cosmological constant term in Einstein's field equations 1.1 to a non-zero value. Perhaps Einstein's initial hunch was correct after all. The observed expansion is driven by an unknown source of energy density, and it has therefore been named dark energy. While a cosmological constant is the simplest model that consistently describes all observations, it does not intrinsically emerge from current theory, and therefore several alternative dark-energy models have been proposed (e.g. Copeland et al. [60], Gott & Slepian [103]), which have yet to be confirmed.

While the precision to which scientists understand the origin and evolution of the universe is astounding, many questions remain. Why exactly is the universe flat? How can temperature patches in the sky be in phase with each other when they should have no causal relation due to the amount of time needed for this information to travel at such scales? Alan Guth [108] proposed the theory of inflation in 1981 as a physical mechanism that consistently describes these various observations. This theory maintains that shortly after the Big Bang, there was a rapid period of expansion, which smoothed spatial curvature and provided a mechanism for distant regions of the sky to be causally connected. Furthermore, inflation provides the mechanism that gives rise to the quantum fluctuations, and it also accounts for the curious fact that all the modes seem to have originated in phase with each other.

Inflation is the proposed mechanism that seeds the quantum fluctuations in the matter density field and leads to all subsequent structure formation. The initial growth of these density perturbations, however, is inhibited by radiation pressure in the high-density environment of the early stages of the universe. As photons redshift under expansion, the radiation density falls more rapidly than the matter density, and when the universe is about one hundred thousand years old, matter begins to dominate. Density perturbations start to spend a larger fraction of time in a compressed versus rarefied state. When the universe is about four hundred thousand years old, radiation decouples completely, and the speed of sound plummets. Overdense regions will begin to collapse in on themselves when they

reach the Jeans instability, i.e., when the enclosed matter no longer has sufficient time to compressionally resist gravitational infall. The infalling matter is accelerated supersonically to thousands of kilometers per second and undergoes an accretion shock. Subsequent ram pressure converts most of the kinetic energy into thermal energy and mixes the phases of the kinetic motion of the gas, via a process called violent relaxation, and homogenizes the gas. A bound, virialized, system will stabilize to the state where the potential energy equals twice the kinetic energy. Individual virialized systems continue to grow through hierarchical structure formation both by the accretion of unbound matter, as well as merging with other virialized systems.

Galaxy clusters represent the most massive structures to have virialized through the hierarchical structure formation scenario. Their total mass can be between approximately 10^{13} and 10^{15} solar masses. It takes several Gigayears for a galaxy cluster to get so large, and its continued growth is prevented as the universe accelerates its expansion in an epoch dominated by dark energy. As the name implies, galaxy clusters contain large concentrations of galaxies, the observation of which led to their initial discovery. The nomenclature is slightly misrepresentative, considering that stars represent $\lesssim 3\%$ of all matter within a galaxy cluster. Ionized gaseous normal matter, the intercluster medium (ICM), constitutes another $\sim 17\%$, and the remaining $\sim 80\%$ of the matter density is called dark matter, because it seems to couple to normal matter gravitationally but otherwise emits no observational signal. Normal matter is also commonly called baryonic matter, because it is composed primarily of neutrons and protons.

Dark matter was proposed in the early 1930s to account for the fact that the observed orbital velocities of stars in the Milky Way (Oort [208]) and of galaxies in the Coma cluster (Zwicky [307]) implied a larger gravitational potential than could be observed. More recent observations of supersonic galaxy cluster collisions, such as of the Bullet Cluster, indicate that while baryonic matter will form a bow shock during such collisions, dark matter passes through relatively undisturbed (Markevitch et al. [168]). While the exact nature of dark matter is still unknown, observations support the idea that it is a non-relativisitc (cold), massive particle which couples only gravitationally to both baryonic matter and itself. Physically-motivated extensions to this basic dark matter model have been proposed, which predict

weak non-gravitational coupling to baryonic matter (Jungman et al. [134], Bertone et al. [27]). Detecting the signature of this coupling (either directly or indirectly) is an extremely active area of research (e.g. Bernabei et al. [26], Ahmed et al. [4], Angloher et al. [9], Cholis et al. [56]).

Cosmologists have now converged on a standard cosmological model, ΛCDM, which contains four primary energy components: baryonic matter, cold dark matter, radiation, and dark energy. The sum of this energy at all times implies a flat universal geometry. The observable universe arose from a singularity, called the Big Bang, approximately 13.7 billion years ago. This event was followed by a period of rapid expansion, known as inflation, followed by a period of continued expansion and large-scale structure formation. At the present time, $\sim$5% of the energy in the universe is baryonic in nature, and $\sim$ 25% of the energy in the universe couples to baryonic matter solely through gravity. The remaining $\sim$70% of the energy density remains constant with volume, fueling the current epoch of accelerated cosmic expansion. This model has withstood rigorous observational cross-examination, but it leaves many open questions as to its physical origin.

Galaxy cluster formation is strongly affected by the nature of dark energy and dark matter, and therefore it is a promising cosmological probe. The possible evolution of dark energy as a function of time can be determined by measuring the number of clusters within a certain mass range as a function of time (Hasselfield et al. [113], Benson et al. [25], Planck Collaboration et al. [228]). The radial scaling of an individual cluster's mass concentration can also give insight into the nature of dark matter (Spergel & Steinhardt [264], Peter et al. [218]). For these to be viable cosmological methods, however, scientists must ensure that measured observables accurately describe the total matter content.

The two cluster observables studied in this thesis are generated directly from the ICM. The ICM is heated to millions of degrees Kelvin, primarily via shock-heating during the initial accretion of matter. As a point of comparison, stars themselves are only several thousands of Kelvin. High-velocity free electrons are deflected by the more massive protons and are slowed via the emission of bremsstrahlung radiation, making galaxy clusters extremely luminous $\sim 10^{43} - 10^{45}$erg/s. A solar luminosity, in comparison, is about 4×10^{33}erg/s and the typical peak supernova luminosity is about 10^{42}erg/s.

The ICM produces a second observable as free electrons distort the spectrum of the CMB via Compton scattering. The exact spectral distortion of the CMB during this process was calculated by two Russian scientists in the 1970s and is eponymously named the Sunyaev-Zel'dovich effect (SZE) ([270, 271]). Under the appropriate conditions, cluster masses can be derived from these observables by applying the equation of hydrostatic equilibrium to the measured pressure profiles. The assumption of hydrostatic equilibrium, however, breaks down for most cluster scenarios and alternative, more robust, mass proxies must be developed and observationally confirmed. The calibration of cluster masses from the SZE signal for cosmology is the topic of the analysis presented in this thesis.

1.2 Distance Measures

Distance is an important concept in cosmology. For a monotonically expanding universe, distance also serves as the cosmological time piece. The dark energy equation of state, for example, can be constrained by counting the number of clusters of a specific mass as a function of distance. Given a particular cosmology, the general conditions in which clusters form is also a function of distance. Furthermore, an accurate distance measure is needed to obtain physical cluster properties from the measured flux of a given observable. The concept of distance, however, is made ambiguous in an expanding reference frame, where general relativity dictates that the distance that a photon travels between two points is not the same as the final physical distance between those two points. Carroll [50] and Hogg [119] give very good overviews of distance measures, and this section briefly introduces the concepts that will become relevant later on.

From special relativity, the invariant distance measure between two points is given by:

$$ds^2 = \sum_{\mu,\nu} g_{\mu\nu} dx^\mu dx^\nu = g_{\mu\nu} dx^\mu dx^\nu. \tag{1.2}$$

Here, μ and ν are indices representing a particlar dimension: either one of the three space dimensions or the time dimension, which is converted to a distance by multiplying it by the speed of light. Einstein's summing convention is introduced in the last term, where repeated

indices for a particular product represent a sum over all indices. The $g_{\mu\nu}$ term is called the metric, and it describes exactly how the four different dimensions should be combined to form the invariant. A popular form of this term is the Minkowski metric, which describes flat spacetime in the absence of matter:

$$g_{\mu\nu} = \eta_{\mu\nu} = \begin{bmatrix} 1 & 0 & 0 & 0 \\ 0 & -1 & 0 & 0 \\ 0 & 0 & -1 & 0 \\ 0 & 0 & 0 & -1 \end{bmatrix}. \tag{1.3}$$

The Robertson-Walker metric reformulates the invariant in equation 1.2 for ΛCDM cosmology and accounts for an expanding reference frame. By multiplying the distance elements by a scale parameter, $a(t)$, and going into a spherical coordinate system, one obtains:

$$ds^2 = -dt^2 + a^2(t)\left[d\chi^2 + S_k^2(\chi)d\Omega^2\right], \tag{1.4}$$

where $d\chi$ is the comoving distance measure, which is normalized to remain constant for any cosmological scenario. The curvature of space affects the non-radial components of the invariant as:

$$S_k(\chi) \equiv \begin{cases} \sin(\chi), & k = +1 \\ \chi, & k = 0 \\ \sinh(\chi), & k = -1. \end{cases} \tag{1.5}$$

Where $k = -1$ corresponds to constant negative curvature (open) , $k = 0$, corresponds to no curvature (flat), and $k = +1$ corresponds to positive curvature (closed). In light of overwhelming observational evidence discussed in the previous chapter, it is sufficient for the present analysis to assume that space is flat, $k = 0$, and Equation 1.4 simplifies to:

$$ds^2 = -dt^2 + a^2(t)\left[d\chi^2 + \chi^2 d\Omega^2\right]. \tag{1.6}$$

The scale parameter can be reformulated using the Doppler redshift, z, of an observed

signal emitted from a receding source:

$$\frac{a(z)}{a_0} = \frac{1}{1+z}. \tag{1.7}$$

Most cosmological parameters with the subscript "0" refer to a parameter's value in the present time. Therefore, a_0 refers to the current scale of the universe. A good mnemonic for remembering the redshift formula is by noting that the universe was half the current size at $z = 1$.

This leads to the formula for the Hubble parameter, which describes the relative rate at which, the universe is expanding as a function of redshift:

$$H(z) = \frac{\dot{a}(z)}{a(z)} = H_0 E(z), \tag{1.8}$$

where the overdot signifies the time derivative and H_0 the Hubble constant. The Hubble distance unit, D_H, can be derived from the Hubble constant, first, by inverting it and obtaining a unit of time (the Hubble time) and then multiplying this by the speed of light:

$$D_H \equiv \frac{c}{H_0}. \tag{1.9}$$

Using the framework of an expanding reference frame, the mechanism for this expansion, which is derived from Einstein's field equations in Equation 1.1, is explored. Solving Einstein's field equations using the Roberston-Walker metric for a flat universe yields the Friedmann equations, one of which is:

$$H(z)^2 \equiv \left(\frac{\dot{a}(z)}{a(z)}\right)^2 = \frac{8\pi G \rho(z)}{3} \tag{1.10}$$

$$\rho_c(z) \equiv \rho(z) = \frac{3H(z)^2}{8\pi G} = \frac{3H_0^2 E(z)^2}{8\pi G}, \tag{1.11}$$

where, in the last step, the equation is re-arranged to solve for ρ, the energy density, which is equivalent to the critical density, $\rho_c(z)$, for a flat universe. This result demonstrates how the relative rate of expansion scales with the local energy density. In the epoch relevant to galaxy cluster formation, the evolution of the Hubble parameter, $E(z)$, can be calculated by

summing the relative energy densities of (total) matter, Ω_M, and dark energy, Ω_Λ in a flat universe:

$$E(z)^2 = \Omega_M(1+z)^3 + \Omega_\Lambda = \Omega_M \frac{a_0^3}{a^3} + \Omega_\Lambda. \tag{1.12}$$

Equation 1.12 explicitly demonstrates how each form of energy evolves differently: matter dilutes with volume, and dark energy remains constant.

The comoving distance, D_C, can then be calculated by setting the geodesic in Equation 1.6 to null and integrating to find the expansion-invariant parameter, χ:

$$0 = ds^2 = -dt^2 + a^2 d\chi^2 \tag{1.13}$$

$$\chi = \int \frac{dt}{a} = \int \frac{da}{a^2 H(a)} \tag{1.14}$$

$$D_C \equiv D_H \int_0^z \frac{dz'}{E(z')}. \tag{1.15}$$

Luminosity distance then becomes the comoving distance, D_C, multiplied by the scale factor:

$$D_L = (1+z)D_C. \tag{1.16}$$

The angular diameter distance, D_A, is the ratio of the physical transverse size corresponding to an observed angular size in radians. For a flat universe:

$$D_A = \frac{D_C}{1+z}. \tag{1.17}$$

A comoving volume can then be obtained from these distance measures and is extremely important for cosmological surveys. The basic element is simple: multiply the comoving differential area by the comoving thickness of the volume:

$$dV_c = D_C^2 d\Omega dD_c = \frac{D_H(1+z)^2 D_A^2 d\Omega dz}{E(z)}, \tag{1.18}$$

where, in the right-hand side, the comoving parameters have been converted to physical parameters using Equations 1.15 and 1.17.

What are the typical scales of these distance measurements? The work-horse distance

unit in astronomy is the parsec, which is 3.086×10^{18}cm, or 3.26 light years. This is the distance an object must be from the Earth for an observer to perceive it to shift by one arcsecond as the Earth travels one AU perpendicular to the axis between the sun and the object. A parsec is about 10,000 times the distance from the Sun to Neptune, the most distant planet in the solar system, or, the approximate distance to our nearest star, *Proxima Centauri*. A galaxy is approximately tens of kpc in size, a galaxy cluster is about a Mpc, and the observable universe is approximately 14 Gpc.

1.3 Structure Formation

This section provides a general overview of structure formation and the reader is referred to Peebles [214], Peacock [213] for a more comprehensive introduction to the subject. The growth of the initial density perturbations can, to first order, be treated as an ideal fluid. Let δ represent the size of a density perturbation relative to a homogeneous background density, ρ_0:

$$\delta(\mathbf{x,t}) = \frac{\rho(\mathbf{x,t}) - \rho_0}{\rho_0}. \tag{1.19}$$

For the vanilla ΛCDM cosmology, δ is scale-independent, and this implies that the space and time components can be solved independently. The spatial-dependence of the disturbance can be expanded into plane waves, $\delta \propto \exp(-i\mathbf{k} \cdot \mathbf{x})$, where $\mathbf{k}$ is a comoving wavevector. By invoking the continuity equation (conservation of mass), the Euler equation (conservation of momentum), and the Poisson equation, the time dependence of δ can be formulated as a familiar-looking second-order differential equation:

$$\ddot{\delta} + 2\frac{\dot{a}}{a}\dot{\delta} = \delta \left(4\pi G \rho_0 - \frac{c_s^2 k^2}{a^2} \right), \tag{1.20}$$

where G is the gravitational constant and c_s is the speed of sound (Peebles Equation 16.4, Peacock Equation 15.21). The second term on the left-hand side is a friction-like term, which prevents the growth of perturbations. The perturbation is allowed to grow via gravitational collapse when the term on the right-hand side is greater than zero, which is when

its wavelength reaches the Jeans scale:

$$\lambda_J = c_s \left(\frac{\pi}{G\rho} \right)^{1/2}. \tag{1.21}$$

The existence of massive neutrinos, which were first observed by Fukuda et al. [95] with SuperKamiokande in 1998, and the possibility of warm dark matter complicate the situation (Bond et al. [39]). Matter perturbations grow more slowly, since the Jeans scale of neutrinos and warm dark matter remains significant after recombination (Bond & Szalay [40]). This couples the spatial and time components, and the evolution of the particle fluid is determined from a set of coupled Boltzmann equations, which can only be traced via simulation (Eisenstein & Hu [81]). The ansatz to Equation 1.20 consists of both a growing mode and a decaying mode with separable spatial and time-dependent components:

$$\delta(\mathbf{x}, t) = A(\mathbf{x})D_1(t) + B(\mathbf{x})D_2(t). \tag{1.22}$$

Substituting Equation 1.22 back into Equation 1.20 and solving for D_1 in a flat universe with a non-zero cosmological constant yields:

$$D_1(z) = \frac{H(z)}{H_0} \frac{\int_z^\infty \frac{dz'(1+z')}{H^3(z')}}{\int_0^\infty \frac{dz'(1+z')}{H^3(z')}}, \tag{1.23}$$

where the term in the denominator is simply a normalization factor so $D_1 = 0$ at $z = 0$. An approximate solution to $D_1(z)$ follows from Lahav et al. [149], Lightman & Schechter [159]:

$$D_1(z) \approx (1+z)^{-1} \frac{5\Omega(z)}{2} \left\{ \Omega(z)^{4/7} - \Omega_\Lambda(z) + \left[1 + \frac{\Omega(z)}{2} \right] \left[1 + \frac{\Omega_\Lambda(z)}{70} \right] \right\}^{-1}. \tag{1.24}$$

Expressing density fluctuations, individual Fourier space gives:

$$\delta_{\mathbf{k}}(k) = \int \delta(\mathbf{x}) \exp(i\mathbf{k}\cdot\mathbf{x}) d^3 x. \tag{1.25}$$

The power spectrum can then be obtained by taking the magnitude-squared of these fluctu-

ations.

$$P(k) \equiv \langle |\delta_k|^2 \rangle \tag{1.26}$$

If δ is a Gaussian random field, then $P(k)$ is a complete statistical description of the perturbation power spectrum. By smoothing these perturbations with the Fourier transform of a spherical top-hat function, $W_k(R)$, of a characteristic size, R, one can characterize the magnitude of perturbations at different scales:

$$\sigma_R^2 \equiv \langle |\delta M/M|^2 \rangle = \frac{1}{(2\pi)^3} \int P(k) |W_k(R)|^2 d^3 k. \tag{1.27}$$

The variance of the matter power spectrum, σ_R^2, is a popular parameter to describe large-scale structure formation, particularly for an $8h^{-1}$ Mpc-sized top-hat, σ_8. As σ is a monotonic function with M, it is often used as a proxy for M, particularly in non-observational work since it can be made relatively independent of cosmology. The purest analytical method to calculate the spectrum of density fluctuations, would be to start with a given $P(k)$ (which is measured beautifully from the CMB) and relate this to the present time using the matter transfer function:

$$T(k,z) \equiv \frac{\delta(k,z)}{\delta(k, z = \infty)} \frac{\delta(0, z = \infty)}{\delta(0, z)}. \tag{1.28}$$

If the growth of structure is scale-independent $(T(k,z) = T(z))$, the spatial component of the growing mode can be related back to σ as:

$$\sigma(M,z) = \sigma(M,0)T(z) = \sigma(M,0)\frac{D_1(z)}{D_1(0)} = \sigma(M,0)\frac{G(z)}{(1+z)G(0)}, \tag{1.29}$$

and the growth function, $G(z) \propto (1+z)D_1(z)$, is introduced in the right-hand equation.

For the present analysis, a local, cluster-based, empirical approximation for $\sigma(M,z)$ is adopted from Stanek et al. [266]. Specifically, using the measured luminosities of galaxy clusters, they calculate $\sigma(M,0)$ to be accurately described with the equation:

$$\ln \sigma = s_0 + s_1 \ln M + s_2 \ln M^2, \tag{1.30}$$

where $[s_0, s_1, s_2] = [0.468, 0.267, 0.0123]$ at $\Omega_m = 0.24$. The normalization of σ is convention-
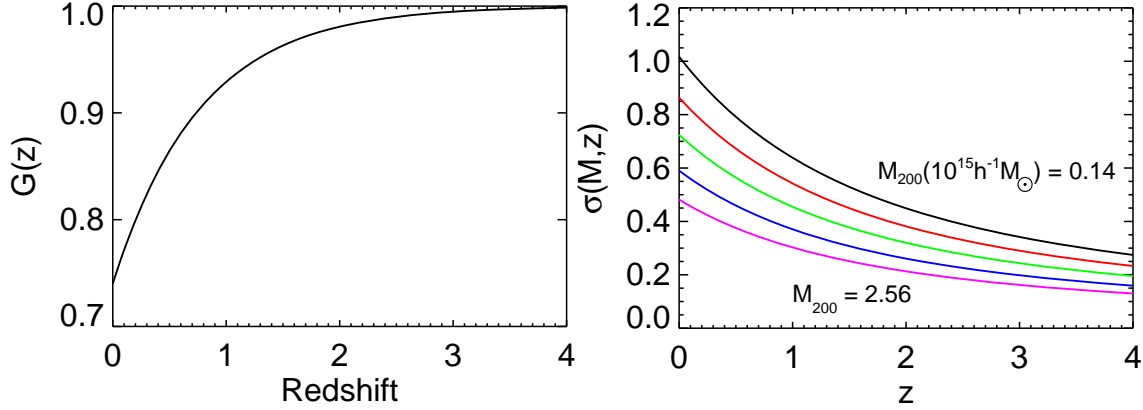
Figure 1.2 Left: The growth of structure in the universe with redshift. Note the slowing growth of structure as the universe expands. Right: The variance of the matter power spectrum with redshift. The mass values, M, indicate the mean enclosed mass for a top-hat of a particular size. The relative value of σ indicates the relative abundance of clustering of a particular size.

ally scaled using σ_8. There is plenty of uncertainty in what the exact value of σ_8 is, partially because our ability to accurately determine cluster mass is limited. The redshift-dependence of the growth function and σ is plotted in figure 1.2.

1.4   Mass Function

The growing perturbations collapse when their density contrast,$\delta = \delta\rho/\rho$, exceeds a critical threshold δ_c. In 1974 Press & Schechter [238, hereafter PS] propose a simple method in which to calculate the mass function, or, the number of clusters of a particular mass within a particular volume. Starting with the variance of the matter power spectrum, $\sigma^2(M, z)$, PS estimate that the probability that a region of mass M exceeds the collapse threshold at redshift z is erfc$[\delta_c/\sqrt{2}\sigma(M, z)]$. The number density of such perturbations follows by dividing by the mean comoving density of a characteristic background mass, M:

$$n(M, z) = \frac{\Omega_M \rho_{cr0}}{M}\text{erfc}\left[\frac{\delta_c}{\sqrt{2}\sigma(M, z)}\right].$$

(1.31)

The differential mass function then takes the form:

$$\frac{dn(M,z)}{d\ln\sigma^{-1}} = \sqrt{\frac{2}{\pi}}\frac{\Omega_M\rho_{cr0}}{M}\frac{\delta_c}{\sigma}\exp\left[-\frac{\delta_c^2}{2\sigma^2}\right].$$ (1.32)

The PS mass function, while qualitatively correct, disagrees in detail with the results of N-body simulations. Specifically, the PS formula overestimates the abundance of haloes near the characteristic mass M, and it underestimates the abundance in the high-mass tail. Over the subsequent decades, this mass function has been tweaked by running more complex simulations, for example, by allowing for elliptical collapse (Jenkins et al. [129]). Currently, a commonly adopted form of the mass-function is the one proposed by Tinker et al. [273] and depicted together with the PS mass function in figure 1.3:

$$\frac{dn(M,z)}{dM} = f(\sigma)\frac{\overline{\rho}_m(z)}{M}\frac{d\ln\sigma^{-1}}{dM},$$ (1.33)

where

$$f(\sigma) = A\left[\left(\frac{\sigma}{b}\right)^{-a} + 1\right]e^{-c/\sigma^2},$$ (1.34)

and $f(\sigma)$ is the mass function. The variance in the matter power spectrum is again given by σ, $\overline{\rho}_m(z)$ represents the mean matter density at the redshift of the cluster, and dn/dM represents the number of clusters per unit volume with masses between $[M, M + dM]$ and redshifts, $[z, z + dz]$. The original simulations presented in Tinker et al. [273] suggest that $f(\sigma)$ evolves with redshift, but in a follow-up study, Tinker et al. [274] dispute this result. The present analysis will therefore assume that the mass function does not evolve with redshift.

Using Equation 1.18 for dV/dz, one obtains the expected number of halos contained within a specific survey volume:

$$\frac{d^2N}{dMdz} = f(\sigma)\frac{\overline{\rho}_m(z)}{M}\frac{d\ln\sigma^{-1}}{dM}\frac{dV}{dz}.$$ (1.35)

This formula will become particularly relevant in later chapters when I attempt to char-
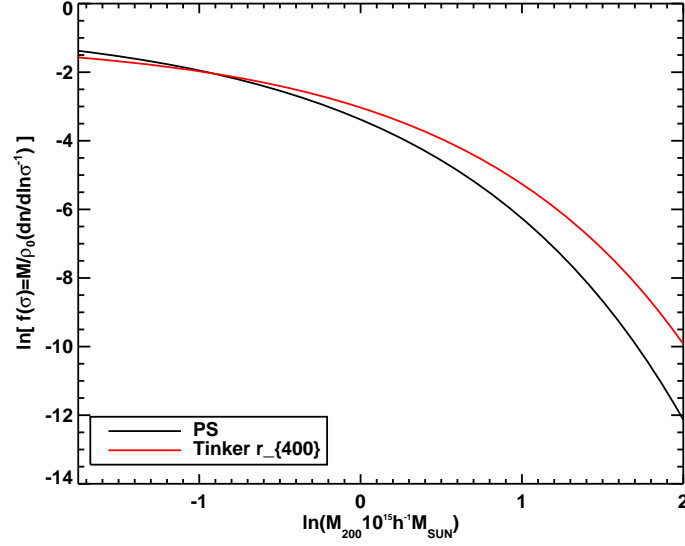
Figure 1.3 The Press & Schechter [238] mass function compared with the Tinker et al. [273] mass function for an overdensity 400 times the matter denstiy at the observed redshift. M is related to σ using Equation 1.30 via Stanek et al. [266].

acterize how our observed cluster sample compares with a given theoretical distribution of cluster observables. Figure 1.4 shows the redshift evolution of iso-mass contours. Note that while the number density for clusters of a particular mass decreases with redshift, the number of observable clusters of a particular mass remains relatively constant since the observable volume also increases with redshift.

Throughout this analysis, I adhere to the convention of calculating cluster properties within a constant, r_Δ, the radius within which the mean cluster density is Δ times the critical density, $\rho_c(z)$, of the universe at the redshift of the cluster. I also assume ΛCDM cosmology, and set $H_0 = 70$ km s^{-1}Mpc^{-1}, $\Omega_M = 0.3$, and $\Omega_\Lambda = 0.7$.
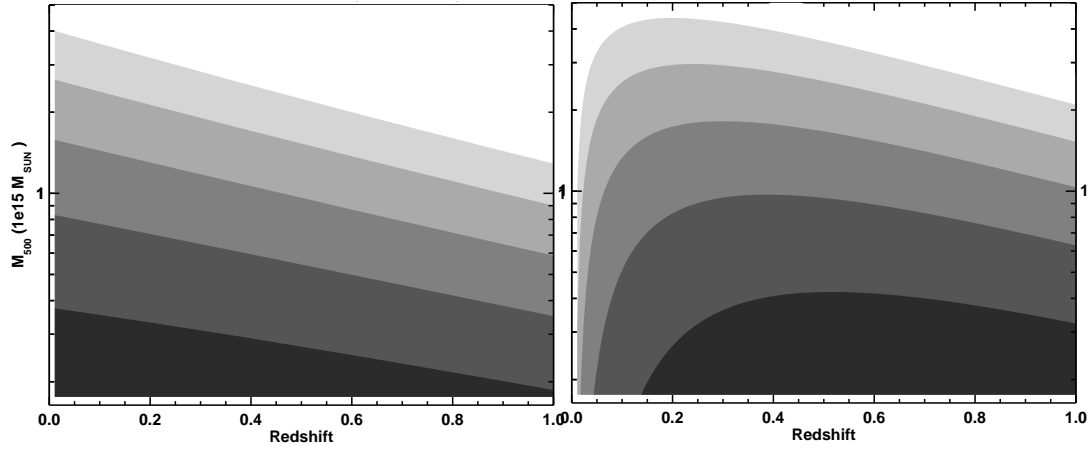
Figure 1.4 The Tinker et al. [273] mass function for an overdensity 400 times the matter density at the observed redshift. The overall normalization is an arbitrary unit. Left: The number of clusters per unit volume. Right: The total number of clusters within an observing volume.

Chapter 2

Galaxy Clusters

Galaxy clusters are complex structures with many degrees of freedom. This complexity brings both a richness of information and built-in cross-checks. A detailed knowledge of cluster astrophysics, however, is required to properly isolate these degrees of freedom. The most relevant physical properties to this work are: size, mass, temperature, density, and pressure. Cluster masses may be directly determined using gravitational lensing, or indirectly from the ICM by applying hydrostatic or virial assumptions. As the assumption of hydrostatic equilibrium generally fails for most galaxy clusters, scaling relations must be calibrated between hydrostatic masses and observational mass proxies that are insensitive to a cluster's dynamical state. Clearly, linear perturbation theory breaks down at the cluster level, and much of what scientists understand about cluster properties derives from complex N-body hydrodynamic simulations. Bertschinger [29] presents a nice review of N-body simulations for structure formation, although the review by Kravtsov & Borgani [145] is more up-to-date. This chapter explores how simulations and observables fit together to give a full description of the astrophysics of galaxy clusters.

2.1   Mass Profiles

Predicting the profiles of dark matter halos is non-trivial. Recall that kinetic energy is acquired following the triggering of the Jeans instability. This occurs approximately when the mean density is 200 times the critical density. The subsequent behavior of the two matter

components, however, is quite different.[1] Although a heating mechanism is absent for dark matter, dark matter particle trajectories will still relax at a much slower rate through phase mixing via gravitational coupling. The system relaxes when the centripetal motion of the dark matter particles prevents further gravitational collapse.

The simulations performed by Navarro, Frenk, and White ([201, 202], NFW) set the stage being the first to show that dark matter profiles have a universal radial scaling independent of mass, the initial power spectrum, or cosmological parameters. The scaling is observed to be self-similar when the radial parameter is normalized, such that the enclosed mass density is a constant multiple, Δ, of the critical density at the given redshift: $M_\Delta = \Delta\rho_c(z)(4\pi/3)r_\Delta^3$ (recall that $\rho_c(z) = 3H(z)^2/8\pi G$). The NFW simulations characterize the mass profile using a broken power law:

$$\frac{\rho_{NFW}(r)}{\rho_c(z)} = \frac{\delta_c}{(r/r_s)(r + r_s)^2}. \tag{2.1}$$

With this model, there are only two free parameters: r_s, the scale radius, and r_{200}, which is a good approximation of the virial radius. The ratio of these two parameters gives the concentration, $c = r_{200}/r_s$, and this sets: $\delta_c = 200c^3/3[\ln(1 + c) - c/(1 + c)]^3$. This radial description of the dark matter halo is commonly adopted in current cluster mass estimation analyses. Due to a combination of limited observational signal and instrumental limitations, galaxy clusters are often only observed out to R_{2500} and R_{500}, and special considerations must be made for these analyses. The NFW profile is plotted in Figure 2.1 for a typical concentration parameter of 4, with the positions of R_{2500} and R_{500} indicated.

Several alternative models to the NFW model have been proposed. Navarro et al. [203], for example, argue for a model in which the logarithmic slope varies continuously with radius: $\rho(r) \propto \exp(-Ar^\alpha)$. This model was originally proposed by Einasto [77],[78, 79] in the context of the light and mass distribution of galaxies. Merritt et al. [184] find that the rms scatter could be reduced by up to a factor of 4 using the Einasto model instead of the NFW model.

---

[1]In this work, baryonic matter will be referred to as "ga,s" since stars and galaxies play only a minor role in this process.
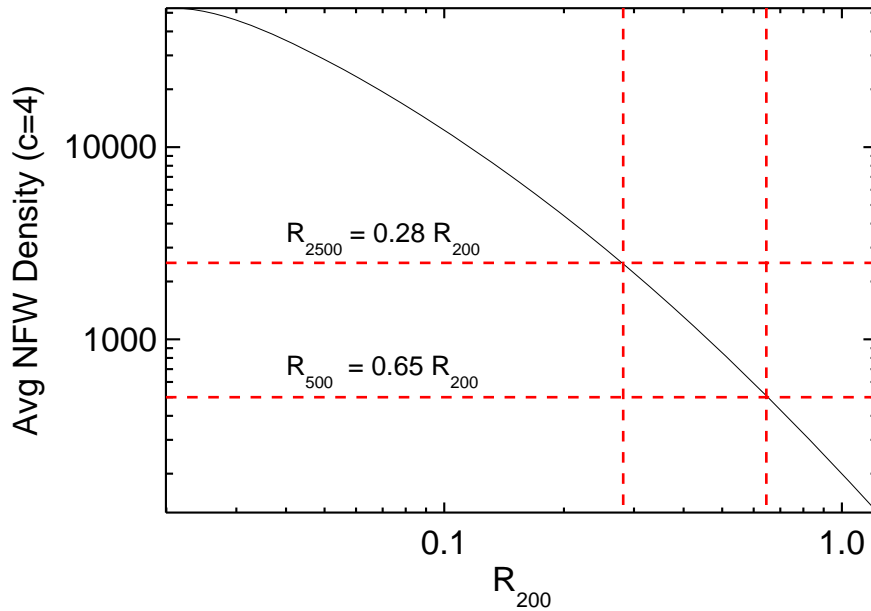
Figure 2.1 The average enclosed density of a Navarro-Frenk-White[201, 202] profile for a typical galaxy cluster with $c = 4$. The positions of R_{500} and R_{2500} are indicated by the dashed red lines and their values are given with respect to the virial radius.

2.2 X-ray Emission Due To Thermal Bremsstrahlung

The nature of X-ray detection provides both flux and spectral information, enabling the measurement of two independent observables: luminosity and temperature. Since all observations are 2D projections sourced by 3D physics, the electron densitiy, n_e, and X-ray temperature, T_X, can be determined using either projection or deprojection techniques. While the deprojection method can account for complex structure independent of a particular parameterization, it has yet to be confirmed whether this technique produces more accurate (or even different) results. Temperature and electron density profiles will be key to deriving hydrostatic mass esimates in Section 2.6.1.2, and the general techniques by which they are measured is reviewed. Several groups have made hydrostatic mass estimates using X-ray data, and any differences in their respective parameter estimation techniques will be highlighted when relevant (Allen et al. [6], Arnaud et al. [13], Bonamente et al. [37], Vikhlinin et al. [279], Pratt et al. [237]).

2.2.1 Pressure Profiles

In order to parameterize cluster properties, one must first choose a model. Pressure profiles can be constructed using X-ray measurements of electron density and temperature profiles. Cavaliere & Fusco-Femiano [52] proposed one of the first and most widely adopted pressure models, the isothermal β-model:

$$p(r) = \frac{p_0}{[1 + r^2/r_c^2]^{3\beta/2}}. \tag{2.2}$$

It has since become clear that the β-model is insufficient in describing cluster properties at both small and large radii. Pratt & Arnaud [234] and Pointecouteau et al. [231] made an initial step to expand this model by fitting two separate β-models at the interior and exterior radius. For obvious reasons, this is called the double β-model. Nagai et al. [198] combine X-ray data at small cluster radii with simulations at large cluster radii to demonstrate that cluster properties are self-similar at R_{500} and can therefore be described with a generalized NFW (GNFW) model:

$$p(r) = \frac{p_0}{(cr)^\gamma \left[1 + (cr)^\alpha\right]^{(\beta-\gamma)/\alpha}}. \tag{2.3}$$

The Arnaud et al. [15]GNFW parameter measurement of:

$$[P_0, c_{500}, \alpha, \beta, \gamma] = [8.403 h_{70}^{-3/2}, 1.177, 1.0510, 5.4905, 0.3081], \tag{2.4}$$

is commonly used as a universal pressure profile, to help constrain observationally-derived measurements and these parameters are also adopted for the present analysis. With major quality improvements in SZE data over the last several years, the parameters of the GNFW model have recently been constrained using SZE data as well (Planck Collaboration et al. [230], Sayers et al. [256]).

2.2.2 X-ray Spectral Temperature

The typical temperatures of the galaxy clusters studied in this analysis are $\sim$10 keV, or $\sim$10^8 Kelvin. This is the temperature of the transition between "hard" and "soft" x-rays
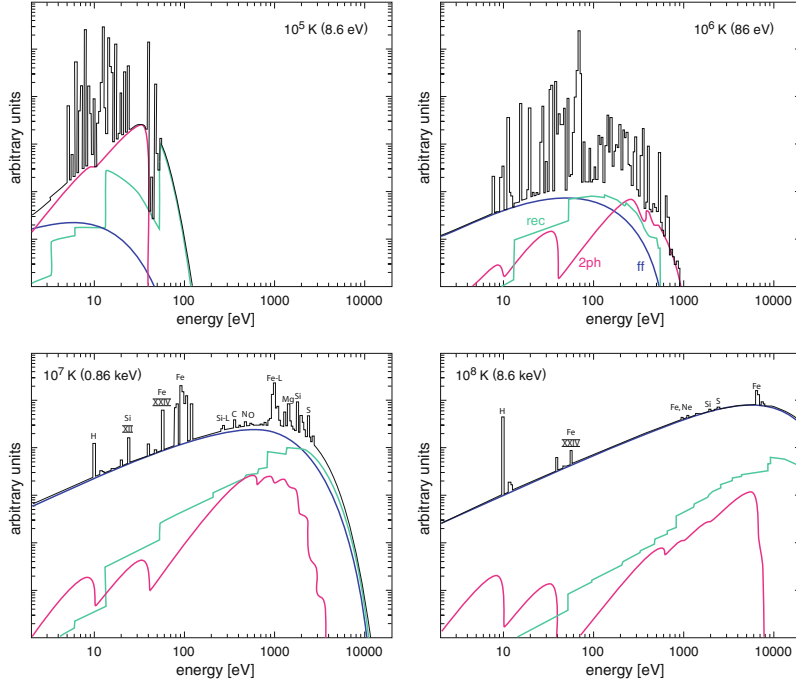
Figure 2.2 X-ray spectra for astronomical formations at different plasma temperatures with major emission lines labelled. (Blue) The continuum contribution from thermal bremsstrahlung, a.k.a. free-free, (green) recombination radiation with sharp ionization edges, a.k.a. free-bound, (red) two-photon radiation associated with the "forbidden" 2s-1s transition (Spitzer & Greenstein [265]). Line emission is produced when electrons change quantum energy levels, a.k.a. bound-bound. Note the dominance of the thermal bremsstrahlung contribution for the hottest object. Image taken from Böhringer & Werner [35].

and approximately 1/50th the rest-mass of an electron. Figure 2.2 demonstrates how at these extremely high temperatures, most emission is sourced by thermal bremsstrahlung.

Spectroscopically measured cluster temperatures, T_X, are a key ingredient with which hydrostatic masses and (to a much lesser extent) electron density profiles are derived. Several sets of code have been developed to fit X-ray spectra (both line and continuum emission) in order to measure temperature. The XSPEC code[2] is based on the MEKAL (Mewe-Kaastra-Liedahl) Model ([186, 135, 158]) and is used for the X-ray measurements utilized in this analysis. Of the hydrostatic mass estimates studies presently considered, Allen et al. [6] fit their temperature spectra to a constant T_X, while the Pointecouteau et al. [231] and Vikhlinin et al. [278] analyses use a higher-order temperature model.

As temperatures are known to fall with radius inside of galaxy clusters (e.g Pratt et al.

_____

[2] http://heasarc.gsfc.nasa.gov/docs/xanadu/xspec/

[235], George et al. [97]), Mazzotta et al. [179] examined the bias that might result by fitting a three-dimensional emission-weighted temperature to a single projected spectroscopic temperature. They conclude that, on average, the measured projected spectroscopic temperature would always under-estimate the true three-dimensional emission-weighted temperature, and in some cases by up to 80%! This is in part due to their observation that the spectroscopic temperature is less sensitive to high-density regions, such as shocks fronts, compared to emission weighted temperatures in simulations. This is definitely a source of concern, for hydrostatic mass estimates which require a spatially-resolved temperature model for accuracy. Mazzotta et al. [179] propose a spectroscopic-like temperature, which best reproduces typical spectroscopic observations fit to a single temperature model using simulations:

$$T_{sl} = \frac{\int n^2 T^{1/4} dV}{\int n^2 T^{-3/4} dV} \rightarrow \frac{\sum_{i=1}^{N} \rho_i T_i^{1/4}}{\sum_{i=1}^{N} \rho_i T_i^{-3/4}}, \tag{2.5}$$

where i is the index of the individually simulated particles.

Mathiesen & Evrard [174] demonstrate that the best approximation of the total thermal energy of a galaxy cluster is neither emission-weighted nor spectroscopic-like, but the mass-weighted temperature, T_{mw}:

$$T_{mw} = \frac{\int nT dV}{\int n dV} \rightarrow \frac{1}{N} \sum_{i=1}^{N} T_i. \tag{2.6}$$

T_{mw} is the direct average of the temperatures of individual mass particles, and this is also the temperature-weighting for the SZE signal.

2.2.3 X-ray Surface Brightness and Gas Mass Estimation

Bremsstrahlung occurs in the ICM when free electrons are deflected by the Hydrogen nucleii. Thermal X-ray emission is thus the product of both electron density, n_e, and proton density, n_p. For a fully ionized gas, $n_e = 1.21 n_p$, and n_e is therefore the physical property that can be calculated most readily from X-ray surface brightness maps. Typical values of n_e range from $10^{-5} - 10^{-1}$ cm^{-3} from the cluster outskirts to the cool-core.

White et al. [288] and Fabian et al. [86, 85] developed a commonly used technique to measure gas density by deprojecting X-ray surface brightness maps into a series of nested electron density shells. The contribution to the total flux from the temperature, $T(i)$, and electron density, $n_e(i)$, for each of these shells is then calculated. By assuming that $T(i)$ and $n_e(i)$ are constant within concentric shells, the flux contribution from each shell will be proportional to :

$$F(i) \propto \frac{n_e(i)^2}{4\pi D_L^2} \Lambda[Z, T(i), E] \propto \frac{n_e(i)^2 T(i)^{1/2}}{D_L^2},$$ (2.7)

where $\Lambda[Z(V), T(i), E]$ is the spectral emissivity/cooling function of the ICM and includes all of the detailed astrophysics of the emission. The subsitution $\Lambda \propto T^{1/2}$ is made in the right-hand equation and is a good approximation at the high temperatures of the ICM. Equation 2.7 is used to calculate luminosity, L, which is a physical property of the cluster directly obtainable from the observable, flux $F = L/(4\pi D_L^2)$.

Equation 2.7 is inverted to obtain the gas density of individual shells, $n(i)$, using the measured luminosity. The gas mass density, $\rho(i)$, is obtained from $n(i)$ using the molecular weight, $\mu \approx 0.6$, and the mass of a proton, M_p. An approximation for $T(i)$ is needed in this step, which can be solved for either entirely independently, using a single temperature model for the entire cluster, or, in a more complex iterative fashion, by simultaneously fitting the spectroscopic and luminosity data. Finally, with $\rho(i)$ in hand, M_{gas} can be directly calculated by integrating over the individual shells:

$$M_{\text{gas}} = 4\pi \int_0^{r_\Delta} \rho(r) r^2 dr = 4\pi \sum_i \rho(i) r_i^2 \Delta r_i.$$ (2.8)

Electron density profiles can also be determined by comparing the observed luminosity maps with a projected model. Bonamente et al. [37] apply this method using a β-model to model the gas distribution. The β-model is appealing, because its projected X-ray surface brightness profile has an analytical form—with the downside that it does not model the central regions of clusters accurately. B08 therefore excise the central 100 kpc data from both the spatial and the spectral data. Pointecouteau et al. [231] calibrate masses using a double β-model (with the option to all for a concentrated inner region). Vikhlinin et al. [278] add several more degrees of freedom to their model and also adopt a three-dimensional

parameterized temperature model, for a total of nine free parameters.

2.3 The Sunyaev-Zel'dovich Effect

When the first X-ray observations from galaxy clusters were made, Sunyaev & Zel'dovich [270, 271] predicted that such a hot plasma would be able to inverse Compton scatter the CMB, increasing its energy. This is the Sunyaev-Zel'dovich effect (SZE) and it turns out to be very small. It therefore took several more decades after its initial prediction before the SZE could reliably be observed in individual clusters.

2.3.1 Theory

The CMB is an ensemble of photon states, whose spectral characteristics approximate an almost perfect 2.725 Kelvin blackbody. When these photons pass through a hot, 10 keV, electron gas, on average, they will scatter up to higher energies. These photon states might be replenished by lower energy photons, which also scatter upwards. At about 219 GHz the net photon gain in occupation number balances the net loss, resulting in a null signal. The observed temperature of the CMB is thus altered:

$$T_{SZ} = f(x)yT_{CMB}, \tag{2.9}$$

with

$$f(x) = x\frac{e^x + 1}{e^x - 1} - 4. \tag{2.10}$$

$f(x)$ contains all the spectral information and is only a function of the Boltzmann ratio of the CMB itself, $x = h\nu/k_B T_{CMB}$. Depending on the application, the relativistic motion of the hot electrons and high peculiar velocities of the clusters with respect to the CMB must be accounted for. At moderate observing frequencies and temperatures, relativistic corrections to the SZE signal can be included by multiplying $f(x)$ by the frequency and electron-temperature dependent factor $(1 + \delta(x, T_e))$ [296, 125, 206]. The specific temperature and frequency dependencies of these relativistic corrections are quite complex, and Chluba et al. [55] provide one of the more popular techniques with which to estimate the

relativistic SZE signal and have publically released their C^{++} code.[3] Relativistic corrections are generally $\lesssim 10\%$ for the cluster sample observed with *Bolocam* at 140 GHz and are included only when physical quantities are derived from the Y_{SZ} signal.

The Compton parameter, y, represents the magnitude of the distortion and, in the non-relativistic limit, encompasses all of the cluster information in the CMB distortion. This term is directly proportional to the electron pressure, P, integrated along the line-of-sight:

$$y = (\sigma_T/m_e c^2) \int P dl, \tag{2.11}$$

where σ_T is the Thomson cross section, m_e is the electron rest mass, and c is the speed of light.

The SZE observable is often expressed using a volume integral:

$$Y_{SZ} D_A^2 = \left(\frac{\sigma_T}{m_e c^2} \right) \int P dV = D_A^2 \int y d\Omega, \tag{2.12}$$

where D_A is the angular diameter distance of the source. This equation presents Y_{SZ} as a cylindrical integral, although Y_{SZ} is also presented using a spherical volume integral. As the cylindrical form of Y_{SZ} requires no additional assumptions to be made in regards to is line-of-sight extent, the cylindrical value is chosen for the present analysis.

2.3.2 Detecting the Sunyaev-Zel'dovich Effect

It took several years to detect the SZE after its initial prediction, owing to the fact that it is much too dim for the sensitivities of the instrumentation of the time. The 168 GHz peak signal is too low in energy to excite semi-conductor CCD technology, and it lies at a relatively high frequency for typical radio coherent detection. Furthermore, atmospheric water vapor is strongly absorbing in this regime and there are few places in the world with the proper climate and facilities to perform these observations.

Throughout the seventies, several groups claimed detection of the SZE using coherent detection with single dish radio telescopes (Pariiskii [211, 212], Gull & Northover [107]).

---

[3]`http://www.cita.utoronto.ca/~jchluba/Science_Jens/SZpack/SZpack.html`
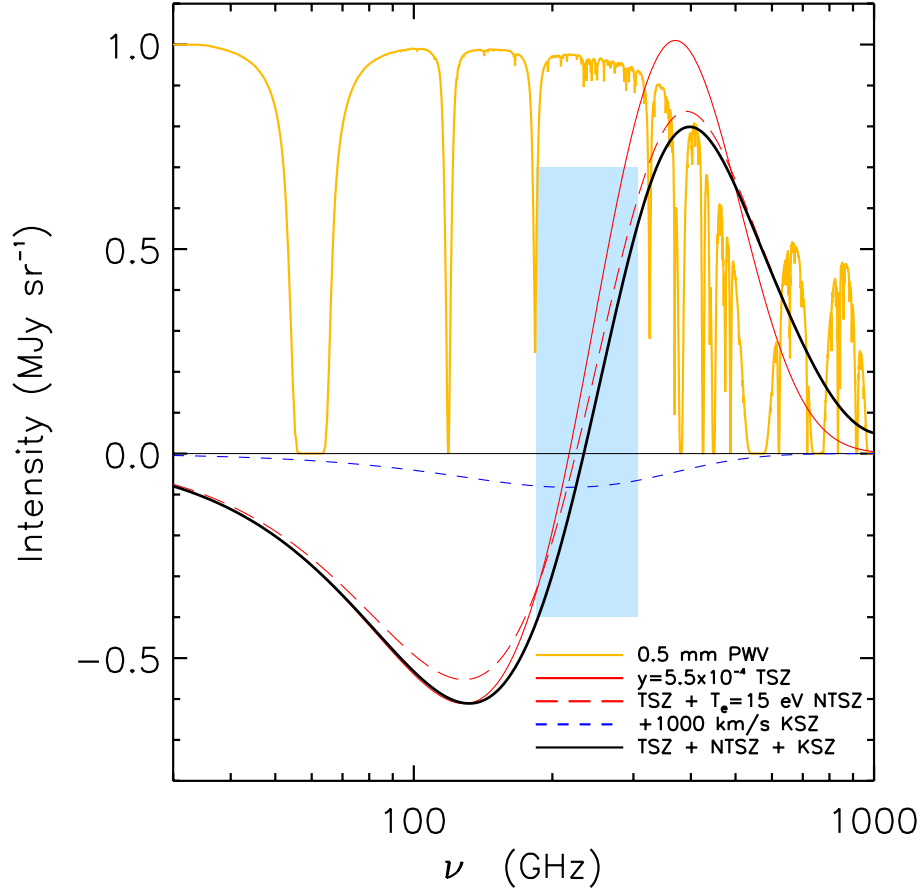
Figure 2.3 Approximate thermal SZE model spectrum for RXJ 1347.5, a.k.a. MACSJ 1347.5 (solid red line) with $y = 5.5 \times 10^{-4}$, $T_x = 15$ keV, and $v_{pec} = 1000$ km/s. Also shown are the distorted spectra after the addition of non-thermal/relativistic corrections (dashed red line), and kinetic SZE corrections (black line). Note how each correction element shifts the nominal SZE null from 217 GHz. At such high cluster temperatures, the relativistic effects are substantial in the spectral region with the SZE increment. The intensity of the kinetic SZE component alone is also plotted (blue dashed line) and Z-Spec's effective bandwidth is depicted in the solid blue region. The atmospheric transmission for a preciptiable water vapor column of 0.5 mm at Mauna Kea is shown in yellow. From this curve, it can be seen how difficult it is to observe the SZE increment due to the high level of atmospheric absorption. Figure taken from Zemcov et al. [300]. *Bolocam* data is used in this work to provide both a spatial template for the Z-Spec analysis, and also to constrain the overall y value serving as a spectral "lever arm" at 140 GHz.

These results, however, were of low significance and often disputed, and it took approximately until the end of the following decade for radio observing techniques to progress to the point where SZE observations of galaxy clusters could be reliably reproduced (Birkinshaw et al. [32, 31], Lake [150], Readhead et al. [240]). In the early nineties, the SZE started to be observed with radio telescope arrays, such as the Ryle Telescope (Jones et al. [132]) and the Owens Valley Radio Observatory (OVRO, Carlstrom et al. [48]), specifically configured with shorter baselines, enabling better atmospheric removal and resolved mapping. More recently, the Sunyaev-Zel'dovich Array (SZA, Muchovej et al. [196]) was specifically constructed to observe the SZE and consists of eight 3.5m telescopes, which provide a $12'$ instantaneous field of view. Six of the antennas are in a close-packed array to provide sensitivity at $2'$ resolution, and two outrigger antennas provide $0.3'$ resolution to aid in the removal of point sources. Coherent detectors were also launched in space, and operated in the highly successful COBE (Boggess et al. [34]) and WMAP (Bennett et al. [23]) CMB satellite missions.

The SZE can also be detected by directly absorbing the radiation, using bolometers to measure power. Bolometric observations of the SZE started in the early eighties, thanks to a significant expansion of the infrared and submillimeter observational capabilities on Mauna Kea. Meyer et al. [187] performed bolometric observations of the SZE using the Infrared Telescope Facility, and Chase et al. [53] attempted to measure the SZE increment using the United Kingdom Infrared telescope. The Caltech Submillimeter Observatory (CSO) was commissioned in 1986, and, with a 10.4 m primary, it is better suited to observe the SZE than the existing infrared facilities. The Sunyaev-Zel'dovich Infrared Experiment (SuZIE) successfully measured the SZE at the CSO in 1994 (Wilbanks et al. [291], Holzapfel et al. [121]), fielding high-sensitivity neutron-transmutation-doped (NTD) bolometers (Palaio et al. [210]). The camera contained three pairs of bolometers, sensitive to 142 GHz, 217 GHz, and 269 GHz, respectively. The first version of the camera used a solid sapphire substrate for the absorber (Holzapfel et al. [121]), and the second version upgraded to a new silicon-mesh (spider-web) absorber (Bock et al. [33], Mauskopf et al. [178]), making the detectors less sensitive to cosmic rays. The NTD spider-web bolometers endured to have a great legacy and were subsequently employed in many high-profile sub-millimeter experiments, such as: *Archeops* (Benoît et al. [24]), *Bolocam* (Haig et al. [109]), BOOMERanG (de Bernardis et al.

[63]), BLAST (Devlin et al. [66]), and *Planck* [222].

While these detectors have outstanding sensitivity, they are difficult to multiplex. Therefore the bolometer of choice in current generation of SZE instruments, containing on the order of 1000 detectors, is the transistion-edge sensor (TES). For a good review of TES detectors, see Irwin & Hilton [124]. TES detectors can be multiplexed using either time-division multiplexing (Chervenak et al. [54], de Korte et al. [65]) or code-division multiplexing schemes (Yoon et al. [298], Kiviranta et al. [141]). TES detectors have been used in the Atacama Pathfinder Experiment (APEX-SZ, Dobbs et al. [69]), the South-Pole Telscope (SPT, Ruhl et al. [248]), its polarization-sensitive successor (SPTpol, Austermann et al. [17]), the Atacama Cosmology Telescope (ACT, Swetz et al. [272]), and its polarization-sensitive successor (ACTpol, Niemack et al. [205]), and the Multiplexed SQUID/TES Array at Ninety Gigahertz (MUSTANG, Dicker et al. [68]).

As submillimeter astronomical projects become more ambitious, there is a push to increase the pixel count by more than an order of magnitude, which would require considerable technological advancement. A promising new type of pair-breaking detector is the microwave kinetic inductance detector (MKID, Day et al. [62]). This detector is highly multiplexable and is the detecting element chosen for the Multiwavelength Submillimeter Inductance Camera (MUSIC), which is currently being commissioned at the CSO (Golwala et al. [101]). This camera is a pathfinder for the type of instrumentation that will be implemented for an ambitious project currently under development, the Cerro Chajnantor Atacama Telescope (CCAT, Woody et al. [294]).

2.4   Gravitational Lensing

According to the general theory of relativity, gravity attracts light much in the same way as it attracts mass. A massive galaxy cluster positioned between an observer and a galaxy will deflect the light like a lens, producing arcs and multiple images of the background source. Strong lensing primarily uses the position and redshift of these sources to map the mass distribution of the lensing object. This requires both high-resolution data as well as high quality spectroscopic data. Weak lensing operates in the limit where the gravitational

distortion is weak, producing a quadrupole distortion of the background galaxies. A thorough review of the weak gravitational methodology is included in Bartelmann & Schneider [18]. This shear can be measured in a statistical sense to reconstruct a cluster's mass profile, up to a constant offset in mass known as the mass-sheet degeneracy. Umetsu et al. [276] break this degeneracy by measuring the absolute magnification of the background galaxies via the positional dependence of the surface density of these galaxies. While lensing gives a fully nonbaryonic cluster mass estimation, cosmic web confusion can still introduce uncertainties of up to 20% (Hoekstra [118]). Several different methods exist to reconstruct the mass profiles both parameterically (e.g. Jullo et al. [133], Merten et al. [185]) and non-parametrically (e.g. Coe et al. [57], Zitrin et al. [304]).

2.5 Richness Measures/Velocity Dispersion/Red Sequencing

One of the biggest ironies of the term "galaxy clusters" is that only a small portion of all of the virialized matter is contained in stars. The motion of these stars, however, is dictated by the gravitational potential and can be used to measure mass. Using the dispersion in the redshift-determined velocities of individual galaxies, one can determine their line-of-sight velocity, which is correlated with cluster mass. Zwicky [307] famously proposed the existence of dark matter based on the measured velocity dispersion for the Coma cluster. Inevitably, such high quality spectroscopic data is not available for most galaxy clusters, and the application of this technique is limited.

Clusters can also be identified through their optical richness, or the number of galaxies within a specified aperture and above a specified luminosity. One of the most popular methods for cluster selection is the "red-sequence", which identifies galaxies based on a linear color-magnitude relation ([42, 99]). This method only requires photometric data at a few selected wavelengths. Using the red-sequence, High et al. [116] measure a correlation between optical richness and cluster mass for Y_{SZ}-selected clusters in the South Pole Telescope survey, although with a high degree of scatter (35%). Despite a large measured scatter, the red

sequence is a promising technique for identifying and weighing high redshift clusters (Stanford et al. [268]).

2.6 Cluster Mass Estimation

Less than 20% of the mass of a galaxy cluster is ordinary matter. Therefore, cluster mass estimation is, to first order, dark matter estimation. The rich set of observables provided by galaxy clusters is valuable in that it provides important cross-checks for a given observational probe's mass estimate. The equation of hydrostatic equilibrium links pressure-derived observables directly to the total cluster mass in the limit where the cluster is relaxed and pressure is only sourced by the thermal motion of the ICM. Of these observables, X-ray observations provide both spectroscopic and bolometric information, while the SZE surface brightness does not dim with redshift. Gravitational lensing is insensitive to the detailed astrophysical processes occuring inside of a galaxy cluster, but the necessary high-quality data needed for these measurements is only available for a handful of clusters. Fully robust mass estimation must integrate all of this information and develop a set of calibrated mass proxy scaling relations that can be used on clusters where high-quality optical data is not available.

2.6.1 Hydrostatic Equilibrium, Self-Similarity, and the Virial Theorem

Following the Jeans instability, in contrast with dark matter, gas undergoes an accretion shock, and further infalling gas is heated when it encounters this shock [28, 83, 44, 96, 189]. These shocks source the entropy, which heats the clusters to several keV (where $1\text{keV} \approx 1.16 \times 10^7 \text{K}$), and the gas rapidly relaxes to form an inter-cluster medium (ICM). The ICM sources the two central observables to this thesis: X-ray emission via thermal bremsstrahlung and the SZE.

While the underlying dark matter halo does not contribute any photons to the observables, its gravitational potential will affect the gas pressure and thereby boost the signal. A

common idealization in fluid dynamics (e.g. galaxy clusters) is that the fluid is adiabatic and in a state of equilibrium. This means that kinetic energy is not altered by such processes as viscous heating, thermal conduction, or emission/absorption of radiation. In the adiabatic regime, the equation of state has only one thermodynamic degree of freedom, pressure, $P = P(\rho)$, which is solely a function of density. This leads to the equation of hydrostatic equilibrium (HSE), which is a restatement of the Archimedes Principal: *The amount of force on an object is equal to the weight of the mass that it has displaced:*

$$\nabla P = \rho \mathbf{g} \;\; = \;\; -\rho \nabla \Phi \tag{2.13}$$

$$\frac{dP}{dr} \;\; = \;\; -\rho \frac{d\Phi}{dr}, \tag{2.14}$$

where in the second equation, spherical symmetry is assumed, and $d\Phi/dr$ can be calculated using Newton's field equations:

$$\nabla^2 \Phi = -\nabla \cdot \mathbf{g} = 4\pi \mathbf{G} \rho. \tag{2.15}$$

Combining equations 2.14 with 2.15 and integrating once using the boundary condition: $dP(r \to \infty)/dr = 0$ yields:

$$\frac{dP}{dr} = -\frac{GM(r)\rho_g}{r^2}. \tag{2.16}$$

By introducing the ideal gas law, $P = \rho_g T$ into Equation 2.16, one finds the total mass scales as:

$$M \;\; \propto \;\; RT \left[\frac{d\ln P}{d\ln r} \right]. \tag{2.17}$$

The ideal gas law generally holds for high-temperature, low-pressure, monatomic gases, which are typical conditions in the ICM. The HSE methodology can be applied to any observable which measures pressure (i.e. X-ray or SZE).

A common assumption applied to galaxy clusters is that they are self-similar. Self-similarity means that, for a particular normalization, all clusters, regardless of absolute size, share similar behavior. Imposing self-similarity on Equation 2.17 implies that $d\ln P/d\ln r_\Delta$

is universal for all clusters at the particular radius, r_Δ. Equation 2.17 then simplifies to:

$$M \propto RT \quad \rightarrow \quad T \propto \frac{M}{R} \propto \Delta \rho_{cr}^{1/3} M^{2/3} \tag{2.18}$$

$$P \quad \propto \quad M^{5/3}. \tag{2.19}$$

Kaiser [136] was one of the first to verify this assumption using N-body simulations. Self-similarity implies: (1) that the amplitude of the density fluctuations is a simple power-law, $\sigma(k) \propto k^{3+n}$, and (2) that gravitational collapse, and the physical processes that produce cluster observables, are scale-free. These assumptions leave two free cosmological parameter dependencies: the normalization of the power spectrum, and its scale factor, n.

On the other hand, if clusters are not self-similar, then hydrostatic mass estimation must start from either Equation 2.14 or Equation 2.17. This is precisely what is done to obtain hydrostatic mass estimates from gas observables, described in further detail in Section 2.6.1. As X-ray data provides an additional independent measurement compared to the SZE, it is more broadly implemented for HSE mass estimation. To derive the X-ray-specific form of the HSE equation, the ideal gas law will once again be inserted into Equation 2.16. This time, however, self-similarity will not be invoked:

$$M(r) = -\frac{kTr^2}{\mu M_p G} \left(\frac{d\ln \rho_g}{d\ln r} + \frac{d\ln T}{d\ln r} \right), \tag{2.20}$$

where the subsitition $\rho_g = \mu n_e M_p$ has been made. With the X-ray temperature and electron density profiles in hand, one can use Equation 2.20 for massive, dynamically relaxed galaxy clusters, where the pressure can be derived *thermally* from the ideal gas law. The gas mass fraction, f_{gas}, can then be calculated by dividing the mass calculated at a specific radius, M_{tot}, by M_{gas} (which, recall, is determined by integrating n_e over the volume of the cluster). HSE cluster candidates are generally chosen at low redshifts to ensure high-quality data and to remove any cosmological dependence that might bias the measurement.

Another approach for estimating mass is to integrate Equation 2.14, which simply restates the virial theorem for an ideal gas:

$$2E_{th}(r) - 3P(r)V = -U_g(r), \tag{2.21}$$

where $E_{th}(r)$ is the total thermal energy of the system, $P(r)$ the pressure, V the enclosed volume, and $U_g(r)$ the gravitational potential energy. The $3P(r)V$ term is added to the traditional formulation of the virial theorem and represents the boundary condition of a surface pressure component. In the absence of this component, this equation states that the kinetic energy of a bound system is twice the gravitational potential and can be derived from a time-averaged form of the Hamiltonian. The surface pressure term allows the kinetic energy to build up a little more. Mroczkowski [192] develops this theory (see Mroczkowski [193] for the inclusion of the surface pressure term) to apply to obtain cluster masses directly using the SZE effect. This method imposes a strong assumption of how gas mass scales with total mass, i.e., $\rho_{gas}(r) = f_{gas}\rho_{tot}(r)$, and therefore is not used directly in the present analysis.

2.6.1.1 Deviations from Hydrostatic Equilibrium

With the electron density and temperature models in hand, one can, in principle, calculate hydrostatic masses using Equation 2.20. Recall that the equation of hydrostatic equilibrium simply demonstrates how pressure and gravity must balance in order to attain equilibrium. If, however, there is a source of non-thermal pressure, equilibrium will be achieved with less thermal pressure. Fortunately, some of these non-thermal sources of pressure, e.g. turbulence and bulk flow, are inherently modeled in hydrodynamic simulations, which trace the motion of gas. These simulations indicate an increasing level of non-thermal pressure at large radii, up to 20-30% at cosmologically interesting radii, leading to an overall 10-15% bias in hydrostatic mass estimates (Lau et al. [153], Battaglia et al. [20, 19], Burns et al. [47], Navarro et al. [201], Rasia et al. [239], Nagai et al. [200], Jeltema et al. [128]). Most HSE mass measurements subsequently account for this bias in some form or another.

The assumption of adiabaticity can be broken by radiative cooling. Radiative cooling is needed for all star formation and is believed to be the process which sets the entropy scale for clusters (Peterson et al. [220], Peterson & Fabian [219], Voit [281], Borgani et al. [41]). Protostellar collapse occurs when gas molecules cool via collisional transfer with dust grains, which in turn radiatively cool the protostellar medium (Larson [152]). Most of the stellar population in clusters is expected to have formed at high redshifts, $z > 2$ (Jimenez et al. [130]), although it is still unclear what fraction of these stars are formed inside of the galaxy

clusters themselves, versus having been acquired via accretion. Simulations by Conroy et al. [59], however, suggest that accreted galaxies have their stellar fraction dispersed into the low-luminosity intracluster light, instead of staying bound as a satellite galaxy or being deposited in the brightest central galaxy.

The $L_X - T_X$ relation was one of the first scaling relations to show deviations from self-similarity, with the relation steepening for the lower mass clusters from the predicted $L_X \propto T_X^2$. (Henry & Arnaud [114], White et al. [289], Markevitch et al. [167], Allen & Fabian [5], Arnaud & Evrard [12], Finoguenov et al. [88, 89]). Bryan [43], Voit & Bryan [282] and Voit et al. [283] argue that the observed deviation from self-similarity is due to the cooling and condensation of gas accompanying star formation. X-ray radiative-cooling models, however, indicate that radiative cooling alone would lead to a much higher than optically-observed stellar mass (Lin et al. [160], Gonzalez et al. [102]). To balance this, star-formation could be slowed by supernova and AGN activity in the core cluster galaxies, which eject high-entropy gas to the cluster outskirts (Markevitch et al. [167], De Grandi & Molendi [64], Vikhlinin et al. [278]). Simulations by Nagai et al. [200] demonstrate this activity to be centralized within cluster radii of about R_{2500}.

Mergers are probably the most obvious example of clusters departing from HSE. The effect of merger activity on cluster observables has attracted a good amount of attention recently (see Wik et al. [290], Nelson et al. [204], Krause et al. [144]). These simulations demonstrate that the assumption that gas mass follows the iso-contours of the underlying dark matter halo fails for disturbed clusters, while frictionless dark matter halos "slosh" around the cluster core, out of phase with the baryonic matter (Ascasibar & Markevitch [16], ZuHone et al. [306]). Molnar et al. [190] suggest that this might leave an observational signature in the projected offset between the SZE and X-ray peaks of galaxy clusters.

Shock fronts provide additional non-thermal pressure, because they prevent the free motion of gas. The relative velocity of halo collisions can be measured from the shock Mach numbers, and these collisions can be up to thousands of kilometers per second (Markevitch & Vikhlinin [169]). Several shock fronts have been identified in galaxy clusters—most notable, of course, is the X-ray image of the Bullet Cluster (Markevitch et al. [168]). With new high-resolution SZE cameras, such as MUSTANG, shock fronts have also been identified

with the SZE (Korngut et al. [143]). In addition to shock fronts, simulations demonstrate that residual bulk motion in the ICM could provide an additional non-negligible source of non-thermal pressure support (Evrard [83], Dolag et al. [70], Lau et al. [153]).

There is ample evidence demonstrating that galaxy clusters are not the smooth, spherical objects that they are often modeled as. For example, mass accretion could be preferentially aligned along collapsed filamentary structures, which remained like a Swiss cheese after the initial collapse of the overdensities. Simulations by Battaglia et al. [19] indicate that ellipticity is largest for clusters at z=1. This ellipticity is dominated by the dark matter component, with gas distribution being significantly more spherical, leading to a potential source of mass bias. A prolate cluster, with its major axis aligned along the line-of-sight, will project a different signal than the same cluster with its major axis aligned in the plane of the sky (Krause et al. [144], Morandi et al. [191]). Furthermore, the specific shape of the mass and gas profile matters at large radii, where the ICM can still contribute a significant amount of SZE flux (Battaglia et al. [20], Lau et al. [154]). Battaglia et al. [19] notice a significant asphericity in cluster gas that is not necessarily aligned with the dark matter halo, and this will naturally bias mass estimations, which assume that the gas follows the dark matter equipotential surfaces. Muñoz-Cuartas et al. [195] simulate cluster halo asphericity and notice that it increases with both mass and redshift. They measure the major-to-minor axis ratio of their simulated cluster halos to be less than 0.5 at 0.3 r_{vir} for halo masses $\sim 10^{15} M_\odot$. On the observational side, Skielboe et al. [261] use a stacked sample of 1743 clusters from the SDSS catalog [4] and measure a higher degree of optical dispersion for galaxies aligned along the major axis of the central galaxy, with respect to those aligned along the minor axis: $\Delta \sigma_\nu / \langle \sigma_\nu \rangle = 6\% \pm 2\%$. This they interpret to be the signature of a preferred prolate cluster geometry based on the simulation results of Gottlöber & Yepes [104].

Significant levels of gas clumping in the outskirts of galaxy clusters have been observed using the Suzaku X-ray telescope, which has a factor of ten less background due to its low-Earth orbit than the previous generation of X-ray telescopes. Measurements by Bautz et al. [21] and Simionescu et al. [260] of this gas clumping indicate an excess of X-ray emission than predicted from theory and simulations. These observations are supported by N-body

---

[4]For more details about the SDSS survey, see Appendix A.

simulations, which indicate cold clumps of infalling gas, such as galaxies, through accretion and merger activity. Nagai & Lau [199] parameterize this using a "clumping" factor:

$$S_X(r) \propto \langle \rho_{gas}^2(r) \rangle = C(r) \langle \rho_{gas}(r) \rangle^2, \qquad (2.22)$$

$$C(r) = \frac{\langle \rho_{gas}^2 \rangle}{\langle \rho_{gas} \rangle^2} \geq 1. \qquad (2.23)$$

Electron density profile measurements generally assume $C(r) = 1$, which would result in overall biases of $\sqrt{C(r)}$ in the density profiles. Note that the parameterization is more general than "clumpiness," for example, shock fronts would also result in $C(r) \neq 1$. Numerous groups (Buote & Humphrey [45], Khedekar et al. [140], Zhuravleva et al. [302]) are currently investigating this phenomenon. As these observations are still recent, clumping is generally not accounted for in hydrostatic mass corrections.

2.6.1.2 X-ray Hydrostatic Mass Measurements

The sample characteristics of four X-ray hydrostatic mass calibration studies will be reviewed to the extent that they pertain to this work: Allen et al. [6, hereafter A08], Bonamente et al. [37, hereafter B08], Vikhlinin et al. [278], and Pointecouteau et al. [231]. The information presented below, together with the relevant scaling relations discussed in Section 2.6.3, is summarized in Table 2.1.

A08 measure hydrostatic masses for a sample of 42 hot ($kT > 5$keV) X-ray luminous, dynamically relaxed galaxy clusters between $0.05 < z < 1.1$. These are the masses used to calibrate the scaling relations in the M10 sample, and, by extension, this work. With weak priors on cosmology, A08 measure f_{gas} to be constant for all 42 clusters of their sample. They measure $f_{\mathrm{gas}} = 0.1104 \pm 0.0016$ at R_{2500}—a result supported by independent observational analyses (Bonamente et al. [37], Zhang et al. [301], Mahdavi et al. [163]). A08 note that the f_{gas} measurements of a subsample of 6 low-redshift clusters is consistent with the entire sample, and the additional rms scatter measured for the entire sample is approximately what would be predicted from hydrodynamic simulations. A08 conclude M_{gas} to be a low-scatter universal proxy for the total cluster cluster mass, M_{tot}. The power of the A08 result is that

M_{tot} can be directly obtained from M_{gas}:

$$M(r_\Delta) = \frac{M_{\text{gas}}(r_\Delta)}{f_{\text{gas}}(r_\Delta)} = \frac{4\pi \Delta \rho_{cr}(z) r_\Delta^3}{3}. \tag{2.24}$$

M10 use the A08 measured f_{gas} value and add an additional $\sim 8\%$ systematic uncertainty to the value to account for scatter in unrelaxed systems.

B08 measure hydrostatic masses using *Chandra* X-ray data for a sample of 38 clusters, split evenly into a low redshift ($z < 0.30$) and a high redshift subset ($0.30 < z \leq .90$). The measured M_{gas} spans approximately an order of magnitude from 10^{13} to 10^{14} $M_\odot$. These are the masses used to calibrate the B08 SZE-X-ray scaling relation study, which shares many properties in common with the BOXSZ sample. Similar to A08, B08 do not detect any scaling of f_{gas} with mass or redshift. B08 include an additional 20% gaussian noise to their M_{tot} values to account for systematic uncertainties. The dominant component of this systematic uncertainty is from the estimated bias due to projection effects caused by cluster asphericity. Cluster asphericity for the sample is characterized using the measured projected ellipticity of the X-ray surface brightness maps. LaRoque et al. [151] measure a mean projected major-to-minor axis ratio of 0.79 for the B08 sample, with an rms scatter of 9%. They then use this as the hypothetical distribution for the line of sight ellipticty of the clusters and calculate the rms scatter that the asphericity would produce under the assumption of a spherical model—20%.

Vikhlinin et al. [278] measure hydrostatic masses using *Chandra* data for 13 low redshift, relaxed galaxy clusters with temperatures ranging betwee 0.7 and 9 keV. They too measure hydrostatic masses for a higher redshift 36-member cluster sample with $0.35 < z < 0.9$, using moderate cosmological priors. These mass calibrations are used in the work of Vikhlinin et al. [278, 279].

Pointecouteau et al. [231] measure the hydrostatic masses for 10 clusters with $z < 0.15$. These masses are used to calibrate the Arnaud et al. [13, 14] scaling relations. Arnaud et al. [15, hereafter A10] use 8 of these clusters together with an additional 12 clusters from the REXCESS sample (Pratt et al. [237]) for hydrostatic mass calibration, although it appears that the hydrostatic masses of the additional sample have not been published. These A10

scaling relations, in turn, are used to calibrate the masses for the Planck Collaboration et al. [224, 227] SZE results.

Arnaud et al. [13], Pratt et al. [236], Vikhlinin et al. [279] and Pratt et al. [237] all conclude that f_{gas} evolves with cluster mass:

$$f_{gas} \propto M_{tot}^{\alpha}. \tag{2.25}$$

Specifically, V09 measure $\alpha = 0.13 \pm 0.02$, and Pratt et al. [236] measure $\alpha = 0.21 \pm 0.03$. These results could possibly be reconciled with A08 and B08 if f_{gas} asymptotes to a constant value for clusters with temperatures above 5 keV. Simulations give varying expectations for whether f_{gas} evolves with mass or temperature. While some simulations, which include non-thermal processes demonstrate f_{gas} to be constant (Eke et al. [82], Crain et al. [61], Fabjan et al. [87]), others observe f_{gas} to evolve with mass and redshift (Kravtsov et al. [147], Stanek et al. [267], Battaglia et al. [19]). The resolution of the uncertainty in the evolution of f_{gas} with redshift and M_{tot} for high-mass clusters is a key priority in the field.

2.6.2   The Y_X Mass Proxy

After observing f_{gas} to evolve with mass and redshift in their simulations [147], Kravtsov et al. [148] propose the X-ray analog of Y_{SZ}, $Y_X = C M_{gas} T_X$ to be a more robust low-scatter mass proxy, where,

$$C = \frac{\sigma_T}{m_e c^2} \frac{1}{\rho_{\mathrm{gas}}/n_e} = 1.406 \times \frac{10^{-5}\mathrm{Mpc}^2}{10^{14}\mathrm{keVM}_\odot}, \tag{2.26}$$

σ_T is the Thompson cross-section, and $\rho_{\mathrm{gas}}/n_e = 1.149 m_p$ for a highly ionized gas. Y_X is suggested to be a lower-scatter mass proxy because the non-thermal scatter in M_{gas}, and T_X are expected to be anti-correlated. This can be understood in the sense that AGN activity in the cluster core will eject baryons radially outwards, both heating the ICM and lowering the relative baryon fraction. Motivated by these results, several observational studies have used Y_X as a default mass proxy (Vikhlinin et al. [279], Andersson et al. [8], Planck Collaboration et al. [224], Lin et al. [161]). The measured Y_X scaling relation results are summarized in

Table 2.1.   X-ray mass calibration sample characteristics used by the various SZE studies.

Name	Obs	Scaling Relation	σ	$N_{\rm cl}$	$\langle z \rangle$	$\langle T_x \rangle$	M_{500}
A08	CXO	$f_{\rm gas} = 0.1105 \pm 0.0005 (r/r_{2500})^{0.214 \pm 0.022}$	0	42	0.35	~ 7 keV	$[\sim 3, 21.7]$
A08C	CXO	$f_{\rm gas} = 0.113 \pm 0.003$	0	6	< 0.15	~ 8 keV	$[\sim 5, 10.1]$
B08	CXO	$f_{\rm gas} = 0.116$	$\cdots$	38	0.30	~ 7 keV	$[2.0, 16.2]$
K06	ART N-body	$M_{500} \propto Y_X^{0.581 \pm 0.009}$	0.071	16	0.3	$\cdots$	$[0.4, 13.0]$
K06	ART N-body	$M_{500} \propto M_{g,500}^{0.921 \pm 0.023}$	0.107	16	0.3	$\cdots$	$[0.4, 13.0]$
V09C	CXO	$M_{500} \propto Y_X^{0.53 \pm 0.04}$	0	17	< 0.25	~ 6 keV	$[1.0, 22.8]$
A10	XMM	$M_{500} \propto Y_X^{0.561 \pm 0.018}$	0.1	20	< 0.15	~ 4 keV	$[1.0, \ 8.4]$

Note. — A compilation of the X-ray- and simulation-derived scaling relations adopted for the various works discussed in the text. First column: The analysis from which these values where derived, where the letter C indicates a low-redshift scaling relation for cosmological applications: (A08) Allen et al. [6], (B08) Bonamente et al. [37], (K06) Kravtsov et al. [148], (V09) Vikhlinin et al. [279]. Second column: The X-ray observatory or the simlation code that was used to derive the scaling relations: (CXO) *Chandra* X-ray observatory, (XMM) XMM-*Newton* X-ray observatory, (ART N-body) Adaptive Refinement Tree N-Body hydro-dynamic code (Kravtsov et al. [146].) Third column: The measured values for the given scaling relation analysis. Fourth column: The measured intrinsic scatter for a given relation. Fifth column: The number of clusters used to constrain the scaling relation. Sixth column: The median redshift for the scaling relation. Seventh column: The median spectroscopic temperature measured for the sample. Eighth column: The measured mass range for the given sample. Mass values for Allen et al. [6] obtained from Mantz et al. [166]. Mass values for Bonamente et al. [37] have been multiplied by a factor of two in order to estimate the M_{500} values for easier comparison with the other data sets.

Table 2.1.

Lin et al. [161] adopt the $M - Y_X$ relation from V09 and apply it down to lower masses and observe $f_{\rm gas}$ to scale with mass as $\alpha = 0.13 \pm 0.03$ and they extend the $f_{\rm gas}$ model to have redshift dependence:

$$f_{gas} \propto M_{tot}^{\alpha}(1+z)^{\zeta}, \tag{2.27}$$

measuring $\zeta = 0.41 \pm 0.04$. If one takes the redshift evolution of Lin et al. [161], and rescales it to the Pratt et al. [236] $\alpha = 0.21 \pm 0.03$, one would obtain $\zeta = 0.66$.

2.6.3   X-Ray Mass Proxy Comparison

Rozo et al. [244, hereafter R12] have recently conducted an examination of the systematic differences between the estimated X-ray masses for shared clusters between the V09, M10, and P11 samples. The results of this analysis are show in Figure 2.4. The V09 and M10 samples share 16 clusters in common, V09 and P11 share 23 clusters in common, and P11 and M10 share 28 clusters in common. At low redshifts, there exists an approximate 10-15% systematic offset in the mass estimates between the different groups. P11 systematically

measure lower masses, M10 systematically measure higher masses, and the V09-measured masses are somewhere in between. At higher redshifts, a systematic trend between the P11 and M10 samples can be identified for the 16 shared clusters with $z > 0.13$. R12 measure the average mass difference to be 45%±5% for these clusters. Aside from the lack of shared
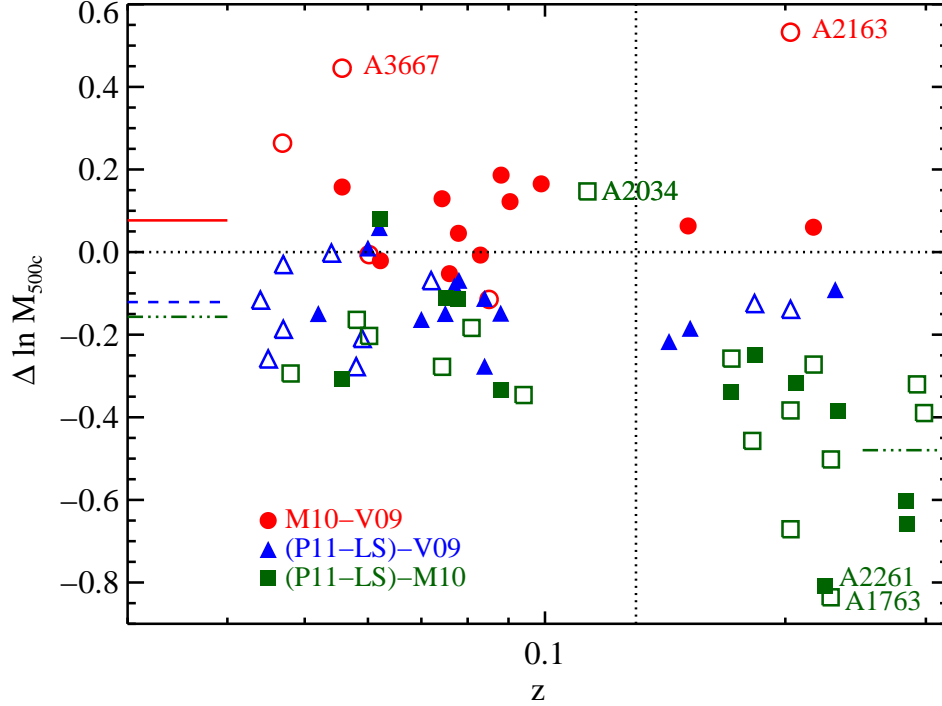
Figure 2.4 A comparison between the differences of the derived mass estimates for individual clusters in the (red) Mantz et al. [166, M10] and Vikhlinin et al. [279, V09], (blue) Planck Collaboration et al. [224, P11-LS] and V09, and (green) P11-LS and M10 cluster samples. P11-LS is abbreviated as P11 in the text. Filled symbols represent relaxed systems, and open symbols represent disturbed systems; the degree of disturbedness is qualitatively determined by the R12 authors. R12 divide the (P11-LS)-M10 analysis into a low-redshift and a high-redshift component, demarcated by the vertical line. Means of the different cluster samples are denoted by the horizontal lines, with the long dotted horizontal line denoting zero difference. Figure from Rozo et al. [245].

hydrostatic cluster mass calibration estimates, the situation is further complicated, because a bias in mass for a particular scaling relation will bias the overdensity radii (e.g. R_{500} or R_{2500}), which determines the aperture within which observables are generally measured. After rescaling the measured M_{gas} values using the ρ_{gas} profile, reported in Piffaretti et al. [221], R12 note that there is no systematic difference between the M_{gas} measurements of the
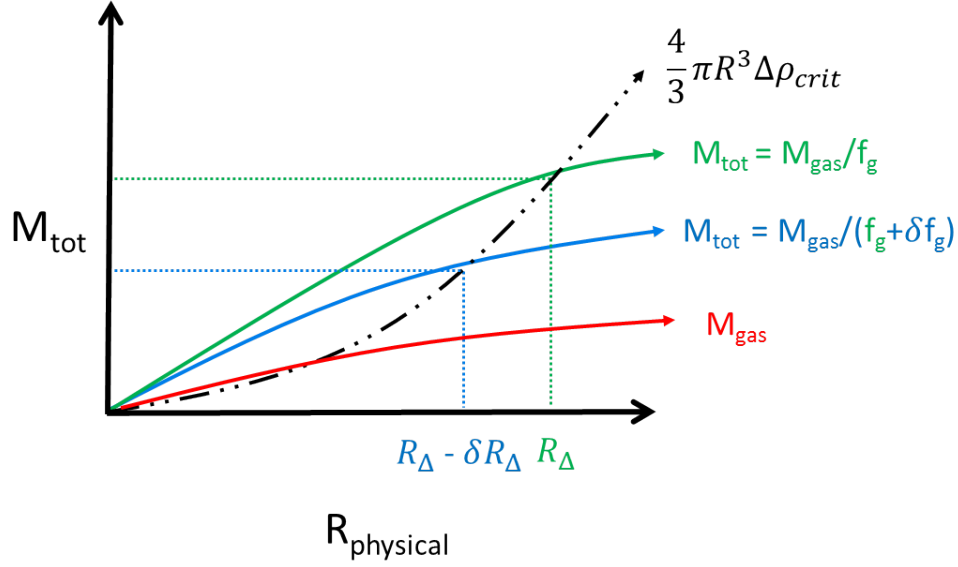
Figure 2.5 Schematic demonstrating how a mass-dependency in f_{gas} affects M_{gas} and M_{tot} measurements. The overdensity radius R_Δ, for a given Δ is determined based on where the mass profile intersects the $4/3\pi R^3 \Delta \rho_c$ black line. For a fiducial $f_{\mathrm{gas}} = f_g$, this is indicated at the intersection of the green dotted lines. When the f_{gas} model changes, so does the over-density radius, as indicated by the blue curve. If one were to naively convert from one f_{gas} model to another without changing the integration radius, one would underestimate the true bias, as indicated by the vertical difference between where the blue curve intersects the blue and the green dotted lines.

various groups.

It is slightly more complicated to compare M_{tot} measurements acquired using different f_{gas} models, because both the aperture and the systematic mass-proxy differences must be accounted for. Figure 2.5 demonstrates why one cannot naively compare two mass measurements using different different f_{gas} models. R12 provide a conversion formula that accounts for aperture effects to compare mass estimates between different mass proxies, which is now reviewed.

As M_{gas} estimates between different groups are consistent with each other, one can conclude that the discrepancies between M_{tot} estimates can be explained by different mass and redshift dependencies of the adopted f_{gas} model. The discrepancy between the mass estimates of two different analyses A and B is defined as the ratio of the M_{tot} estimates for a

particular cluster:

$$b_{AB} = \frac{M_{tot,\Delta,A}}{M_{tot,\Delta,B}} = \frac{R_{\Delta,A}^3}{R_{\Delta,B}^3}. \tag{2.28}$$

Where in converting from M_{tot} to R_Δ, the same reference cosmology is assumed. This assumption holds when comparing the P11 and M10 analyses, as they both use: $\Omega_M = 0.3$, $\Omega_\Lambda = 0.7$, and $H_0 = 70$ km s^{-1} Mpc^{-1}. V09 use $\Omega_M = 0.3$, $\Omega_\Lambda = 0.7$, and $H_0 = 72$ km s^{-1} Mpc^{-1}, which would result in a constant offset of $\sim$5% compared with the P11 and M10 samples.

By matching M_{gas} measurements at the same physical radius between the two groups, and assuming self-similarity ($M \propto R_\Delta^\gamma$), the effect that a systematically different $f_{\rm gas}$ value has on M_{tot}(measured at different radii) can be characterized. First, equating $M_{gas,B}$ with $M_{gas,A}$ at the same $R_{\Delta,A}$, and expressing the result in terms of M_{tot} and $f_{\rm gas}$, yields:

$$M_{gas,B}(@R_{\Delta,A}) = f_{gas,A}(M,z)M_{tot,A} = f_{gas,B}(M,z)M_{tot,\Delta,B}\left(R_{\Delta,A}/R_{\Delta,B}\right)^\gamma. \tag{2.29}$$

This step can be visualized in Figure 2.5 by collapsing a given M_{tot} profile onto M_{gas} and then moving along the curve to match the other M_{gas} estimate. Inserting the calculated $R_{\Delta,A}/R_{\Delta,B}$ ratio into Equation 2.28 yields:

$$b_{AB} = \frac{M_{tot,\Delta,A}}{M_{tot,\Delta,B}} = \left(\frac{f_{gas,B}}{f_{gas,A}}\right)^{3/(3-\gamma)} = \left(\frac{f_{gas,B}}{f_{gas,A}}\right)^{1.67}, \tag{2.30}$$

where in the last step, the substitution $\gamma = 1.2$ has been made, which R12 determine using the Piffaretti et al. [221] ρ_{gas} profile. The result in Equation 2.30 implies that aperture biases will further increase the M_{tot} scaling with different $f_{\rm gas}$ assumptions. This additional bias can be identified as the vertical difference between the intersection of the dotted green and blue lines with the blue curve. If the $f_{\rm gas}$ assumptions between two groups are the same, of course, $b_{AB} = 1$.

To summarize, R12 find that once aperture biases have been accounted for, M_{gas} measurements between V09, P11, and M10 are consistent with each other. Therefore, the systematic differences in the mass measurements between the different groups can be derived from the equivalence of the M_{gas} measurements and a known systematic difference in the $f_{\rm gas}$ as-

sumption. With a measured $M_{tot,A}$ for a given cluster and $f_{\mathrm{gas},A}$ model, equation 2.30 shows how to predict the $M_{tot,B}$ estimate determined using an $f_{\mathrm{gas},B}$ model. Keep in mind that systematic differences in $M_{tot,\Delta}$ are measured at different R_{Δ} values since we want to keep Δ the same between the two samples. Referring again to Figure 2.5, M_{tot} must be evaluated as some point along the black dash-dotted line. This equation will be used later in Section 4.6.1 when the *Bolocam* results are compared with other scaling relations analyses.

2.6.4   Gravitational Lensing Mass Estimates

Pressure-derived scaling relations are relatively low-scatter but are potentially biased. Because gravitational lensing is a measure of total mass, lensing data should ideally be able to calibrate this bias. While several weak lensing studies have been conducted to characterize the degree of X-ray hydrostatic bias, they do not all agree with each other (see, for example, Applegate et al. [10] and Okabe et al. [207]).

Marrone et al. [171] and Marrone et al. [172] measure the exponential scaling of the SZE signal using both strong-lensing mass estimates and weak-lensing mass estimates, respectively. Clusters were selected from the LoCuSS cluster catalog (see Appendix A) and the SZE observations were performed using the Sunyaev-Zel'dovich Array (SZA) which was introduced in Section 2.3.2. The Marrone et al. [171] strong-lensing sample consists of 14 galaxy cluster with a median redshift, $\langle z \rangle = 0.222$. Assuming a scaling of $M_{\Delta} \propto Y_{\Delta}^{\beta}$, they measure $\beta = 0.47^{+0.24}_{-0.20}$ with an intrinsic scatter of $32 \pm 4\%$ at a fixed physical integration raduis of 350 kpc for their adopted cosmology. This is about 50-75% the size of R_{2500} for the clusters in their sample. This radius was primarily chosen because strong lensing is mostly sensitive to the core regions of galaxy clusters. The Marrone et al. [172] weak-lensing sample, in comparison, consists of 18 galaxy clusters from the LoCuSS sample with redshifts between $0.15 < z < 0.3$. Their results give an exponential scaling that steepens at smaller r_{Δ}, with $\beta = \left[0.44^{+0.12}_{-0.11}, 0.48^{+0.11}_{-0.11}, 0.55^{+0.14}_{-0.13} \right]$ at $\Delta = [500, 1000, 2500]$—each one shallower than self-similar, $\beta = 3/5$. They measure the intrinsic scatter to be approximately $20\% \pm 10\%$, which they suggest is so large due to variations in cluster morphology. At fixed Y_{spher}, they measure the mass of the undisturbed cluster to exceed that of the disturbed clusters by $[41 \pm 6\%, 28 \pm 5\%, 13 \pm 6\%,]$ at $\Delta = [500, 1000, 2500]$, respectively.

Chapter 3

Bolocam and *Chandra* Observations of the BOXSZ Cluster Sample

Starting in 2011 I devoted myself full-time to *Bolocam* data analysis and I expanded the suite of reduced *Bolocam* observations from 5 to 45 clusters. Following the Sayers et al. [255] proof-of-methodology paper, our work entered an exciting period of scientific collaboration and publication. With our large sample of reduced observations, we were able to explore and reduce various systematic biases in the data caused by aggressive atmospheric filtering, calibration uncertainties, and radio source contamination.

3.1 BOXSZ: The *Bolocam* X-ray/Sunyaev-Zel'dovich Sample

The *Bolocam* X-Ray SZ (BOXSZ) sample is a compilation of 45 clusters, with existing *Chandra* data, observed with *Bolocam* at 140 GHz (Glenn et al. [100], Haig et al. [109]). *Bolocam* is a 144-element bolometric camera with a 58" FWHM PSF at the SZE-emission-weighted band center of 140 GHz. This data was collected over five years (from Fall 2006 to Spring 2012) in 14 different observing runs at the Caltech Submillimeter Observatory. The relevant observational information is included in Table 3.1, and most of the cluster properties relevant to this analysis are included in Table 3.3.

Bolocam is well-suited to observe intermediate redshift clusters, and therefore many of the clusters in the BOXSZ sample were selected with redshifts between $0.3 \lesssim z \lesssim 0.6$. In

Table 3.1.   Observational Parameters of the BOXSZ Sample.

Catalog	ID	RA (J2000)	DEC (J2000)	SZE S/N	SZE RMS ($\mu K_{CMB} - arcmin$)	SZE t_{int} (hours)
Abell	2204	16:32:47.2	+05:34:33	22.3	18.5	12.7
Abell	383	02:48:03.3	-03:31:46	9.6	18.9	24.3
Abell	209	01:31:53.1	-13:36:48	13.9	22.3	17.8
Abell	963	10:17:03.6	+39:02:52	8.3	35.7	11.0
Abell	1423	11:57:17.4	+33:36:40	5.8	31.7	11.5
Abell	2261	17:22:27.0	+32:07:58	10.2	15.9	17.5
Abell	2219	16:40:20.3	+46:42:30	11.1	39.6	6.3
Abell	267	01:52:42.2	+01:00:30	9.6	23.0	20.7
RX	J2129.6+0005	21:29:39.7	+00:05:18	8.0	23.7	16.0
Abell	1835	14:01:01.9	+02:52:40	15.7	16.2	14.0
Abell	697	08:42:57.6	+36:21:57	22.6	17.4	14.3
Abell	611	08:00:56.8	+36:03:26	10.8	25.0	18.7
MACS	J2140.2-2339	21:40:15.1	-23:39:40	6.5	27.3	12.8
Abell	S1063	22:48:44.8	-44:31:45	10.2	48.6	5.5
MACS	J1931.8-2634	19:31:49.6	-26:34:34	10.1	28.7	7.5
MACS	J1115.8+0129	11:15:51.9	+01:29:55	10.9	22.8	15.7
MACS	J1532.8+3021	15:32:53.8	+30:20:59	8.0	22.3	14.8
Abell	370	02:39:53.2	-01:34:38	12.8	28.9	11.8
MACS	J1720.2+3536	17:20:16.7	+35:36:23	10.6	23.5	16.8
Cl	0024+17	00:26:35.8	+17:09:41	3.3	26.6	8.3
MACS	J2211.7-0349	22:11:45.9	-03:49:42	14.7	38.6	6.5
MACS	J0429.6-0253	04:29:36.0	-02:53:06	8.9	24.1	17.0
MACS	J0416.1-2403	04:16:08.8	-24:04:14	8.5	29.3	7.8
MACS	J0451.9+0006	04:51:54.7	+00:06:19	8.1	22.7	14.2
MACS	J1206.2-0847	12:06:12.3	-08:48:06	21.7	24.9	11.3
MACS	J0417.5-1154	04:17:34.3	-11:54:27	22.7	22.7	9.8
MACS	J0329.6-0211	03:29:41.5	-02:11:46	12.1	22.5	10.3
MACS	J1347.5-1144	13:47:30.8	-11:45:09	36.6	19.7	15.5
MACS	J1311.0-0310	13:11:01.7	-03:10:40	9.6	22.5	14.2
MACS	J2214.9-1359	22:14:57.3	-14:00:11	12.6	27.3	7.2
MACS	J0257.1-2325	02:57:09.1	-23:26:04	10.1	39.0	5.0
MACS	J0911.2+1746	09:11:10.9	+17:46:31	4.8	33.5	6.2
MACS	J0454.1-0300	04:54:11.4	-03:00:51	24.3	18.2	14.5
MACS	J1423.8+2404	14:23:47.9	+24:04:43	9.4	22.3	21.7
MACS	J1149.5+2223	11:49:35.4	+22:24:04	17.4	24.0	17.7
MACS	J0018.5+1626	00:18:33.4	+16:26:13	15.7	21.0	9.8
MACS	J0717.5+3745	07:17:32.1	+37:45:21	21.3	29.4	12.5
MS	2053.7-0449	20:56:21.0	-04:37:49	5.1	18.0	18.7
MACS	J0025.4-1222	00:25:29.9	-12:22:45	12.3	19.7	14.3
MACS	J2129.4-0741	21:29:25.7	-07:41:31	15.2	21.3	13.2
MACS	J0647.7+7015	06:47:49.7	+70:14:56	14.4	22.0	11.7
MACS	J0744.8+3927	07:44:52.3	+39:27:27	13.3	20.6	16.3
MS	1054.4-0321	10:56:58.5	-03:37:34	17.4	13.9	18.3
RXJ	0152.7-1357	01:52:41.1	-13:58:07	10.2	23.4	9.3
CLJ	1226.9+3332	12:26:57.9	+33:32:49	13.0	22.9	11.8

Note. — BOXSZ observation data. Columns give the catalog and ID, X-ray centroid coordinates (J2000), the peak SZE /N in the optimally filtered images (see Sayers et al. [253] for details on how this was calculated), RMS noise level of the SZE images, and the total Bolocam integration time.

total, the BOXSZ sample spans from $0.15 \leq z \leq 0.9$, with a median redshift of $\langle z \rangle = 0.42$. This redshift distribution is similar to the initial ground-based SZE-selected catalogs of both the SPT, $\langle z \rangle = 0.57$ (Song et al. [263]), and the Atacama Cosmology Telescope, $\langle z \rangle = 0.44$ (Menanteau et al. [182]). In contrast, the early *Planck* SZE catalog has a median redshift of $\langle z \rangle = 0.15$ (Planck Collaboration et al. [223]), while the recently released 2013 *Planck* SZE catalog has a median redshift of $\langle z \rangle = 0.22$ (Planck Collaboration et al. [228]). In addition to redshift, many of the clusters in the BOXSZ sample were selected based on their higher-than-average X-ray spectroscopic temperatures, T_X, given the expected correlation between T_X and SZE brightness. A few clusters, however, were chosen due to their membership in the CLASH and the MACS high redshift catalogs, and the BOXSZ sample includes both the complete CLASH cluster catalog (Postman et al. [233]), and the complete MACS cluster catalog of the 12 most luminous clusters with $z > 0.50$ (Ebeling et al. [71]). However, the BOXSZ sample as a whole lacks a well-defined selection function. Therefore, selection effects for the SZE scaling relations are modeled and explored in Section 4.3.

BOXSZ SZE data has already been used in several publications with *Bolocam* team members as co-authors. Two results have come directly out of our data analysis procedure: one on the calibration of millimeter-wave planetary fluxes (Sayers et al. [254]) and one on radio source contamination in the SZE maps (Sayers et al. [257]). We observed two of the Planck Early Release cluster candidates, PLCKESZ G115.71 and PLCKESZ G189.84, and we confirmed the former to be a cluster (Sayers et al. [253]). Several studies use *Bolocam* data to cross-calibrate mass estimates of other observable probes. Zitrin et al. [305] use *Bolocam* data to calculate an upper-limit on a possibly lensed cluster by Abell 383. Umetsu et al. [277] and Medezinski et al. [180] calibrate the mass profiles of MACSJ 1206.2 and MACSJ 0717.5, respectively, using a combination of *Bolocam* SZE, X-ray and lensing data. Morandi et al. [191] perform a joint Bayesian analysis, using the same observables to constrain the triaxiality and non-thermal pressure profile of Abell 1835. By combining *Bolocam* 140 GHz and 268 GHz data with OVRO/BIMA/SZA 90 GHz data, Mroczkowski et al. [194] find the best-fit spectral model of MACSJ 0717.5 to prefer a kinetic SZE component by more than 2σ. Most recently, Sayers et al. [256] characterize the average pressure profile of the sample, obtaining results that suggest a shallower pressure profile at large radii than predicted by simulations.
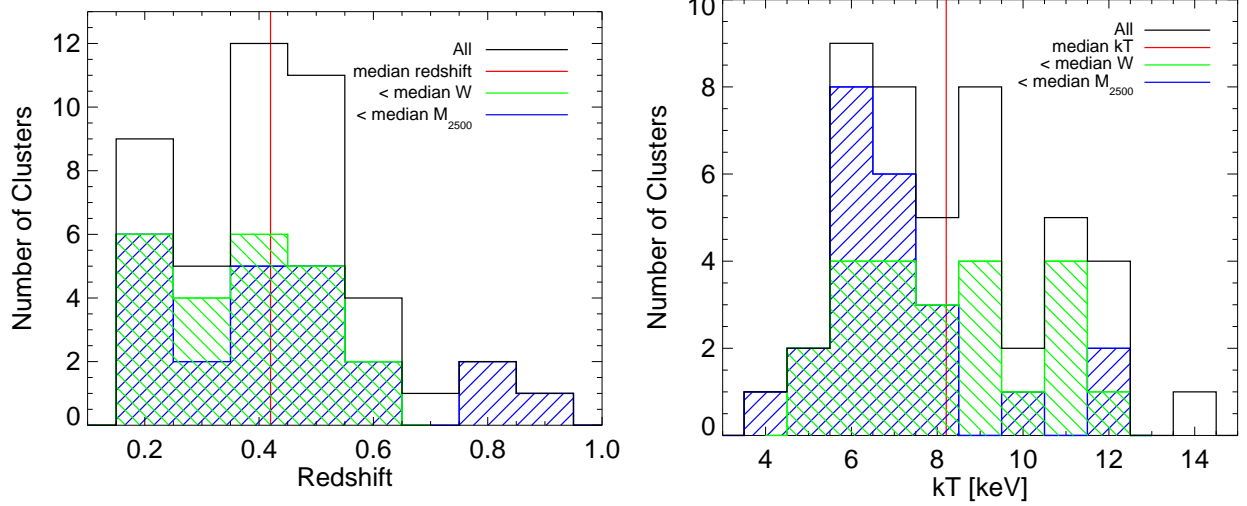
Figure 3.1 Redshift (left) and X-ray temperature (right) distributions for the BOXSZ cluster sample. Black histograms depict the entire sample with the red line indicating the median value. Green histograms depict the clusters with centroid shift parameters below $w = 7.2 \times 10^{-2}$, which have therefore been classified to be the most relaxed. Blue histograms depict the 23 lowest mass clusters of the sample, with $M_{2500} < 3.03 \times 10^{14} M_\odot$. Note that in the left-hand plot the disturbed and relaxed samples are approximately uniformly distributed in redshift. The high-mass and low-mass samples are also approximately uniformly distributed in redshift, with three low-mass high-redshift outliers. In the right-hand plot, it can be seen that there is almost no correlation between the disturbedness measure and the X-ray temperature.

Some of the analyses are discussed in further detail in Chapter 5.

3.2 BOXSZ X-ray Data and Mass Estimation

X-ray mass estimates are utilized both for the BOXSZ scaling relations and to define an aperture within which to integrate the SZE signal. Of the 238 clusters in the Mantz et al. [166, hereafter M10] sample, 32 clusters overlap with the BOXSZ sample, and 13 additional clusters were added specifically to complete the X-ray observations for the BOXSZ catalog. X-ray luminosities are measured between 0.1 and 2.0 keV and M_{gas} values are calculated using semi-analytical methods described in [165]. The XSPEC-MEKAL code is used to fit to a single cluster temperature, excluding the core, between 0.15 and 1.0 R_{500}.

The M_{tot} values for this work are directly calculated from M_{gas}, using the Allen et al. [6,

hereafter A08] f_{gas} calibration, with $f_{\mathrm{gas}}= 0.1104$, discussed in Section 2.6.1.2:

$$M_{tot}(r_\Delta) = \frac{M_{\mathrm{gas}}(r_\Delta)}{f_{\mathrm{gas}}(r_\Delta)} = \frac{4}{3}\pi\Delta\rho_{\mathrm{cr}}(z)r_\Delta^3. \tag{3.1}$$

In deriving M_{tot} from M_{gas}, an additional 8% global systematic gaussian uncertainty in f_{gas} is marginalized over. As the uncertainty in M_{gas} depends on the uncertainty in $r_\Delta \propto M_{tot}^{1/3}$, the fractional error for the two measurements is approximately the same.

Centroid variance, w_{500}, is an indicator of how much the body of a cluster is displaced from its core. Mohr et al. [188] first introduce this method to characterize local cluster X-ray morphology. Specifically, the w_{500} parameter measures the standard deviation of the projected separation between the cluster X-ray peak and the surface brightness centroids of a series of concentric apertures, from 0.05 R_{500} to R_{500}, centered at the X-ray peak and normalized to R_{500}. Using N-body simulations, Poole et al. [232] verify that w_{500} is an extremely sensitive indicator of a cluster's dynamical state. We have therefore adopted w_{500} as a measure of the dynamical state of the BOXSZ clusters. The w_{500} measurements have been calculated using the method described in Maughan et al. [177, 175] and are presented in Table 3.3. The temperature and redshift distributions of the BOXSZ sample, and their associated subsamples, split based on the median values of w_{500} and M_{2500}, are plotted in Figure 3.1.

3.3 Data Collection and Reduction

Bolocam data reduction is extensively explained in Sayers [252] and Sayers et al. [255]. The general aspects of this process are reviewed below, including any pertinent changes, to the extent that they provide a picture of the nature of the final data product.

3.3.1 Scan Pattern

Approximately 50-100 10-minute observations were performed for each BOXSZ cluster using a lissajous scan pattern. This observing method enables 100% on-source observing efficiency. The telescope is scanned in R.A. and Dec. with two asynchronous scan periods of 6.28
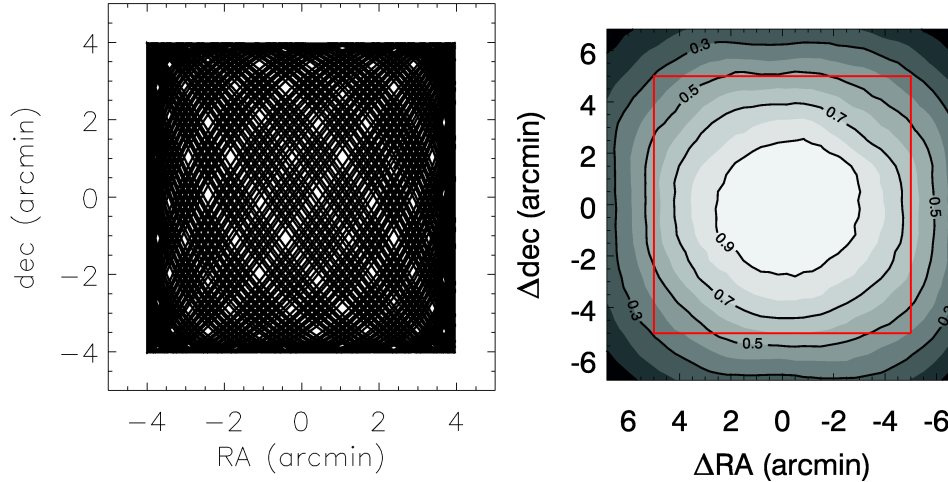
Figure 3.2 Left: Typical lissajous scan pattern used to observe galaxy clusters with *Bolocam*. Right: Integration time per pixel relative to the maximum integration time for MACSJ 0454.1-0300. The red box denotes the region, $10'$/side, over which the deconvolution of the pipeline transfer function yields reliable results. Taken from Sayers et al. [255].

seconds and 8.89 seconds, each with an amplitude of 4 arcmin. The scan periods alternate between R.A. and Dec. every other observation. The mean scan speed is approximately 4 arcmin per second, with a peak scan speed of about 6 arcmin per second while crossing the cluster. The observing efficiency for a sample cluster and an image of the scan pattern are displayed in Figure 3.2.

3.3.2 Data Quality Cuts

Cuts to the data are performed based on the AC/DC characterization of individual bolometer timestreams. The overall loading and calibration of the bolometers can be characterized by the absolute, DC signal, and the imaging data lies in the AC signal, at frequencies higher than the fundamental scan frequencies A sample diagnostic plot of this process for a single observation is given in Figure 3.3, and an example of some of the cuts that are performed on the data are given in the legend. The first and second values give the lower and upper range of passing values, and the third item is the measurement for the particular observation. This particular observation passed all of the displayed cuts, except for the median RMS AC bolometer signal, which is measured to be 0.290 V. The time-ordered median DC voltage across all bolometers is given in the upper plot. Due to the high emissivity of atmospheric

water vapor, the *Bolocam* bolometer-calibration is responsive to changes in the atmospheric water vapor. However, because cluster observations can still be performed under a variety of atmospheric conditions, stringent cuts are not placed on the absolute level of the DC signal. The power spectral density (PSD) is given in the lower plot. Here, the given observation has a noticeably higher level of low-frequency noise compared to the median, and therefore it is cut. As a reference point, the bandwidth used for observations is between 250 mHz and 2 Hz. The number of observations which are cut for a particular observating run is highly sensitive to the overall observing conditions of the run. Generally, fewer than 20 observations are cut for a "good" run.

Cuts are similarly performed on individual bolometer timestreams, averaged over all observations, to identify if particular bolometers are not functioning properly for a given run. Of the 144 bolometers that are read-out on the *Bolocam* 140 GHz focal plane, 6 are not optically coupled ("dark"), and 24 are non-operational. Of the 114 operational bolometers, up to 10 bolometers can be cut from a particular observing run depending on individual bolometer performance. Because the bolometers are read out in six independent hextants, this process also allows us to trouble-shoot if there are any electronic problems with the read-out for a particular hextant.

3.3.3   Synchronization and Pointing Correction

Excessive pointing and timing uncertainty will effectively increase the beam FWHM, when large amounts of data are coadded. Both effects are modeled and removed from the data. The *Bolocam* data acquisition clock has a long time-scale drift and is actively synchronized to the GPS-synchronized telescope on a nightly basis. Figure 3.4 depicts how the timing offset can change throughout the course of the night. The y-axis is in units of the 50Hz sample rate. Therefore, a change in 50 units over the course of the night would cause an overall shift of 1 second in synchronization. As the telescope scans approximately 4 arcminutes per second, this offset could significantly smear if the beam if not accounted for. The data is corrected using a simple linear time-drift model, which can be constructed from the timing uncertainty indicated by the red line in Figure 3.4.

There are two stages to the pointing correction: one at the bolometer level and one at
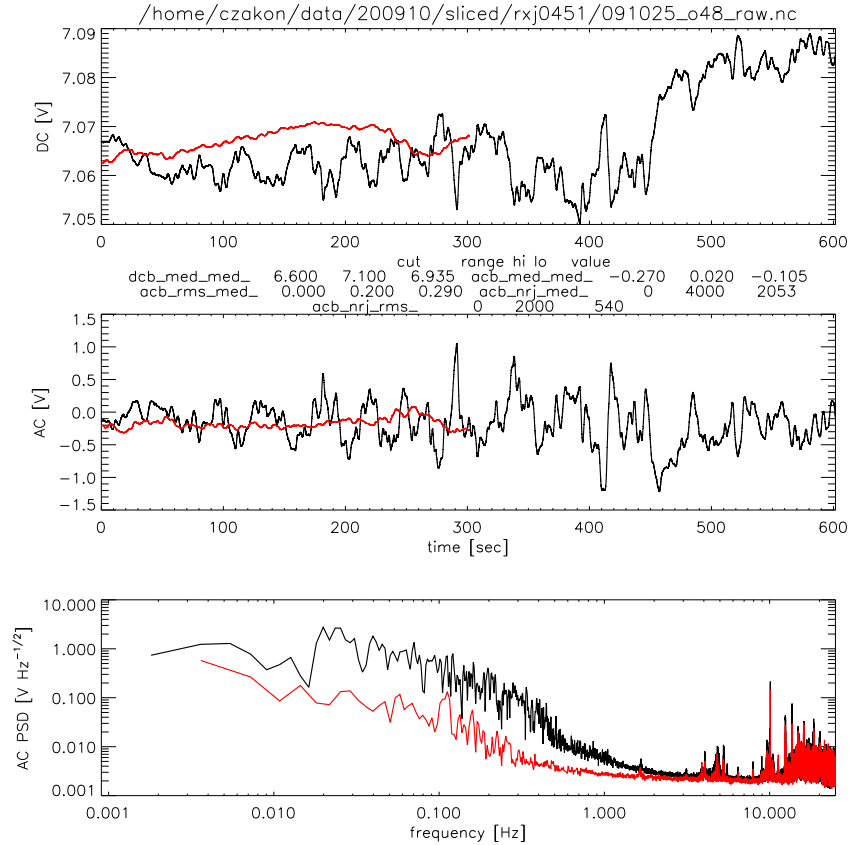
Figure 3.3 A sample diagnostic plot used to remove one of the RXJ 0451 (aka MACSJ 0451.9+0006) observations from the final cluster coadds. From top to bottom: DC signal in Volts, AC signal in Volts, and AC noise power spectral density in $\mathrm{Volts/Hz}^{1/2}$ for the October 2009 observing run. Red lines indicate the signal averaged over all observations (including the 5-minute pointing observations), and the black lines represent a particular observation which was cut from the final coadds. One can see that the sky noise for this particular observation is rather severe.
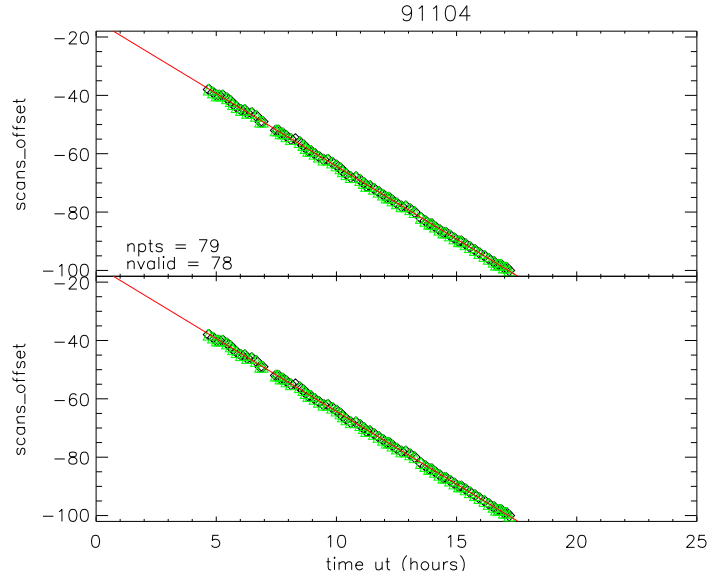
Figure 3.4 Sample diagnostic plot used to model the clock drift for each night of observation. The y-axis is in units of the data sample rate: 1 unit represents 10 ms. The clock has drifted a bit more than a second over the course of the night, and this is well-modeled by a linear fit. Uncorrected, this would result in a systematic error on the pointing correction that is time-dependent over the night. Given the scan speed, this error would be large compared to the beam FWHM and effectively smear the FWHM for coadded observations.

the telescope level. Pointing models are constructed by performing two consecutive 5-minute observations of stationary millimeter-bright point sources (generally quasars) approximately once every fourth observation. The centroids of the pointing maps determine the position of the center of the focal plane on the sky with respect to the telescope coordinates. The relative positions of individual bolometers with respect to the center of the focal plane are determined using beam maps of the nightly 20-minute observations of a calibration source: either Uranus, Neptune, or a secondary calibrator given in Sandell [251]. Flux calibration is discussed separately in Section 3.3.4.

As *Bolocam* is mounted at the Cassegrain focus of the telescope, it must be dismounted every time another instrument is scheduled to observe at that position. The mounting of the warm optics has fairly loose tolerances, which results in slightly different optical path for each mount/dismount cycle. This is accounted for by constructing pointing models for each observation run relative to an ensemble average over many runs. In Figure 3.5, one can observe that the overall trend in pointing has been that the beams of the bolometers in the
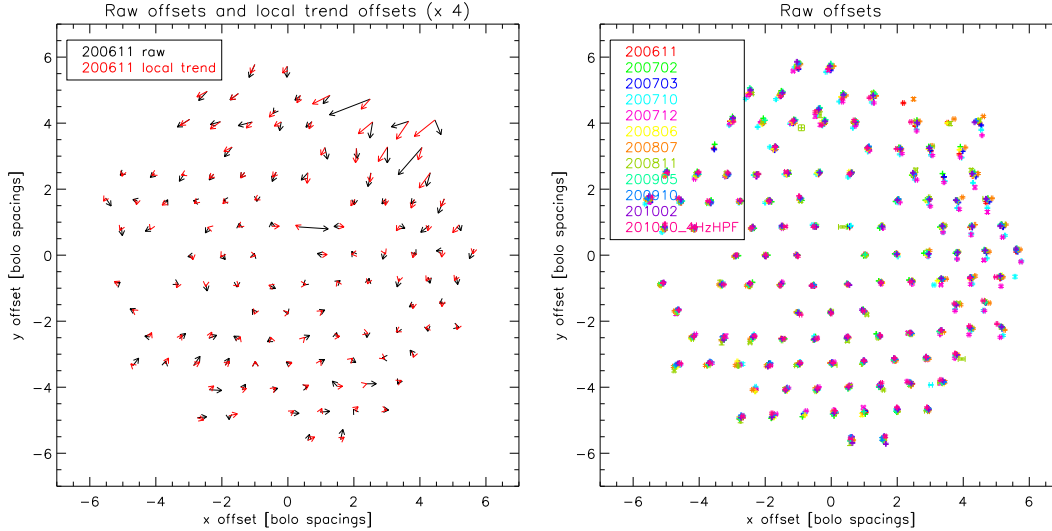
Figure 3.5 Individual bolometer pointing corrections superimposed with the relative bolometer positions on the *Bolocam* focal plane in units of the mean bolometer spacing for the November 2006 observing run. Left: Bolometer position offsets magnified by a factor of 4. Black: the raw offsets. Red: the local trend in offsets, obtained by averaging over all bolometers within 1.5 bolometer spacings of the given position. Right: the raw offsets over all observing runs from November 2006 to October 2010. The bolometer positions are generally consistent from run-to-run, although the upper-right hextant appears to experience more positional variation than the others.

upper right corner of the focal plane are shifted towards the center. Note that the trend is magnified by a factor of four in the plot for visibility. The right-hand plot depicts the overall trend of the pointing offsets through several different observing runs.

The second stage of pointing corrections occurs at the telescope stage. In general, these are more significant than the focal plane pointing corrections. A sample nightly-pointing diagnostic plot is given in Figure 3.6 and Figure 3.7 shows the positions of the pointing sources for MACSJ 0744.8 over an entire observing run in 2009. Pointing generally does not vary from night-to-night, and these diagnostics are solely performed as an additional quality check. By far the largest systematic pointing offset is caused by offsets in the telescope and source coordinates which vary telescope position. The left-hand plot of figure 3.8 depicts a relatively rare situation with a gross offset of approximately 30 arcseconds in the azimuthal direction (which can also be identified in Figure 3.6). This is most likely due to an incorrect telescope setting and, if left uncorrected, this offset would source a significant amount of effective beam smearing. Fortunately, as can be seen in the right-hand plot of the same
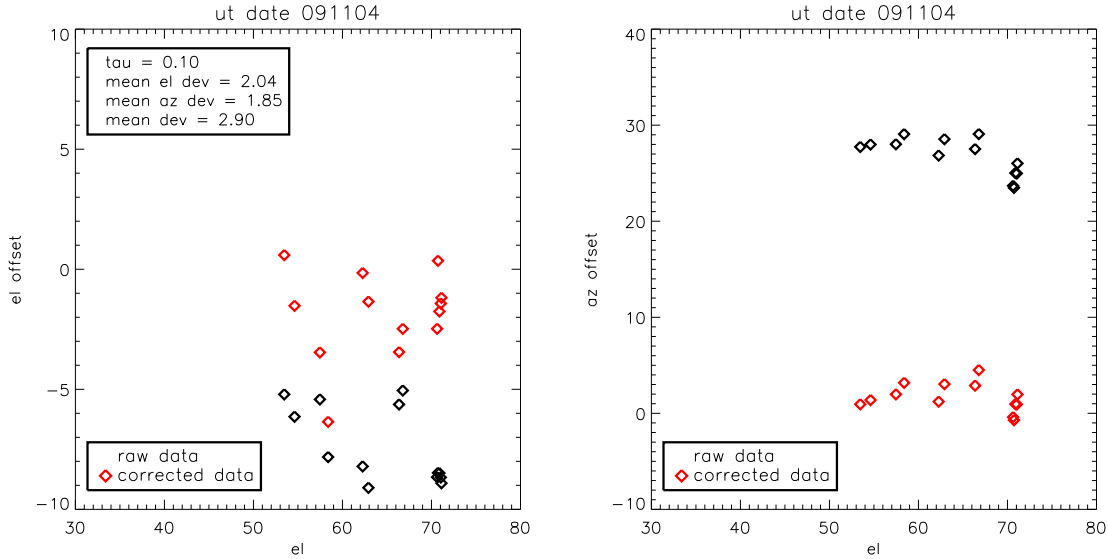
Figure 3.6 Diagnostic plot for the nightly pointing of MACSJ 0744.8 on the night of November 4th, 2009. (Left) elevation pointing offset, (right) azimuthal pointing offset, (black diamonds) raw data, and (red diamonds) corrected data. Note the overall 30 arcsecond pointing offset in azimuth. When corrected with the pointing model, the residuals drop to about 5 arcseconds.

figure, these pointing erors can be well-modeled and removed. These models are accurate to ~5 arcseconds, and this pointing uncertainty produces an effective broadening of the point-spread function (PSF). Specifically, an effective PSF is determined by convolving *Bolocam*'s nominal PSF, which has a full-width at half-maximum (FWHM) of 58 arcseconds, with a two-dimensional Gaussian profile with $\sigma = 5$ arcsec. Fortunately, this broadening of the PSF due to pointing uncertainty is small, and it does not have a significant impact on the derived results (especially for resolved objects like galaxy clusters).

3.3.4   Flux Calibration

Flux calibration is performed with nightly 20-minute observations of Uranus and Neptune, together with other secondary calibrators given in Sandell [251]. The absolute fluxes of Uranus and Neptune, which are heated to about 110 Kelvin by the Sun, were determined using the models of Griffin & Orton [106], rescaled based on an improved WMAP calibration [209, 117, 286]. The WMAP measurements demonstrate the Wright [295]/Rudy et al. [247] model to be systematically high by about 5-7%. The full methodology is described in detail
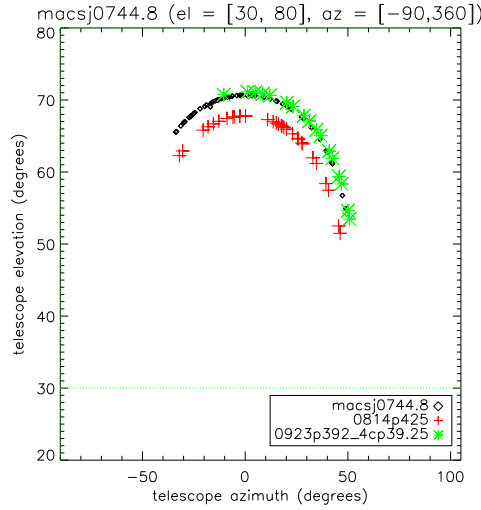
Figure 3.7 Telescope pointing for all of the observations of MACSJ 0744.8 and the associated pointing sources. This data is used as the basis for the pointing corrections depicted in Figure 3.8.
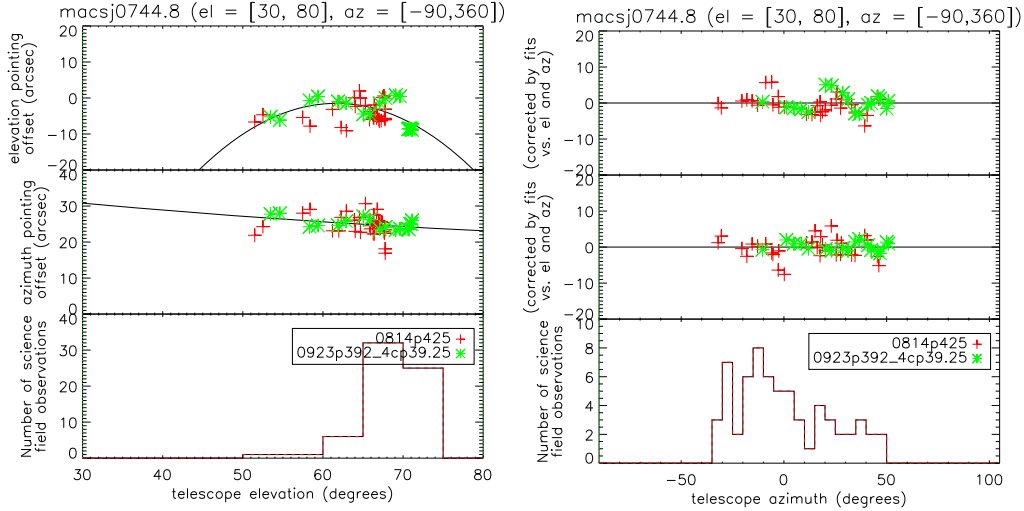
Figure 3.8 (Left) Elevational- and (right) azimuthal-dependence of the observational pointing error for MACSJ 0744.8 in a 2009 observing run. Black lines depict the best-fit pointing models. (Bottom panels) Histograms of the total number of observations at a particular elevation, left, or azimuth, right. (Top panels) Elevation pointing offset either uncorrected, left, or corrected, right, with the best-fit pointing models. (Middle panels) Azimuthal pointing offset either uncorrected, left, or corrected, right, with the best-fit pointing models.
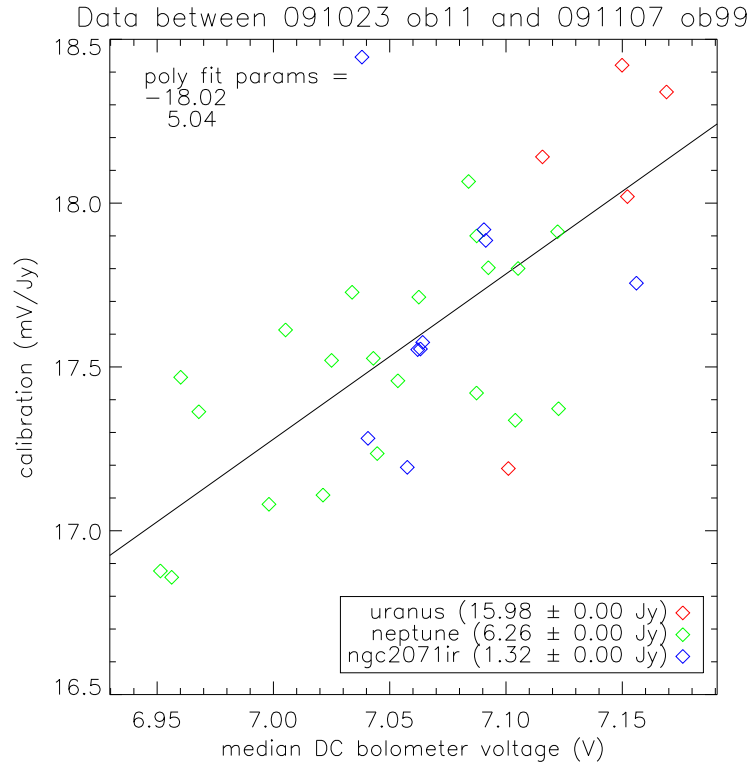
Figure 3.9 Flux calibration (mV/Jy) for the October 2009 observation run as a function of median DC bolometer voltage. For this particular run, we observed Uranus (red diamonds), Neptune (green diamonds), and a secondary calibration source (blue diamonds) given in Sandell [251] . The estimated flux is given in the legend, and the error bars are generally larger than 0.00 for sources with unknown flux. Note how both the responsivity and voltage decrease with atmospheric loading, making the flux-calibration a linear function of atmospheric loading.
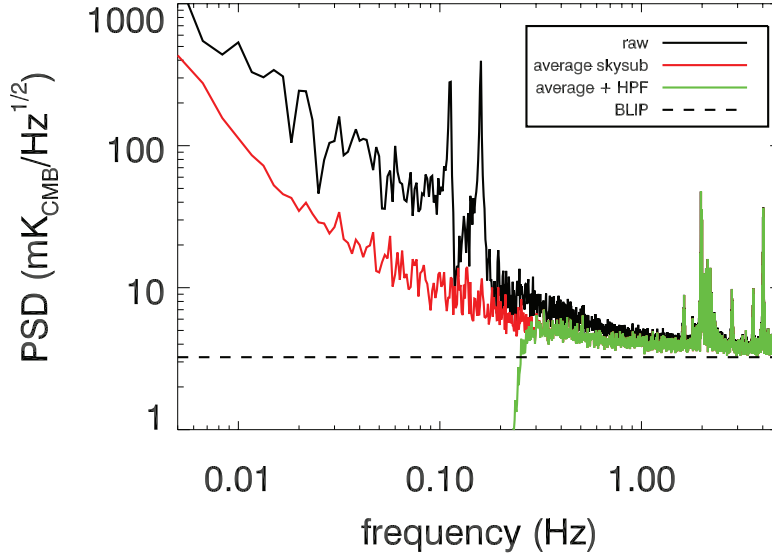
Figure 3.10 Measured timestream noise PSD for a typical bolometer in $\mathrm{mK_{CMB}}/\sqrt{\mathrm{Hz}}$. Black line: raw data, where the fundamental lissajous scan frequencies can be seen above the atmospheric noise. Red line: Noise PSD after removal of the instantaneous bolometric response-weighted median across the FOV. The data are then high-pass filtered data at 250 mHz (green line). The spectral lines at high frequencies are due to the readout electronics, where there is very little astronomical signal. Dashed line: estimated atmospheric background limited noise level (BLIP). More details can be found in Sayers et al. [255].

in Sayers et al. [254], and the final overall uncertainty on the *Bolocam* flux calibration is approximately 5%.

Atmospheric loading decreases the bolometer resistance, and since the bolometers are biased with a constant current, this will also decrease the peak voltage response for a bolometer to a given source. A sample flux calibration diagnostic plot is given in Figure 3.9, demonstrating the linear relation between responsivity and median DC voltage.

3.3.5 Atmospheric Noise Removal/Transfer Function/Mapping

Atmospheric brightness fluctuations are removed from the data-streams of each detector by first subtracting the response-weighted mean detector signal and then applying a 250 mHz high-pass filter. The individual detector responses used in this process are determined at the particular lissajous scan frequencies.This process removes some cluster signal and is weakly dependent on cluster shape. The effect that this has on the data PSD can be seen in Figure 3.10. The black line traces the raw bolometer PSD. The fundamental scan periods can be

identified at 1/6.28 s = 160mHz and 1/8.89 s = 112mHz. The amplitude of the signal at these frequencies is due to the changing loading due to the movement in elevation during scanning. The red trace depicts the noise PSD, once the bolometer response-weighted median is removed from the time stream. Finally, a 250 mHz HPF is applied to the time-ordered data and the green trace depicts the fully-filtered PSD.

The pipeline transfer function must be determined in order to create an unbiased cluster map, which can be directly compared to a given cluster model. The transfer function is also used to compare model profiles directly to the processed data. As described in detail in Sayers et al. [255], an iterative process is used to determine the signal transfer function separately for each cluster. Each iteration involves processing a parametric model through the data reduction pipeline, computing a signal transfer function by comparing the output shape of this model to the input shape, fitting a parametric model to the data (convolved by this transfer function), and then using this parametric fit for the input to the next iteration. This process converges quickly—generally within two iterations. The azimuthally-averaged transfer function for MS 0451.6-0305 is depicted in Figure 3.11. Because the model clusters are, by design, not intended to fit small-scale modes, they have little signal in this regime, and therefore the transfer function has a large degree of uncertainty for smale-scalle modes. The transfer function is therefore set equal to one for modes smaller than 1.33 arcmin. For large scale modes, there is very little *Bolocam* SZE signal, and the transfer function goes to zero. In order to prevent significant amplification of large-scale noise, deconvolved images are reduced to 10×10 arcminutes in size, compared with the processed images, which are 14×14 arcminutes in size.

3.4 Noise Characterization and Point Source Removal

The scaling relation analysis depends critically on accurate noise characterization. This is because a misestimate of the noise will not only affect the derived uncertainty estimates, but will also bias the determination of the best-fit scaling relation. The *Bolocam* SZE cluster images contain noise from a variety of sources: atmospheric fluctuations, instrument noise, flux calibration, primary CMB anisotropies, and emission from the non-uniform distribution
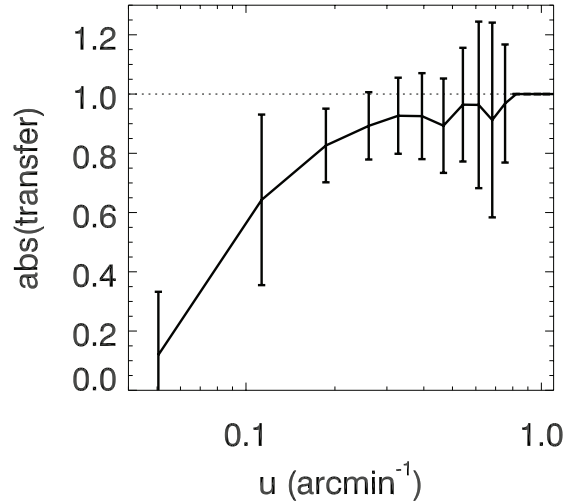
Figure 3.11 The magnitude of the azimuthally-averaged transfer function for MS 0451.6-0305 as a function of Fourier wavenumber $u = 1/\lambda$. At large scales, the error bars are good indicators of the rms azimuthal variation of the map. At small scales, however, the cluster model has little signal/constraining power and the measurement noise increases due to numerical uncertainty. The transfer function is therefore set equal to 1 at $u > 0.75 \text{arcmin}^{-1}$. The full 2-dimensional transfer function is used for the *Bolocam* data analysis. More details can be found in Sayers et al. [255].

of fore- and background galaxies. Section 3.5.1 reviews how additional uncertainties due to the deconvolution of the signal transfer function are accounted for. Section 3.7 characterizes the uncertainties of the Y_{SZ} estimates that arise from the uncertainty in the overdensity radius used for integration.

Noise realizations are created for each cluster by multiplying a randomly chosen subset of half of the ∼50-100 observations by −1 prior to coadding them together. A total of 1000 such jackknife noise realizations are created for each cluster. The noise realizations contain no astronomical signal but retain the statistical properties of the atmospheric and instrumental noise. To account for noise from primary CMB fluctuations and unresolved galaxies, a random realization of the 140 GHz astronomical sky is added to each noise realization, using the measured angular power spectrum from the SPT [138, 241] under the assumption that the fluctuations are Gaussian. The resulting noise realizations are statistically indistinguishable from *Bolocam* maps of blankfields, thereby verifying that this noise model provides an adequate description of the *Bolocam* data. These noise realizations provide the basis to which all of the modeled astronomical noise, discussed below, is added.

Dusty star-forming regions and radio-bright point sources will bias Y_{SZ} measurements low. Fortunately, the 140 GHz regime is located in a valley of low background contamination between radio and thermal dust emission. The frequency dependence of the flux density, S_ν, for radio sources can be approximated as:

$$S_\nu \propto \nu^{-\alpha}, \tag{3.2}$$

where $0.5 \lesssim \alpha \lesssim 1.4$ for the BOXSZ sample. The flux density of dusty thermal sources can be characterized with a gray-body spectrum (not quite in the Raleigh-Jeans limit), peaking at 10's of Kelvin,

$$S_\nu \propto \nu^{\alpha}, \tag{3.3}$$

where typically $alpha \gtrsim 2$. Several of the clusters in the BOXSZ sample contain signal from bright radio galaxies that are not accounted for in the SPT power spectrum. In particular, the brightest cluster galaxy (BCG) is often a bright radio emitter, and this emission will systematically reduce the magnitude of the SZE decrement towards the cluster.

A full description of the methodology in which we systematically characterize and subtract the flux of these bright radio galaxies is given in Sayers et al. [257], and the general procedure is described below. A total of 6 bright radio sources are detected in the *Bolocam* 140 GHz maps for the entire cluster sample. These maps are used to constrain the normalization of a point-source template, centered on the coordinates of the detected radio source in the 1.4 GHz NVSS radio survey [58], and the best-fit template is subsequently subtracted from the data. In addition to this, NVSS-detected sources near the centers of 11 clusters in the BOXSZ sample have extrapolated 140 GHz flux densities greater than 0.5 mJy. This is the threshold found to produce more than a 1% bias in the SZE signal of the cluster, and an effort is made to remove them from the cluster signal. All of the undetected sources are subtracted using the extrapolated flux densities based on a combination of 1.4 GHz NVSS and 30 GHz OVRO/BIMA/SZA measurements.

Furthermore, the uncertainties of these subtracted point sources are accounted for in the estimated error of the Y_{SZ} parameters. This is performed by adding to each noise realization

introduced in Section 3.4 the corresponding point-source template, multiplied by a random value drawn from a Gaussian distribution. The standard deviation of the distribution is equal to either the uncertainty on the normalization of the detected sources, or is based on a fixed 30% uncertainty on the extrapolated flux density for the undetected radio sources.

3.5 Model Fitting

As described in Section 3.3.5, an unbiased image of a given cluster is obtained by deconvolving the signal transfer function from the processed image. However, one subtlety in this process is the fact that the DC component of the signal transfer function is equal to zero, which means that the *Bolocam* data do not constrain the overall signal offset in the deconvolved images. A parametric model is therefore used to constrain this signal offset. Specifically, a signal offset is added to the deconvolved image, so that the average signal in the deconvolved image at $r \geq r_{500}/2$ is equal to the average signal from the parametric model in the same region. Although we have strived to make our SZE measurements as model-indepedent as possible, constraining the overall signal offset of the deconvolved images does introduce some model-dependence in the results (the computation of the signal transfer function introduces an even smaller amount of model dependence, and this is described in Section 3.3.5).

Unprojected SZE signal can be modeled using the pressure profile models, which were generally introduced in Section 2.2.1. Arnaud et al. [15, hereafter A10] measured a GNFW model, which is commonly used in the field and is therefore it is also adopted for this analysis. The A10 model is constrained with X-ray data below R_{500} and with simulations above:

$$p(r) = \frac{p_0}{(cr)^{\gamma} \left[1 + (cr)^{\alpha}\right]^{(\beta-\gamma)/\alpha}}, \tag{3.4}$$

where p_0 is the pressure normalization, c is the concentration parameter that sets the radial scale, and α, β, and γ are the power-law slopes at moderate, large, and small radii. In all cases, the exponential parameters are set to the A10 values: $[\alpha, \beta, \gamma] = [1.05, 5.49, 0.31]$. We allow p_0 to float in all cases and further generalize the fits to allow for ellipticity by substituting r with $\sqrt{r_1^2 + r_2^2/(1-\epsilon)^2}$, where ϵ is the ellipticity and r_1 and r_2 represent

the major and minor axes, respectively. The elliptical generalization of equation 3.4 is numerically integrated using equations 2.11 and 2.12, with the additional assumption that the axis along the line of sight follows the relation:

$$r_3 \equiv \sqrt{\frac{r_1^2}{2} + \frac{r_2^2}{2(1-\epsilon)^2}}. \tag{3.5}$$

Due to the variety of cluster morphologies and SZE signal-to-noise levels within the BOXSZ sample, the number of free parameters needed to sufficiently describe the data varies across the sample. All clusters are therefore fit to a set of four models, each with a different number of free parameters, depending on whether c and/or ϵ are fixed in Equation 3.4 to the A10 values of $c_{A10} = 1.18/r_{500}$ and $\epsilon_{A10} = 0$. These various models are subsequently referred to in terms of the number of their free parameters, (1, 2, 3 or 4), with: (1) c and ϵ are fixed, (2) ϵ is fixed, (3) c is fixed, and (4) both c and ϵ are allowed to float. Note that floating the ellipticity of the 3- and 4-models introduces two additional free parameters: ellipticity as well as the angle of inclination of the major axis.

All cluster fitting is performed by convolving the proposed cluster model with the signal transfer function and minimizing the χ^2 with respect to the processed data:

$$\chi^2 = \sum_i \frac{(model(i) - data(i))^2}{\sigma_i^2}, \tag{3.6}$$

where index i is summed over all map pixels and σ_i is the pixel variance determined from the noise realizations.

3.5.1 Choosing a Minimal Model: The Simulated F-Test

In a general sense, the F-test is the standard statistic to test for the validity of adding an additional parameter to a fit. This statistic calculates the difference between the chi-square distributions for fits to models differing by one degree of freedom, normalized by the reduced χ^2 of the original model, and is given by Bevington & Robinson [30]:

$$F_\chi = \frac{\chi^2(m) - \chi^2(m+1)}{\chi^2(m+1)/(N-m-1)} = \frac{\Delta\chi^2}{\chi_\nu^2}, \tag{3.7}$$

where the values of χ^2 are computed from Equation 3.6 for both the model with $m + 1$ degrees of freedom (the candidate model with one additional free parameter) and the model with m degrees of freedom (the original model).

The model fits to the maps assume a diagonal covariance matrix—implying that pixel-to-pixel noise is uncorrelated. From Sayers et al. [255], we know that this is a good, but not perfect, description of the data. While the assumption of a diagonal covariance matrix is sufficient for model-fitting, the F-test is more sensitive to small-levels of covariance. This covariance is accounted for by utilizing the 1000 noise realizations for each cluster to develop the probability distribution, $\chi^2(m)$, for various degrees of freedom. First, the *observed* χ^2_{Bq} distributions are calculated by fitting the *Bolocam* data, B, with each of the the four different best-fit models, q, for each cluster. Here, $q \in [1, 2, 3, 4]$ represents the number of free parameters of the model fit, which was introduced in Section 3.5. Similarly, the *modeled* χ^2_{pq} distributions are calculated by adding a representative input model, p, to each of the 1000 noise realizations and fitting each one of these model+noise realizations with the q model. Note that each χ^2_{Bq} represents a single data point, while each χ^2_{pq} represents an entire *modeled* χ^2 distribution. For example, χ^2_{13} represents the 1000-element χ^2 distribution for an input 1-model+noise realization fit with a 3-model. In contrast, χ^2_{B3} represents the observed *Bolocam* data fit with a 3-model.

With this information, the modeled F-test is performed by comparing the different χ^2_{Bq} values for two different q values with the difference of the χ^2_{pq} distributions of these same q values. The lower plot of figure 3.12 depicts the differenced $\chi^2_{11} - \chi^2_{12}$ and $\chi^2_{11} - \chi^2_{13}$ distributions for Abell 1423, and the corresponding $\chi^2_{B1} - \chi^2_{B2}$ and $\chi^2_{B1} - \chi^2_{B3}$ values are represented by vertical lines. Since the additional free parameter represented by the scale radius, i.e., c, is not completely described by the two additional free parameters in the ellipticity, i.e. ϵ, the 2-model and the 3-model represent two independent branches of comparison for the F-test. A hierarchical decision tree is therefore implemented to choose the minimal model for each particular cluster. Starting with the 1-model and progressing towards the 4-model:

a. First, the model distribution, $\chi_{12} - \chi_{11}$, is calculated. If $\chi_{B2} - \chi_{B1}$ is greater than 98% of the model distribution, the 1-model is ruled out, and the process proceeds to step b. Otherwise, the 1-model is determined to be a sufficient model for this branch, and the

process continues with step c.

b. The $\chi_{B2} - \chi_{B4}$ value is compared with the $\chi_{22} - \chi_{24}$ distribution. If $\chi_{B2} - \chi_{B4}$ is greater than 98% of the differenced model distribution, the 4-model is chosen as the minimal model, and the F-test procedure is finished. Otherwise, the 2-model is determined to be a sufficient model that describes the data along this branch, and the process proceeds to step c. We chose 98% as the cut-off value based on the expectation that one of the 45 BOXSZ clusters would fall outside of this range.

c. This is the second branch of the F-test, this time replacing the 2-model of steps a-b with the 3-model. Again, if the 4-model is chosen along this branch, it represents the minimal model, and the process is finished.

d. If both branches choose the 1-model, then the 1-model is chosen.

e. If only one branch chooses a 2- or a 3-model, then the higher order model is chosen.

f. If both branches choose either the 3-model or the 2-model, the 2-model is chosen, since it has fewer free parameters.

Once a minimal model is selected for a given cluster, this model is used for all subsequent analysis. The F-test chosen models are given in the last column of table 3.2. The largest fraction of the BOXSZ cluster sample are best described using a 1-model, and this ends up being 16 clusters. The higher-order 2-, 3-, and 4-models are selected for 10, 12, and 7 clusters in the sample, respectively. In a later section, the effect that these different model fits have on the observed scaling relations is explored.

The minimum model required to adequately describe each cluster is then used to determine the signal offset in the deconvolved images. In order to aid the visualization, a schematic of this process is given in figure 3.13. In each case, the noise-weighted mean signal in the deconvolved image is computed in the region $r \geq r_{500}/2$. The mean signal for the minimum model required to describe the cluster is then computed in the same region using the same weighting, and the offset between the two mean signal values is then added to the deconvolved image. A range of radii were explored as possible cutoffs for the region used
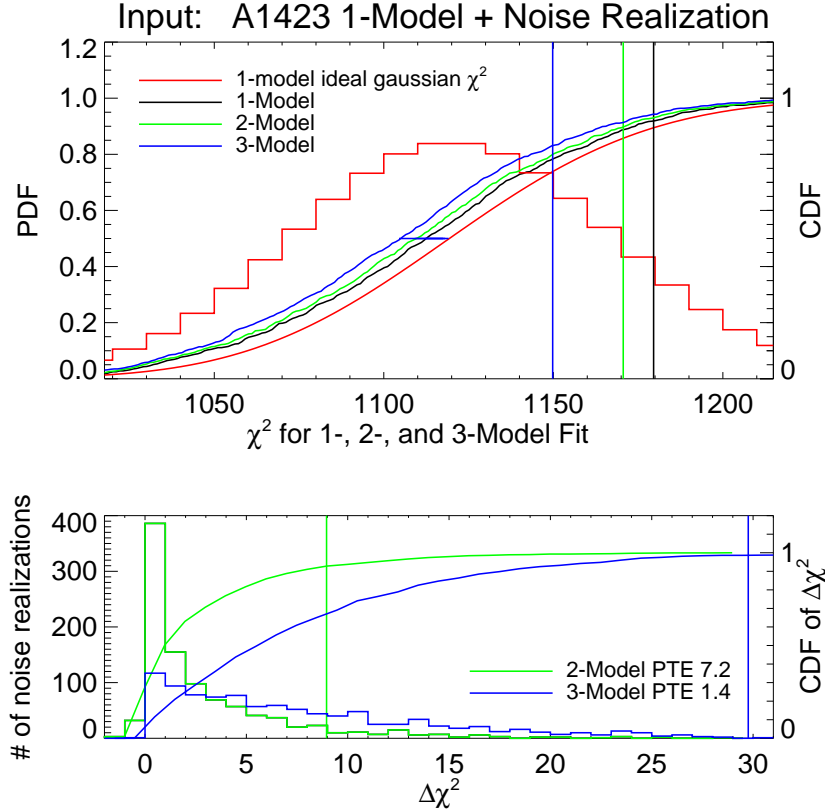
Figure 3.12 Example of the χ^2_{1q} distribution for Abell 1423 used for the modeled F-test. Upper: The red curves represent the 1-model χ^2 PDF and CDF, under the assumption that a diagonal noise covariance matrix fully describes the noise in the processed image. The black line shows the 1-model χ^2 CDF obtained from fits to the 1000 noise realizations. The offset between the black and red CDFs is because a diagonal noise covariance matrix does not perfectly describe the noise, and it motivates the use of empirically-derived CDFs based on the noise realizations. Green lines represent the 2-model, and blue lines the 3-model CDFs. The coloring for the vertical lines represents the observed χ^2_{Bq} values, with the same coloring of model fit as with the modeled χ^2 distributions. Lower: Histograms and CDFs of the $\Delta\chi^2$ for the 2- and 3-model fits to the noise realizations. The PTE of the 3-model fit to the data is less than 2%, and therefore the modeled F-test developed in this work indicates that the 3-model is the best model that describes the data in the first step of the process. The next step in the modeled F-test for this cluster would then be a comparison between the 3- and 4-models.

14' x 14' processed image

10' x 10' deconvolved image

region en-
closed by
r_{2500}

region out-
side r_{500}/2
used to
find signal
offset

signal offset
added to de-
convolved
image
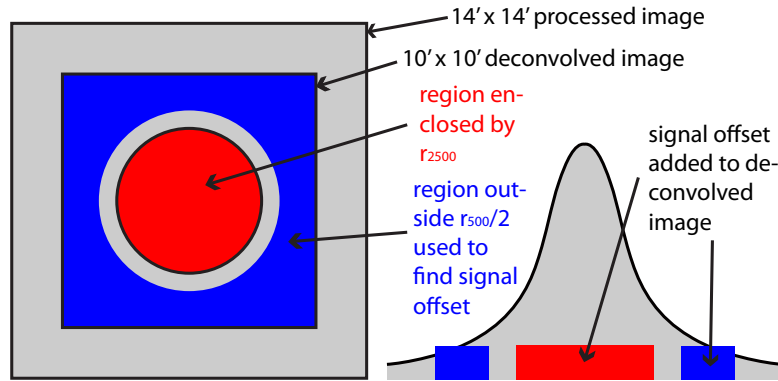
Figure 3.13 Schematic demonstrating how the signal offset for the SZE images is determined. The large gray box on the left demonstrates the extent of a processed image (14×14 arcmin). Prior to deconvolving the signal transfer function, the processed image is trimmed to 10×10 arcmin. The transfer function of the DC signal component is 0, and therefore the overall signal offset of the deconvolved images is unconstrained by the data alone. Consequently, the signal offset is determined by forcing the noise-weighted mean signal in the deconvolved image outside of $R_{500}/2$ to be equal to the mean signal from the minimal parametric model fit to the cluster, using the same weighting in the same region (denoted in blue on the left-hand figure). The region used to compute Y_{2500} is denoted in red, and does not overlap with the region used to constrain the signal offset. The right-hand figure shows a 14 arcmin one-dimensional slice through a cartoon cluster, showing that the cluster SZE signal is non-zero even at the edge of the image. The blue and red boxes indicate the approximate value of the signal offset added to the deconvolved image.

in the computation of the mean signal. This radius should be large enough so that the region of the image used to compute the model offset is independent from the region used to determine Y_{SZ}, thus minimizing the model-dependence of the Y_{SZ} estimates. However, at larger radii the measurement noise on the mean signal increases quickly because the number of map pixels included in the calculation drops. At $R_{500}/2$ the mean-signal measurement noise is near its minimum, yet this radius is in general outside of the integration radius used to compute Y_{SZ}, R_{2500}. For the BOXSZ sample, $R_{500}/2$ varies from $\simeq 1-4$ arcminutes, with a median of approximately 2.5 arcminutes.

The same process is then applied to each of the 1000 noise realizations for each cluster, with the signal offset determined using the minimum-model fits to the model+noise realizations described above. Therefore, the uncertainty in the signal offset is fully included in the ensemble of noise realizations. Figures 3.14 and 3.15 show thumbnails of the SZE filtered and deconvolved maps for the entire data set, respectively. For the deconvolved maps, the F-test determined offsets are included. The best-fit pressure profile parameters for the BOXSZ sample are presented in Table 3.2.

3.5.2   Measured Ellipticity

Beyond being a mass proxy, several groups are interested in using SZE data to constrain cluster triaxiality. To the extent that there is no selection bias in the line-of-sight extent of galaxy clusters, the distribution of ellipticity can characterize the distribution of triaxial structure in general (LaRoque et al. [151]). Furthermore, ellipticity is a strong indicator of an abnormal cluster morphology.

Figure 3.16 depicts the measured BOXSZ ellipticity, given an assumed model and the F-test results. 19 out of the 45 clusters (42%) prefer a free elliptical measurement parameter. As expected, the signal-to-noise ratios of the measured ellipticities of the F-test sample are significant with a median S/N $\gtrsim 4.0$. While it cannot be assumed that the source of the ellipticities are actual cluster SZE signal, many of the clusters with the most extreme ellipticity measurements show signs of being exceptional.

The most extreme major-to-minor axis ratio measured for the BOXSZ sample is 4.8 ± 0.6, for the cluster MACSJ 0911.2. While this cluster is not characterized as disturbed in [256],
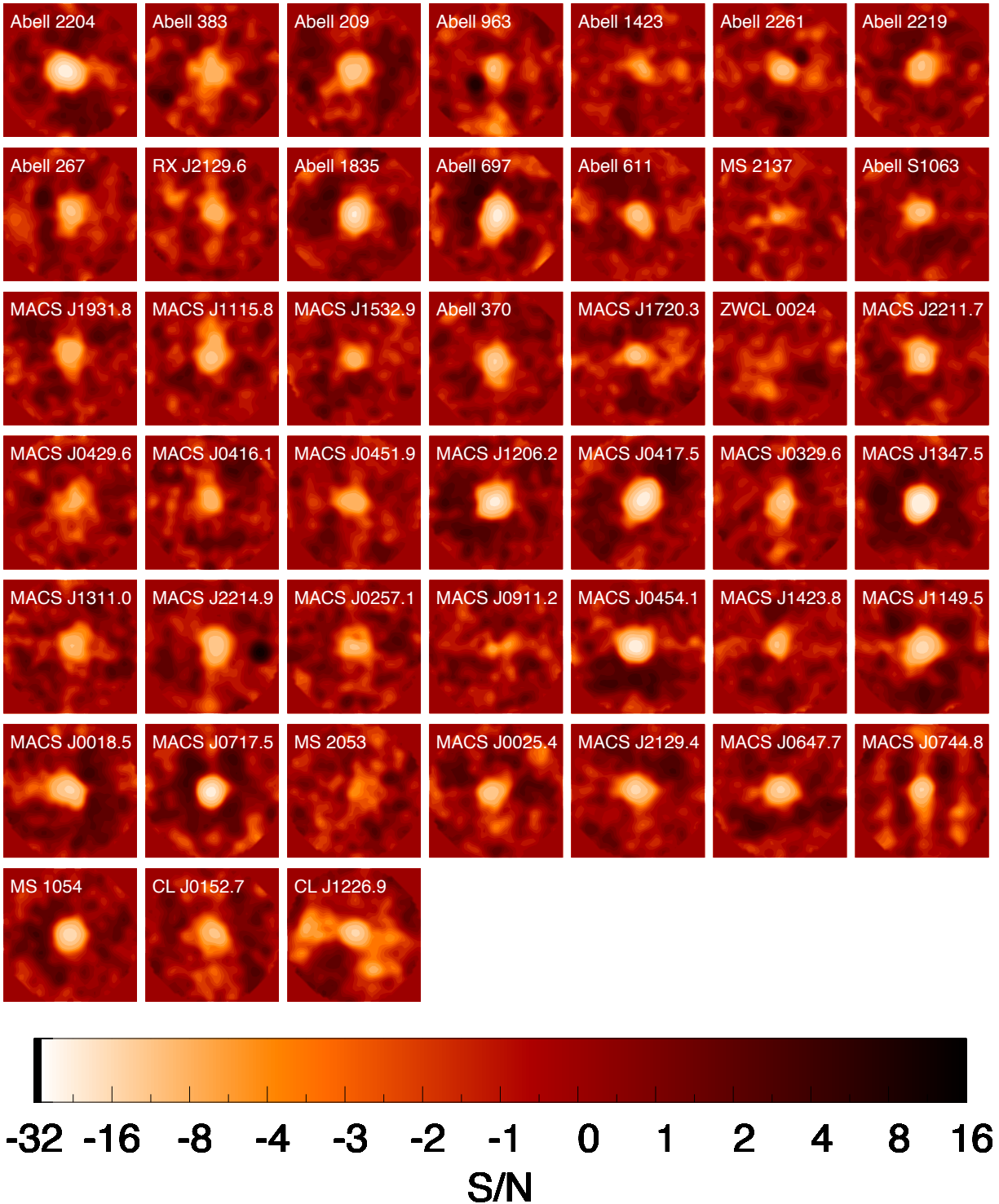
Figure 3.14 Thumbnails showing the S/N per beam in the processed SZE images for all 45 BOXSZ clusters. The images are 14×14 arcminutes in size. The color scale is linear from S/N of -4 to S/N of $+2$ to allow an accurate visualization of the noise and low S/N SZE decrements, and the color scale is quasi-logarithmic at lower and higher S/N values. This logarithmic scale is required due to the large dynamic range of some images, due to significant SZE decrements and/or bright point sources. Note that the point sources are subtracted from the data prior to any estimation of Y_{2500}.
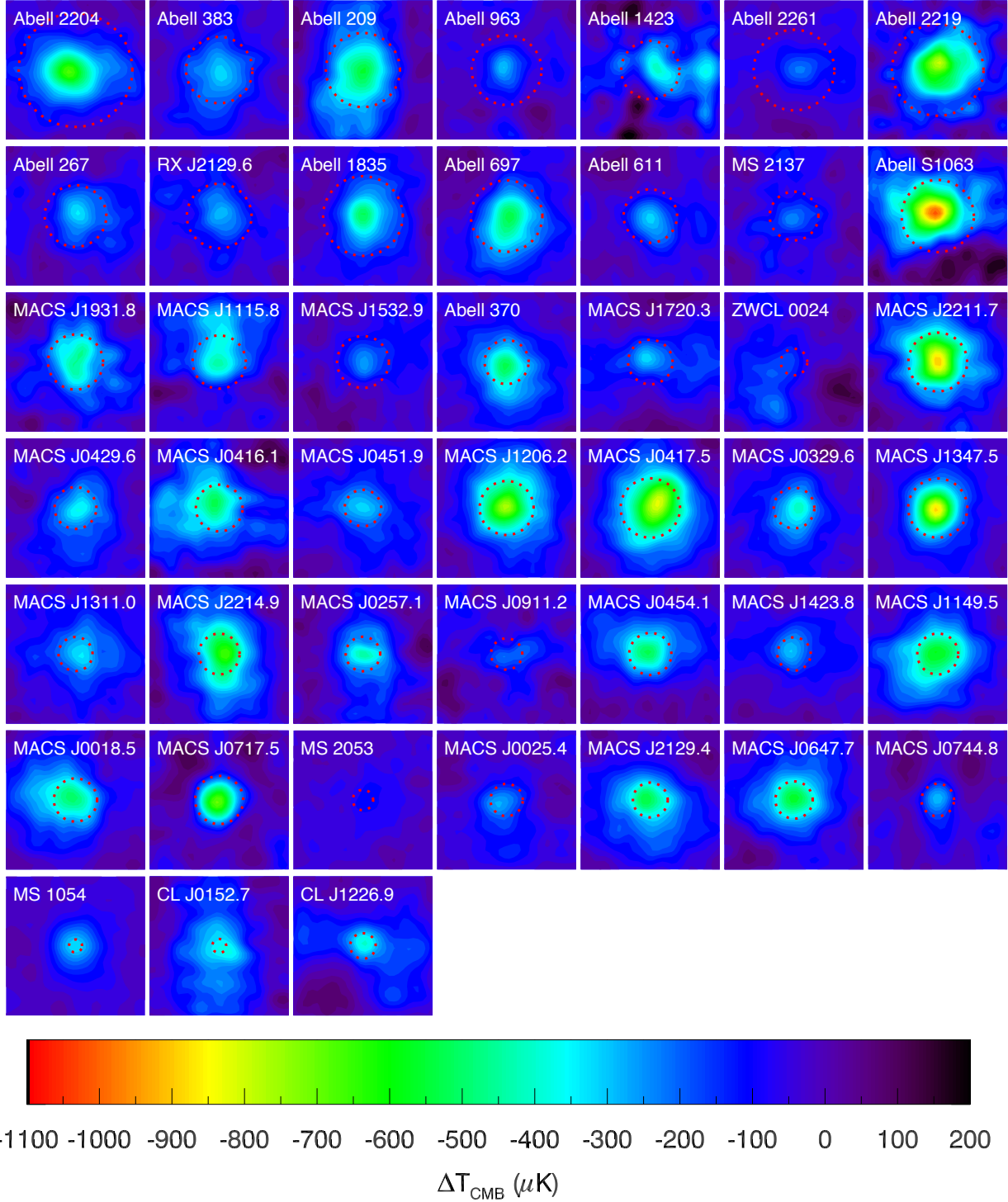
Figure 3.15 Thumbnails showing the deconvolved SZE images of all 45 BOXSZ clusters. Each image is 10×10 arcminutes in size. These images have been directly integrated to obtain Y_{2500}, with the region enclosed by R_{2500} shown as a dashed red line.
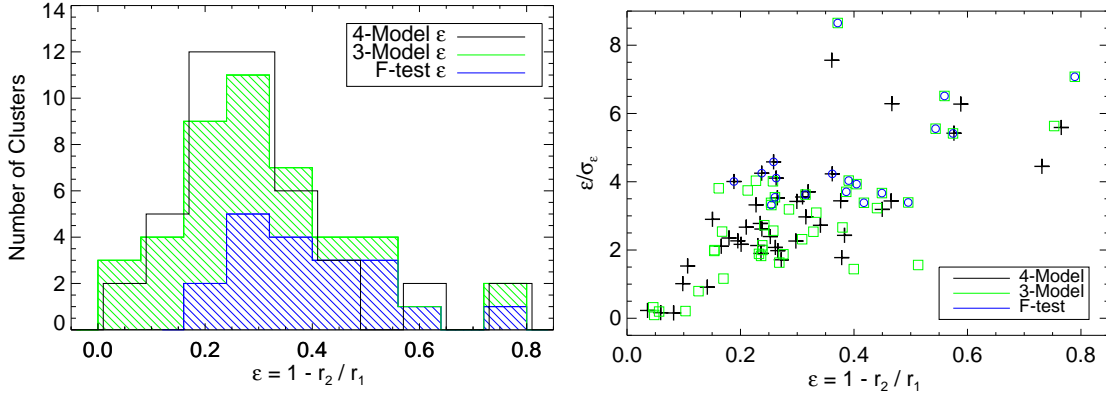
Figure 3.16 The distribution of ellipticities for the BOXSZ cluster sample. Left: distribution of the measured 4-model (black), 3-model (green), and F-test (blue) ellipticities in the BOXSZ sample. The bins of the 4-model distribution are shifted slightly for clarity. Right: average signal-to-noise ratio of the measured ellipticities in the BOXSZ sample for fits to the 4-model (black crosses), 3-model (green squares), and F-test-selected models(blue circles).

it is one of the more interesting clusters in the Kartaltepe et al. [137] study of the MACS high-redshift sample. Kartaltepe et al. [137] identify two sub-clusters for MACSJ 0911.2 approximately 1 Mpc apart, and the *Bolocam*-measured major-axis orientation of 83.2 ± 7.3 degrees West-of-North is similar to the axis between the two sub-clusters which Kartaltepe et al. [137] do not explicitly measure.

The next most elliptical cluster is MACSJ 0744.8 with a measured major-to-minor ratio of 2.3 ± 0.4. This cluster is classified as disturbed in Sayers et al. [257], and there are no known point sources immediately in its vicinity. Korngut et al. [143] have identified a shock in the high-resolution MUSTANG SZE maps of this cluster and measure a Mach number of 1.2 ± 0.2, resulting from two clusters colliding with a relative speed of 1827^{+267}_{-195}km/s. The *Bolocam*-measured North-South elongation is similar in orientation to the one measured in Korngut et al. [143], although this correlation must be taken with caution, considering that MUSTANG and *Bolocam* measure the SZE at extremely different scales. Kartaltepe et al. [137] note a complex red-sequence galaxy surface density morphology exhibiting an elongated double peak. This galaxy cluster has also been studied using strong lensing [303, 258]. Of all the MACS high-redshift galaxy clusters studied in those works, MACSJ 0744.8 has the least extension along the line-of-sight. One can visually identify that the major axes of the mass and galaxy surface densities are orthogonal to both sets of SZE data. If the cluster is

indeed post-merger, this would perhaps suggest that the *Bolocam* SZE signal is along the major axis of the shock, as expected. However, considering that the X-ray surface brightness does not exhibit any similar ellipticity to the SZE signal, this suggests the need for further investigation of what could be the source of ellipticity.

As the most distant cluster in the BOXSZ sample (and also one of the hottest), it is no surprise that CLJ 1226.9 stands out, with the third-highest measured ellipticity of 2.2 ± 0.4. Jee et al. [127] cite this cluster to exhibit tension with the standard ΛCDM cosmological model, due to being so massive and at such a high redshift. Nevertheless, the cluster is not classified as disturbed based on the X-ray centroid shift parameter [177, 256]. A 0.08 mJy point source has been identified in the *Bolocam* data [257], although it is not removed, because it is not expected to affect the integrated Y_{SZ} signal. CLJ 1226.0 is also studied in Korngut et al. [143], where they note an SZE enhancement in the South-West region of the cluster. This is in agreement with an X-ray-hot region and a lensing-identified sub cluster $40''$in the South-West region of the X-ray centroid [176, 126]. In contrast to the case of MACSJ 0744.8, the *Bolocam* Y_{SZ} elongation is along the lensing mass major axis. This would suggest that the merger is not causing a noticeable distortion of the large-scale Y_{SZ} signal.

3.6 Choice of Integration Aperture

Scaling relations at different radii are not necessarily the same because halo concentration is correlated tightly with formation epoch and is therefore dependent on the underlying cosmology (Bond et al. 38, Bryan & Norman 44, Lemson & Kauffmann 157, Wechsler et al. 284, 285, Wetzel et al. 287, Jing et al. 131, Wu et al. 297). The choice of R_{500} as an integration aperture is popular because simulations indicate that this is the point at which a given mass proxy is least affected by the non-thermal activity of the cluster core and the observed clumping in the cluster outskirts (Evrard et al. [84]). Unfortunately, it is often difficult to obtain reliable X-ray measurements out to this radius using XMM-*Newton* and *Chandra* observations due to significant foreground dominating the dim cluster emission. Consequently, many analyses involving X-ray data have chosen to instead use R_{2500} (e.g.,

Bonamente et al. 37).

For this analysis, $\Delta = 2500$ is chosen primarily due to systematic uncertainties related to the SZE data. In particular, the fractional noise on Y_{SZ} due to uncertainties in the signal offset of the deconvolved images grows quickly with integration radius, increasing by approximately a factor of two between R_{2500} and R_{500} as depicted in Figure 3.17. Furthermore, a few clusters in the BOXSZ sample have values of R_{500} larger than the $10' \times 10'$ deconvolved images. Although the choice of integration radius is not driven by considerations related to the X-ray analysis, it should be noted that due to the rapid roll-off of X-ray surface brightness beyond R_{2500}, the noise in the *Chandra* X-ray measurements is lower at R_{2500} as well.

One consequence of this choice of integration radius is that it is not significantly larger than the *Bolocam* PSF, and therefore beam-smoothing effects can bias the Y_{2500} estimate. Effectively, this implies that some of the SZE emission within R_{2500} appears in the *Bolocam* image outside of R_{2500}, due to beam smearing. To estimate this bias, Y_{2500} is computed using the minimal parametric model, determined in Section 3.5.1, both before and after convolution with the *Bolocam* PSF. The *Bolocam*-measured Y_{2500} value is then corrected by the ratio of Y_{2500} values, determined from the un-smoothed and beam-smoothed model for each cluster. This beam-smoothing correction is generally $\lesssim 10\%$, and anti-correlated with mass due to the fact that more massive clusters tend to have larger R_{2500} (see Figure 3.17). Therefore, although this beam-smoothing bias is relatively minor, it is critical to correct for this bias in order to obtain an accurate scaling relation due to its mass dependence.

The fractional bias due to beam smoothing is plotted in Figure 3.17 together with rms large-scale signal modeling uncertainty. The figure demonstrates how the beam-smoothing bias and the rms uncertainty in the signal offset is minimized at integration radius of $\sim 1.3'$. This is very close to the median of the R_{2500} distribution but at the edge of the R_{500} distribution. The rms signal offset uncertainty is approximately 20% around the median of R_{500} and is significantly larger than the simulated intrinsic scatter between Y_{SZ} as a function of M_{tot}, such as is modeled in Nagai et al. [198]. For this reason, we have chosen R_{2500} as the integration radius for the BOXSZ scaling relation analysis.
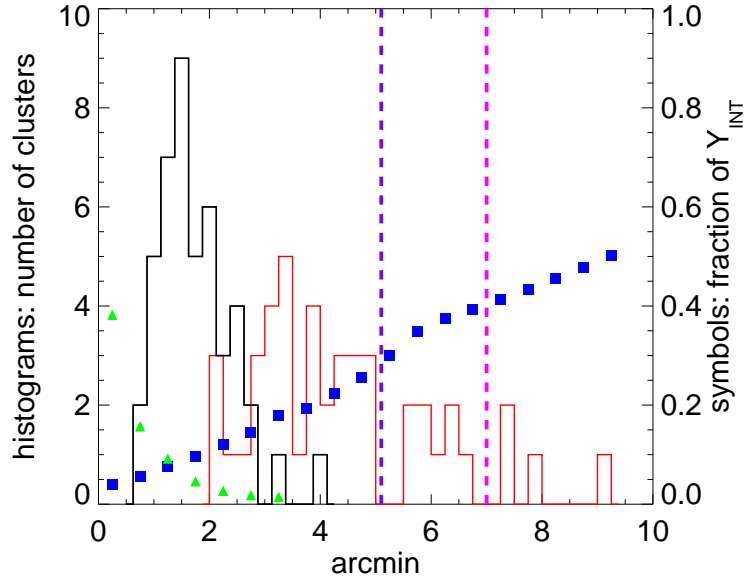
Figure 3.17 Histograms, left axis: Distribution of the R_{500}(red) and R_{2500}(black) values for the BOXSZ cluster sample. (Magenta, dashed) 7 arcmin ensquared radial extent of the BOXSZ maps, and (violet, dashed) 5 arcmin ensquared radial extent of the deconvolved BOXSZ maps. Symbols, right axis: (green, triangles) The radial dependence of the systematic bias in Y_Δ due to the finite size of the *Bolocam* PSF. (Blue, squares) uncertainty in Y_Δ as a function of integration radius due to uncertainties solely in the signal offset of the deconvolved SZE image. As a point of reference, recall that there is an overall 5% flux calibration uncertainty for the BOXSZ cluster sample.

3.7 Y_{SZ} Estimation

The signal-offset-corrected deconvolved SZE images are directly integrated using Equation 2.12 to determine the best-fit value of Y_{SZ} for each cluster, with the integration extended over the solid angle within R_{2500}. In addition, the value of Y_{SZ} is also computed for each of the 1000 noise realizations, and these values are then added to the best-fit value of Y_{SZ} to produce a distribution of Y_{SZ} values based on the noise properties of each cluster. Figure 3.18 and Equation 3.1 demonstrate that an uncertainty in M_{tot} directly translates into an uncertainty in the X-ray estimated r_{Δ}. To account for the uncertainty in Y_{SZ} due to uncertainties in the X-ray derived value of R_{2500}, the integration radius for each noise realization is randomly drawn from the distribution of R_{2500} values produced by the Monte-Carlo chains obtained from the X-ray data discussed in Section 3.2. In contrast to the distribution of M_{tot} values, which is log-Gaussian, the distribution of Y_{SZ} values is approximately Gaussian. The final Y_{SZ} values are presented in Table 3.3, and the M_{tot} and Y_{2500} distributions are depicted in Figure 3.19. Since the scaling relation formalism in Section 4.1 assumes log-Gaussian error, the effects of the Gaussian distribution of Y_{SZ} values are accounted for via simulation, which is described in detail in Section 4.3. Note that all of the errors shown in any figures or given in any tables throughout this manuscript are equal to the standard deviations of the Y_{SZ} distributions for each cluster. The employed method to compute Y_{SZ} differs from the parametric fitting methods used in other scaling relation analyses (e.g., Bonamente et al. 37, Marrone et al. 171, Planck Collaboration et al. 224, 229, Andersson et al. 8, Marrone et al. 172), as the directly detected signal is not parameterized. Parametric models are solely used to determine the signal transfer function (which very weakly depends on cluster shape), and to constrain the average signal in the deconvolved images in a region *outside* the integration radius for Y_{SZ}.
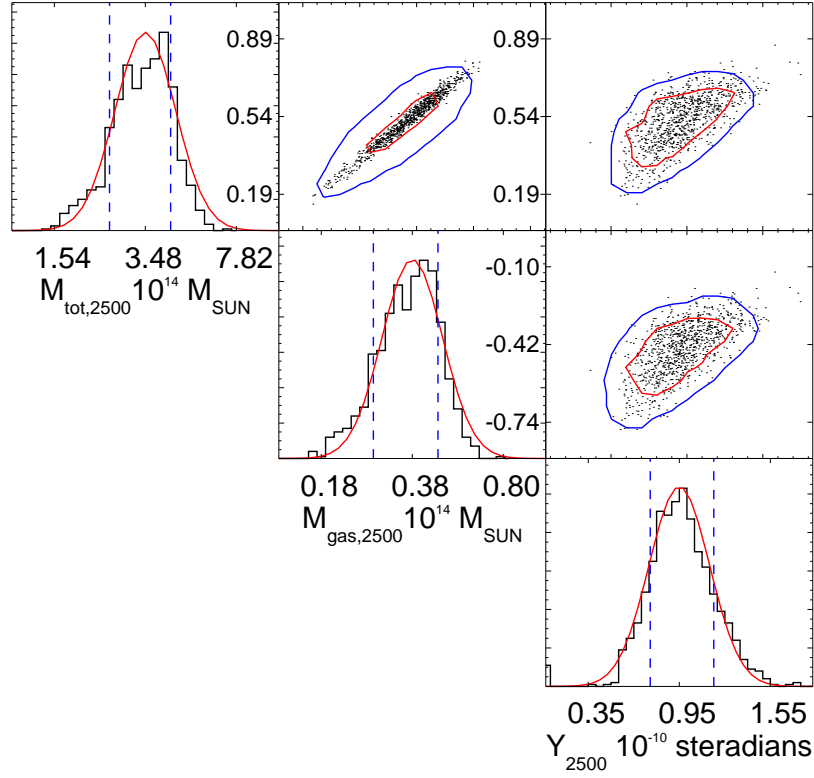
Figure 3.18 Two-dimensional confidence intervals (68% outlined in red and 95% outlined in blue), along with the one-dimensional marginalized PDFs for R_{2500}, M_{2500}, and Y_{2500} for the cluster MACSJ 0416.1, a typical *Bolocam* cluster with z=0.42 and $M_{500} = 0.9 \times 10^{15}$. The red-line is a best-fit normal distribution drawn to help guide the eye. The mass values are given on a logarithmic axis and Y_{SZ} values are given on a linear axis. Note that the uncertainty in $M_{tot,2500}$, as discussed in Section 3.2, derives from the uncertainty in $f_{gas,2500}$, while the uncertainty in $M_{gas,2500}$ derives from the uncertainty in R_{2500}, which is a function of $M_{tot,2500}$.

Table 3.2: Best-Fit Cluster Pressure Profile Parameters for the BOXSZ cluster sample.

Catalog	ID	ΔRA (arcmin)	ΔDEC (arcmin)	p_0 ($10^{-11}\frac{\text{erg}}{\text{cm}^3}$)	r_s (arcmin)	ϵ	θ (°E of N)	χ^2	DOF	F
Abell	2204	0.42±0.05	-0.15±0.07	23.7± 3.7	4.3±0.4	0.26±0.06	82.6± 7.2	1197.4	1117.0	4
Abell	383	-0.03±0.05	-0.25±0.17	4.5± 0.6	11.6±3.1	···	···	1156.2	1118.0	2
Abell	209	0.11±0.04	-0.16±0.09	9.2± 0.8	6.3	0.25±0.08	-18.4± 8.8	1206.8	1118.0	3
Abell	963	0.17±0.06	0.13±0.11	41.8±22.7	1.6±0.9	···	···	1179.9	1118.0	2
Abell	1423	-0.34±0.06	0.27±0.34	7.2± 1.4	5.5	0.50±0.15	69.8±11.2	1149.8	1118.0	3
Abell	2261	-0.46±0.05	0.00±0.23	3.7± 0.7	6.3	0.42±0.12	82.6± 8.8	1111.8	1116.0	3
Abell	2219	-0.16±0.08	0.28±0.14	13.4± 1.7	6.7	···	···	1084.3	1120.0	1
Abell	267	-0.27±0.04	0.22±0.15	7.9± 1.3	4.7	···	···	1011.6	1119.0	1
RX	J2129.6+0005	-0.25±0.06	0.27±0.14	6.4± 1.0	4.8	0.45±0.12	17.6±10.0	1182.8	1118.0	3
Abell	1835	-0.13±0.06	0.02±0.07	9.3± 1.1	5.4	0.26±0.07	-15.6±10.0	967.1	946.0	3
Abell	697	-0.11±0.03	-0.23±0.05	9.1± 0.6	5.5	0.37±0.04	-21.2± 4.0	1284.2	1118.0	3
Abell	611	-0.02±0.04	-0.28±0.15	8.4± 1.1	4.0	···	···	1120.5	1120.0	1
MACS	J2140.2-2339	0.01±0.06	-0.20±0.24	5.5± 1.1	3.3	···	···	1124.8	1120.0	1
Abell	S1063	0.35±0.10	0.21±0.13	15.6± 1.8	5.0	···	···	1113.5	1120.0	1
MACS	J1931.8-2634	-0.06±0.04	0.31±0.12	9.9± 1.2	3.8	···	···	1180.4	1120.0	1
MACS	J1115.8+0129	-0.04±0.06	0.60±0.13	4.5± 0.8	6.6±1.6	0.30±0.09	-0.0± 9.8	1179.2	1117.0	4
MACS	J1532.8+3021	0.06±0.04	0.03±0.15	6.3± 1.1	3.7	···	···	1204.2	1120.0	1
Abell	370	0.04±0.04	-0.37±0.10	10.0± 1.1	3.8	···	···	1143.2	1120.0	1
MACS	J1720.2+3536	-0.12±0.05	0.18±0.24	1.9± 0.4	21.4±5.8	0.47±0.07	-82.1	1210.7	1117.0	4
Cl	0024+17	1.00±0.05	-0.39±0.37	4.4± 1.8	2.7	···	···	1201.4	1120.0	1
MACS	J2211.7-0349	0.05±0.07	0.15±0.09	16.2± 1.8	4.2	···	···	1153.0	1120.0	1
MACS	J0429.6-0253	-0.31±0.06	-0.03±0.18	3.3± 0.7	9.7±2.9	···	···	1168.4	1119.0	2
MACS	J0416.1-2403	0.26±0.08	0.31±0.14	9.6± 1.3	3.2	···	···	996.5	948.0	1
MACS	J0451.9+0006	0.02±0.04	0.06±0.13	7.7± 1.1	2.8	···	···	1164.6	1120.0	1
MACS	J1206.2-0847	0.14±0.05	0.10±0.06	12.6± 0.9	4.0	···	···	1102.7	1120.0	1
MACS	J0417.5-1154	-0.50±0.05	0.31±0.06	8.3± 0.9	6.7±0.9	···	···	1165.8	1119.0	2
MACS	J0329.6-0211	-0.25±0.05	-0.02±0.09	11.0± 1.3	2.9	0.40±0.10	-5.0± 9.3	1212.5	1118.0	3
MACS	J1347.5-1144	0.15±0.03	-0.11±0.03	36.3± 5.4	2.4±0.2	0.19±0.05	-20.4± 9.0	1073.2	1117.0	4
MACS	J1311.0-0310	-0.45±0.04	0.11±0.15	2.9± 0.7	5.7±1.7	···	···	1118.5	1119.0	2
MACS	J2214.9-1359	-0.36±0.06	0.07±0.10	12.9± 1.5	3.2	0.39±0.10	14.2± 9.0	1131.5	1115.0	3
MACS	J0257.1-2325	-0.14±0.05	0.03±0.15	3.3± 0.4	14.4±3.8	···	···	1062.9	1119.0	2
MACS	J0911.2+1746	-0.70±0.06	-0.01±0.33	7.1± 1.5	2.8	0.79±0.11	-83.2± 7.6	1127.8	1118.0	3
MACS	J0454.1-0300	0.24±0.03	0.13±0.07	8.0± 1.1	4.2±0.3	0.26±0.06	86.4± 7.2	1188.8	1117.0	4
MACS	J1423.8+2404	0.16±0.04	0.29±0.11	9.5± 1.4	2.4	···	···	1052.6	1120.0	1
MACS	J1149.5+2223	0.01±0.04	-0.16±0.07	5.8± 0.9	5.9±1.4	0.24±0.06	-51.3± 8.6	1119.6	1117.0	4

Catalog	ID	ΔRA (arcmin)	ΔDEC (arcmin)	p_0 $(10^{-11}\frac{\text{erg}}{\text{cm}^3})$	r_s (arcmin)	ϵ	θ (°E of N)	χ^2	DOF	F
MACS	J0018.5+1626	0.31±0.05	0.07±0.10	5.6± 0.8	5.5±1.1	···	···	1098.9	1119.0	2
MACS	J0717.5+3745	0.10±0.10	-0.06±0.04	38.2± 9.9	2.2±0.4	···	···	1188.7	1119.0	2
MS	2053.7-0449	-0.58±0.03	0.10±0.24	5.1± 1.4	1.8	···	···	1205.9	1120.0	1
MACS	J0025.4-1222	0.46±0.04	-0.25±0.09	9.1± 1.0	2.4	···	···	1226.7	1120.0	1
MACS	J2129.4-0741	0.15±0.04	0.12±0.08	13.9± 1.5	2.7	0.31±0.09	65.8± 8.5	1124.5	1118.0	3
MACS	J0647.7+7015	-0.03±0.05	0.03±0.09	7.1± 1.4	4.4±0.8	···	···	1128.9	1119.0	2
MACS	J0744.8+3927	0.01±0.05	0.04±0.06	10.9± 1.0	2.5	0.56±0.09	-2.8± 5.1	1265.2	1118.0	3
MS	1054.4-0321	-0.02±0.04	-0.02±0.09	5.7± 1.4	3.7±0.7	···	···	1086.1	1119.0	2
RXJ	0152.7-1357	-0.08±0.06	0.04±0.12	2.0± 0.4	8.3±2.7	0.36±0.09	8.4± 8.1	1220.3	1117.0	4
CLJ	1226.9+3332	-0.11±0.08	0.21±0.11	17.8± 1.9	1.8	0.54±0.10	71.2± 6.7	1293.2	1118.0	3

Note. — The third and fourth columns give the SZE centroid shift with respect to the X-ray centroid, given in Table 3.1. The fifth, sixth, seventh, and eighth columns give the amplitude, scale radius, ellipticity, and orientation of the major elliptical axis, as defined for Equation 3.4. There exists a degeneracy between the amplitude and scale radius, and the given error bars fully marginalize over this degeneracy. The ninth, tenth and eleventh columns give the best-fit χ^2, the number of degrees of freedom of the GNFW profile fits, and the probability for the measured χ^2 to exceed the number of degrees of freedom. The final column gives the number of free parameters as determined from the F-test.

Table 3.3: Physical X-ray and SZE Parameters Measured in this Analysis.

Catalog	ID	z	r_{2500} (Mpc)	$M_{gas,2500}$ ($10^{14} M_\odot$)	$M_{tot,2500}$ ($10^{14} M_\odot$)	kT (keV)	Y_{2500} (10^{-10} ster)	w_{500} (10^{-2})
Abell	2204	0.151	$0.62^{+0.03}_{-0.03}$	$0.44^{+0.07}_{-0.05}$	$4.00^{+0.68}_{-0.51}$	8.55 ± 0.58	$3.37^{+0.59}_{-0.64}$	0.13 ± 0.04
Abell	383	0.188	$0.44^{+0.02}_{-0.03}$	$0.16^{+0.02}_{-0.02}$	$1.46^{+0.22}_{-0.24}$	5.36 ± 0.19	$1.70^{+0.47}_{-0.40}$	0.19 ± 0.03
Abell	209	0.206	$0.53^{+0.03}_{-0.03}$	$0.29^{+0.04}_{-0.05}$	$2.61^{+0.41}_{-0.47}$	8.23 ± 0.66	$2.34^{+0.37}_{-0.34}$	0.50 ± 0.17
Abell	963	0.206	$0.50^{+0.03}_{-0.02}$	$0.25^{+0.03}_{-0.03}$	$2.22^{+0.39}_{-0.30}$	6.08 ± 0.30	$0.58^{+0.25}_{-0.25}$	0.22 ± 0.11
Abell	1423	0.213	$0.42^{+0.03}_{-0.03}$	$0.14^{+0.03}_{-0.02}$	$1.31^{+0.29}_{-0.22}$	5.75 ± 0.59	$0.81^{+0.33}_{-0.31}$	0.76 ± 0.19
Abell	2261	0.224	$0.60^{+0.03}_{-0.03}$	$0.43^{+0.05}_{-0.06}$	$3.87^{+0.56}_{-0.58}$	6.10 ± 0.32	$1.14^{+0.30}_{-0.27}$	0.85 ± 0.08
Abell	2219	0.228	$0.71^{+0.04}_{-0.03}$	$0.69^{+0.10}_{-0.08}$	$6.29^{+1.08}_{-0.87}$	10.90 ± 0.53	$3.68^{+0.83}_{-0.81}$	0.18 ± 0.13
Abell	267	0.230	$0.48^{+0.02}_{-0.02}$	$0.21^{+0.03}_{-0.02}$	$1.93^{+0.27}_{-0.26}$	7.13 ± 0.71	$0.85^{+0.24}_{-0.20}$	2.68 ± 1.26
RX	J2129.6+0005	0.235	$0.52^{+0.04}_{-0.02}$	$0.27^{+0.04}_{-0.03}$	$2.47^{+0.39}_{-0.33}$	6.34 ± 0.62	$0.84^{+0.22}_{-0.22}$	0.52 ± 0.14
Abell	1835	0.253	$0.65^{+0.03}_{-0.03}$	$0.56^{+0.07}_{-0.05}$	$5.11^{+0.80}_{-0.57}$	9.00 ± 0.25	$1.75^{+0.31}_{-0.29}$	0.23 ± 0.02
Abell	697	0.282	$0.64^{+0.04}_{-0.04}$	$0.54^{+0.09}_{-0.08}$	$4.90^{+0.96}_{-0.89}$	10.93 ± 1.11	$1.87^{+0.28}_{-0.26}$	0.60 ± 0.45
Abell	611	0.288	$0.49^{+0.02}_{-0.02}$	$0.24^{+0.03}_{-0.02}$	$2.21^{+0.35}_{-0.27}$	6.85 ± 0.34	$0.62^{+0.15}_{-0.14}$	0.56 ± 0.10
MACS	J2140.2-2339	0.313	$0.47^{+0.02}_{-0.02}$	$0.22^{+0.02}_{-0.02}$	$1.98^{+0.27}_{-0.23}$	4.67 ± 0.43	$0.39^{+0.11}_{-0.11}$	0.39 ± 0.05
Abell	S1063	0.348	$0.75^{+0.04}_{-0.04}$	$0.94^{+0.15}_{-0.11}$	$8.57^{+1.61}_{-1.28}$	10.90 ± 0.50	$3.29^{+0.63}_{-0.60}$	0.75 ± 0.15
MACS	J1931.8-2634	0.352	$0.57^{+0.02}_{-0.02}$	$0.42^{+0.05}_{-0.04}$	$3.83^{+0.51}_{-0.44}$	7.47 ± 1.40	$1.26^{+0.21}_{-0.20}$	0.35 ± 0.09
MACS	J1115.8+0129	0.355	$0.56^{+0.02}_{-0.02}$	$0.40^{+0.04}_{-0.04}$	$3.65^{+0.44}_{-0.46}$	9.20 ± 0.98	$1.06^{+0.30}_{-0.32}$	0.27 ± 0.05
MACS	J1532.8+3021	0.363	$0.55^{+0.03}_{-0.03}$	$0.38^{+0.05}_{-0.04}$	$3.39^{+0.55}_{-0.39}$	6.83 ± 1.00	$0.44^{+0.15}_{-0.15}$	0.28 ± 0.15
Abell	370	0.375	$0.48^{+0.03}_{-0.03}$	$0.26^{+0.04}_{-0.04}$	$2.35^{+0.41}_{-0.47}$	7.34 ± 0.52	$0.86^{+0.15}_{-0.16}$	4.90 ± 2.00
MACS	J1720.2+3536	0.387	$0.49^{+0.03}_{-0.02}$	$0.28^{+0.04}_{-0.03}$	$2.54^{+0.42}_{-0.33}$	7.90 ± 0.74	$1.14^{+0.62}_{-0.34}$	0.24 ± 0.06
Cl	0024+17	0.395	$0.30^{+0.02}_{-0.02}$	$0.06^{+0.01}_{-0.01}$	$0.55^{+0.13}_{-0.11}$	5.94 ± 0.87	$0.12^{+0.07}_{-0.07}$	2.53 ± 0.41
MACS	J2211.7-0349	0.396	$0.66^{+0.03}_{-0.03}$	$0.69^{+0.10}_{-0.08}$	$6.30^{+1.01}_{-0.84}$	13.97 ± 2.74	$2.35^{+0.33}_{-0.33}$	0.88 ± 0.13
MACS	J0429.6-0253	0.399	$0.47^{+0.02}_{-0.02}$	$0.25^{+0.03}_{-0.03}$	$2.25^{+0.35}_{-0.30}$	8.33 ± 1.58	$0.78^{+0.24}_{-0.20}$	0.39 ± 0.07
MACS	J0416.1-2403	0.420	$0.54^{+0.05}_{-0.05}$	$0.38^{+0.10}_{-0.10}$	$3.40^{+0.95}_{-0.88}$	8.21 ± 0.99	$1.00^{+0.24}_{-0.20}$	2.02 ± 1.06
MACS	J0451.9+0006	0.430	$0.43^{+0.04}_{-0.03}$	$0.19^{+0.05}_{-0.04}$	$1.77^{+0.53}_{-0.37}$	6.70 ± 0.99	$0.42^{+0.10}_{-0.09}$	1.93 ± 0.80
MACS	J1206.2-0847	0.439	$0.64^{+0.03}_{-0.03}$	$0.66^{+0.09}_{-0.07}$	$6.00^{+0.98}_{-0.83}$	10.71 ± 1.29	$1.77^{+0.21}_{-0.21}$	0.72 ± 0.11
MACS	J0417.5-1154	0.443	$0.70^{+0.04}_{-0.04}$	$0.88^{+0.13}_{-0.12}$	$7.96^{+1.40}_{-1.28}$	9.49 ± 1.12	$2.63^{+0.43}_{-0.44}$	3.01 ± 0.07
MACS	J0329.6-0211	0.450	$0.49^{+0.02}_{-0.02}$	$0.30^{+0.03}_{-0.03}$	$2.71^{+0.39}_{-0.32}$	6.34 ± 0.31	$0.61^{+0.10}_{-0.09}$	1.40 ± 0.26
MACS	J1347.5-1144	0.451	$0.71^{+0.10}_{-0.03}$	$0.92^{+0.10}_{-0.10}$	$8.37^{+1.12}_{-1.05}$	10.75 ± 0.83	$1.76^{+0.17}_{-0.16}$	0.59 ± 0.04
MACS	J1311.0-0310	0.494	$0.43^{+0.02}_{-0.02}$	$0.21^{+0.02}_{-0.02}$	$1.93^{+0.28}_{-0.22}$	6.00 ± 0.32	$0.46^{+0.09}_{-0.09}$	0.22 ± 0.08
MACS	J2214.9-1359	0.503	$0.52^{+0.03}_{-0.03}$	$0.38^{+0.06}_{-0.05}$	$3.46^{+0.70}_{-0.54}$	9.65 ± 0.78	$1.06^{+0.20}_{-0.20}$	1.30 ± 0.29
MACS	J0257.1-2325	0.505	$0.45^{+0.03}_{-0.02}$	$0.23^{+0.04}_{-0.03}$	$2.10^{+0.40}_{-0.31}$	9.90 ± 0.90	$0.95^{+0.27}_{-0.21}$	0.46 ± 0.13
MACS	J0911.2+1746	0.505	$0.41^{+0.02}_{-0.03}$	$0.17^{+0.03}_{-0.03}$	$1.59^{+0.29}_{-0.31}$	6.60 ± 0.60	$0.19^{+0.09}_{-0.08}$	0.89 ± 0.64
MACS	J0454.1-0300	0.538	$0.56^{+0.07}_{-0.03}$	$0.51^{+0.07}_{-0.06}$	$4.59^{+0.79}_{-0.68}$	9.15 ± 0.49	$0.87^{+0.11}_{-0.10}$	2.27 ± 1.50
MACS	J1423.8+2404	0.543	$0.44^{+0.02}_{-0.02}$	$0.25^{+0.04}_{-0.03}$	$2.30^{+0.39}_{-0.31}$	6.92 ± 0.32	$0.33^{+0.07}_{-0.08}$	0.31 ± 0.15
MACS	J1149.5+2223	0.544	$0.54^{+0.03}_{-0.03}$	$0.46^{+0.07}_{-0.06}$	$4.16^{+0.78}_{-0.62}$	8.50 ± 0.57	$1.09^{+0.17}_{-0.17}$	1.64 ± 1.23
MACS	J0018.5+1626	0.546	$0.58^{+0.03}_{-0.03}$	$0.54^{+0.08}_{-0.07}$	$4.87^{+0.82}_{-0.77}$	9.14 ± 0.43	$0.99^{+0.17}_{-0.14}$	0.67 ± 0.14
MACS	J0717.5+3745	0.546	$0.65^{+0.03}_{-0.04}$	$0.77^{+0.11}_{-0.10}$	$7.00^{+1.14}_{-1.09}$	11.84 ± 0.54	$1.08^{+0.22}_{-0.20}$	2.55 ± 1.26

Catalog	ID	z	r$_{2500}$ (Mpc)	M$_{gas,2500}$ $(10^{14}M_\odot)$	M$_{tot,2500}$ $(10^{14}M_\odot)$	kT (keV)	Y_{2500} $(10^{-10}$ ster)	w_{500} (10^{-2})
MS	2053.7-0449	0.583	$0.28^{+0.02}_{-0.02}$	$0.07^{+0.02}_{-0.01}$	$0.59^{+0.16}_{-0.12}$	4.45±0.58	$0.05^{+0.03}_{-0.02}$	1.02±0.31
MACS	J0025.4-1222	0.584	$0.45^{+0.04}_{-0.03}$	$0.26^{+0.06}_{-0.05}$	$2.38^{+0.66}_{-0.50}$	6.49±0.50	$0.28^{+0.06}_{-0.05}$	0.65±0.50
MACS	J2129.4-0741	0.589	$0.48^{+0.03}_{-0.02}$	$0.33^{+0.05}_{-0.04}$	$3.03^{+0.54}_{-0.43}$	8.57±0.74	$0.68^{+0.11}_{-0.10}$	1.51±0.69
MACS	J0647.7+7015	0.591	$0.52^{+0.02}_{-0.03}$	$0.42^{+0.05}_{-0.05}$	$3.83^{+0.51}_{-0.54}$	11.50±1.10	$0.84^{+0.14}_{-0.13}$	0.62±0.29
MACS	J0744.8+3927	0.698	$0.49^{+0.02}_{-0.02}$	$0.38^{+0.05}_{-0.04}$	$3.50^{+0.53}_{-0.46}$	8.08±0.44	$0.29^{+0.05}_{-0.05}$	1.60±0.11
MS	1054.4-0321	0.831	$0.44^{+0.03}_{-0.02}$	$0.34^{+0.07}_{-0.04}$	$3.16^{+0.71}_{-0.35}$	11.98±1.44	$0.30^{+0.06}_{-0.05}$	6.62±2.47
RXJ	0152.7-1357	0.833	$0.22^{+0.05}_{-0.03}$	$0.04^{+0.03}_{-0.01}$	$0.37^{+0.29}_{-0.12}$	6.48±0.90	$0.13^{+0.06}_{-0.03}$	8.22±1.02
CLJ	1226.9+3332	0.888	$0.42^{+0.02}_{-0.02}$	$0.31^{+0.04}_{-0.04}$	$2.77^{+0.45}_{-0.36}$	11.97±1.27	$0.32^{+0.06}_{-0.05}$	0.95±0.31

Note. — The X-ray and SZE-derived properties used in the BOXSZ scaling relations analysis and described in the text. The first three columns give the catalog, ID, and redshift. The references for the individual cluster redshift measurements are given in Sayers et al. [256]. The fourth column gives R_{2500} followed by $M_{gas,2500}$, $M_{tot,2500}$ and kT, which are calculated as described in Mantz et al. [166]. The $M_{gas,2500}$ and $M_{tot,2500}$ values were calculated specifically for this analysis. The eighth column gives Y_{2500} as measured using *Bolocam*. The last column gives the centroid shift parameter within R_{500} and is also described in the text.
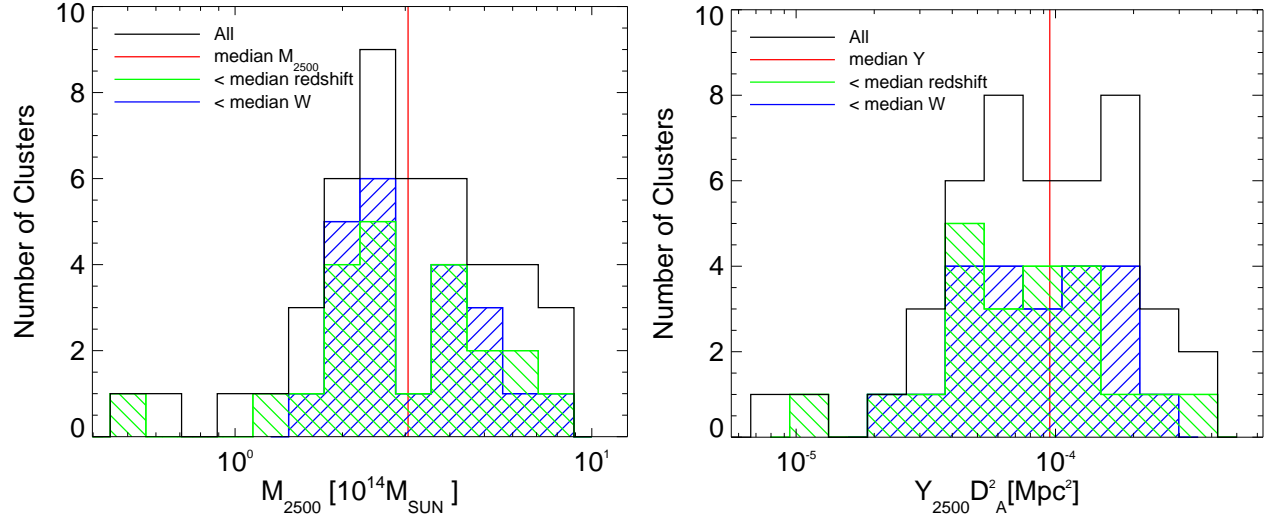
Figure 3.19 M_{2500} (left) and Y_{2500} (right) distributions for the BOXSZ cluster sample. Black histograms depict the entire sample with the red line indicating the median value. Note the logarithmic scaling of the x-axis. Green histograms depict the clusters with redshift values below the median $\langle z \rangle = 0.42$. Blue histograms depict the clusters with centroid shift parameters below $w = 7.2 \times 10^{-2}$, which have therefore been classified to be the most relaxed. Note the lack of significant bias in the distribution of morphological state and redshift with cluster mass.

Chapter 4

Bolocam Y_{SZ}-X-ray Scaling Relations

A precise understanding of how the SZE signal scales with cluster mass is needed in order for galaxy clusters to be competitive cosmological probes. Any observed deviations from self-similarity are interesting, because they indicate that the major physical processes within galaxy clusters are not scale-free. This is well-known for smaller clusters; however, clusters are expected to behave self-similarly above some mass scale, the precise value of which has yet to be determined. Our results indicate an SZE-mass scaling significantly shallower than self-similar, and significantly shallower than other SZE scaling relation results. This would suggest one of three things for the clusters under investigation: (1) the SZE signal has a weaker-than self-similar scaling with mass, (2) the mass proxy has a larger than unity scaling with the true cluster mass, or (3) there is a mis-calibration in the estimated error for one of both of the observables. Interestingly, the mass-proxy-independent *Bolocam*-SZE scaling relations are consistent with other analyses (such as Bonamente et al. [37], Andersson et al. [8], Planck Collaboration et al. [224]), these results are compiled in Table 4.3 and discussed in detail in Section 4.6 after the BOXSZ results are presented. This is promising, since it suggests that once the systematics between different X-ray mass proxies have been resolved, the integrated SZE signal can serve as a low-scatter mass proxy in future cosmological analyses.

4.1 Scaling Relation Parameterization

The scale-free nature of gravitational collapse leads to the prediction that gas-derived cluster observables scale in a self-similar fashion with total cluster mass. This can be reduced to a linear relation when the cluster properties are recast in logarithmic form:

$$m_{2500} \equiv \log_{10}\left[\frac{E(z)M_{2500}}{10^{14.5}M_\odot}\right] \tag{4.1}$$

$$m_{500} \equiv \log_{10}\left[\frac{E(z)M_{500}}{10^{15}M_\odot}\right] \tag{4.2}$$

$$l \equiv \log_{10}\left[\frac{L_{500}}{E(z)10^{44}\text{ergs}^{-1}}\right] \tag{4.3}$$

$$t \equiv \log_{10}\left[\frac{kT_{\text{ce}}}{\text{keV}}\right] \tag{4.4}$$

$$y_x \equiv \log_{10}\left[E(z)^{2/3}10^4 C_x\ kT_{ce}\ M_{gas,2500}\right] \tag{4.5}$$

$$y \equiv \log_{10}\left[E(z)^{2/3}10^4 D_A^2 Y_{2500}\right], \tag{4.6}$$

where the term

$$C_X = \frac{\sigma_T}{m_e c^2}\frac{1}{\rho_{\text{gas}}/n_e} = 1.406 \times \frac{10^{-5}\text{Mpc}^2}{10^{14}\text{keVM}_\odot} \tag{4.7}$$

normalizes Y_X to Y_{2500}, with σ_T being the Thompson cross-section, m_e and m_p, the electron and proton rest masses, respectively, and c the speed of light. For a highly ionized gas, $\rho_{\text{gas}}/n_e = 1.149m_p$. Using the logarithmic representations for the cluster observables, self-similarity can be formulated as a linear relation between the proposed cluster properties, p and q, as:

$$p = \beta_0^{p|q} + \beta_1^{p|q}q. \tag{4.8}$$

As discussed in Section 2.6.1, Kaiser [136] found that by including additional assumptions of self-similarity to the HSE equation, cluster temperature should scale logarithmically with cluster mass with $\beta_1^{t|m} = 2/3$. Extending this to the Y_{SZ} observable, which is a line-of-sight integral of cluster pressure and (in the limit that M_{gas} scales the same as M_{tot}) should scale

with the product of mass and temperature: $\beta_1^{y|m} = 5/3$. I refer to this type of scaling as HSE self-similar scaling and use it as a general standard of comparison.

Occasionally, the ensemble of fit parameters for a particular scaling relation will be referred to as $\theta_{p|q} = (\beta_0^{p|q}, \beta_1^{p|q}, \sigma_{p|q}^2)$, where $\sigma_{p|q}^2$ is the Gaussian intrinsic scatter of the observable $p \in [l, t, y]$ at a fixed q. Note the different integration apertures used for the X-ray scaling relations, which are necessary, since the Mantz et al. [166, hereafter M10] R_{500}-derived scaling relations will occassionally be utilized. When there is no explicit Δ subscript on m for β_0^{pm}, β_1^{pm}, and $\theta_{p|m}$, the integration aperture is assumed to be that of p.

The intrinsic scatter between different scaling relations might have covariance, for example, as significant non-thermal pressure support will affect all of the ICM-derived observables in some fashion. The symmetric covariance matrix can then be described as:

$$\rho_{LTY} = \begin{bmatrix} 1 & \rho_{LT} & \rho_{LY} \\ \rho_{LT} & 1 & \rho_{TY} \\ \rho_{LY} & \rho_{TY} & 1 \end{bmatrix}, \tag{4.9}$$

where the $[l, t, y]$ indices have been captilized for clarity. Covariance is not explicitly measured for the observed BOXSZ scaling relations, but it is utilized when generating mock sky realizations to characterize selection effects in Section 4.3. The off-diagonal elements of ρ_{LTY} are determined using a combination of empirical and simulated measurements. The $l - t$ covariance is adopted from M10b: $\rho_{LT} = 0.1$. As we are not aware of any observed constraints of ρ_{LY} and ρ_{TY}, the simulated results of Stanek et al. [267, hereafter S10] (particularly the "pre-heating" scenario) are used as a starting point from which to estimate our fiducial X-ray-Y_{SZ} covariance. The ρ_{TY} value is set to 0.6—which is the S10 simulated covariance between Y and a spectroscopic-like temperature. The situation with ρ_{LY} is slightly more complicated. M10b measured $\rho_{LT} = 0.1$, which is lower than the S10 value of 0.7. This is due to the use of bolometric luminosity in S10 versus the use of soft-band $[0.1 - 2.4]$ keV luminosity of M10b. As this analysis uses values of l calculated in an identical fashion to M10b, ρ_{LY} is set to 0.1 under the assumption that ρ_{LY} will be similar to ρ_{LT}. The selection bias would increase the more tightly l and y are correlated, since there is a strong selection effect on l.

Table 4.1.   Scaling Relations for BOXSZ Cluster Sample.

θ	β_1	β_0	σ
$Y_{2500} - M_{2500}$	1.16±0.12	-0.09±0.03	0.11±0.03
$Y_X - M_{2500}$	1.46±0.05	-0.52±0.01	0.04±0.02
$Y_{2500} - Y_X$	0.84±0.07	0.33±0.03	0.09±0.03
$T_X - M_{2500}$	0.45±0.05	-0.18±0.01	0.06±0.01
$T_X - M_{500}$	0.50±0.05	0.80±0.01	0.06±0.01
$L_{500} - M_{500}$	1.06±0.12	0.87±0.03	0.13±0.02

Note. — Corrected BOXSZ scaling relations parameters: slope (β_1), intercept (β_0), and intrinsic scatter (σ.) The small level of intrinsic scatter in $\theta_{y_x|m_{2500}}$ is indicative of the high amount of correlation between the two axes. Due to subtleties of the selection function process, the Y_{2500}-Y_X was not corrected for selection bias and the Y_X-M_{2500} and T_X-M_{2500} relations adopt the T_X-M_{500} selection function correction.

The following sections will characterize the bias due to selection function effects and fitting bias. Section 4.2 explores possible biases due to the fitting method. Section 4.3 studies the selection function effects of the BOXSZ sample, and Section 4.4 explores modeling bias and evolution of the scaling relations for physically distinct subsets of clusters. The corrections to the BOXSZ scaling relations are given in Table 4.2, and the corrected relations are given in Table 4.1.

4.2   Fit Method and Characterization

The adopted fitting method must account for measurement error in all observables, and also any additional intrinsic scatter that can arise through various physical processes (e.g., cluster asphericity and non-thermal pressure support). Two different fitting methods that account for measurement error in both the covariate (the x-axis) and the response (the y-axis) and also fit for Gaussian intrinsic scatter in the response have been examined. The first is a

generalized least squares method (GLS), described in [275], and the second is a Bayesian fitting method, linmix_err[1] (LME), described in [139]. The particular biases of the two fitting methods are examined using a proposed set of scaling relations (which includes Gaussian intrinsic scatter) applied to the observed covariates of the BOXSZ sample. Measurement noise is added to each mock observable, either Gaussian or, when available, directly sampled from the noise realizations discussed in section 3.7. A scaling relation is then fit to these mock observables, and the difference between the input and the best-fit scaling relations gives an estimate of the fitting bias. The process is repeated for a variety of scaling relation parameters. The bias is most sensitive to the intrinsic scatter parameter, and some of the output values are shown in Figure 4.1.

The left-hand plot of Figure 4.1 demonstrates that there is very little constraining power for scatter less than 5%. This is due to the constraint that intrinsic scatter must be positive in light of significant measurement noise. With an input intrinsic scatter above 10%, the LME method with Gaussian noise approaches zero bias (the green dashed line). An interesting observation is that if the noise realizations are sampled instead of assuming Gaussian noise, there is a negative bias when the input intrinsic scatter is greater than ~ 0.05. As can be seen in the righthand plot of Figure 4.1, the bias of the generalized least square method (GLS) is always larger than that of the LME method for Gaussian noise. For the intrinsic scatter values relevant to the BOXSZ $\theta_{y|m}$ relation, there is very little bias in the measured slope and intercept of the fit. These two methods provide results that are negligibly different, given the measurement uncertainty. The LME method, however, was ultimately chosen, because it properly accounts for covariance between the various fit parameters.

4.3   Modeling the Selection Function

All of the clusters in the BOXSZ sample were selected based on the availability of *Chandra* X-ray data. In addition to this, several other factors affected the selection process. First, clusters were generally chosen to have high X-ray luminosities and spectroscopic tempera-

---

[1]The linmix_err IDL code can be downloaded at `http://idlastro.gsfc.nasa.gov/ftp/pro/math/linmix_err.pro`.
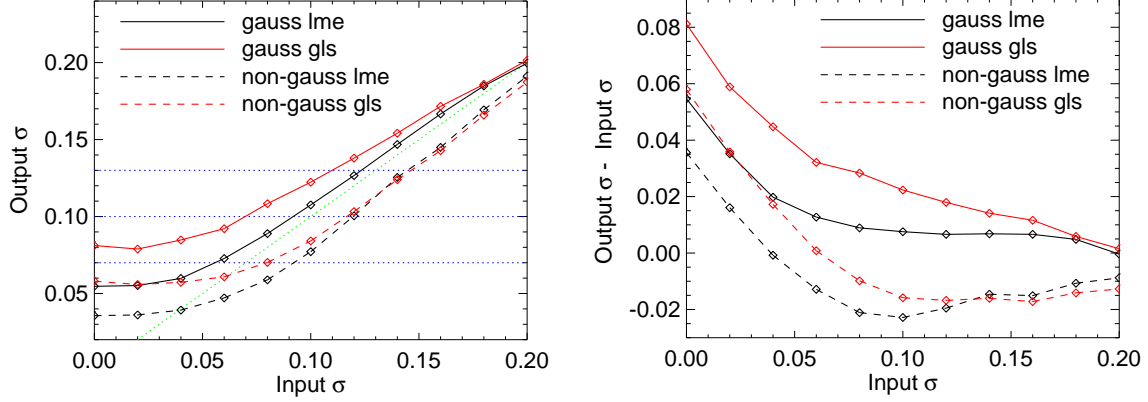
Figure 4.1 The fitting method bias for the BOXSZ sample for various input levels of intrinsic scatter, and a nominal slope and intercept of 1.2 and -0.08, respectively. The solid and dashed lines represent sampling noise from either a Gaussian noise distribution or from the noise realizations described in Section 3.7, respectively. The red and black lines represent the GLS and LME fitting methods, respectively. The green line has a slope of one and indicates where the measured intrinsic scatter matches the input intrinsic scatter. There is limited constraining power in the measured intrinsic scatter for values less than $\sim 8\%$. Above this level, the LME fitting method has the least amount of measurement bias in intrinsic scatter under the assumption of Gaussian noise.

tures, under the expectation that these X-ray observables would correlate with a bright SZE signal. Second, moderate redshift clusters were generally selected to ensure that the cluster's R_{500} would be within the resulting $14' \times 14'$ *Bolocam* image. Finally, because there already was a large degree of overlap with the MACS high redshift ($z > 0.5$) and CLASH samples (which are discussed in Appendix A), a few clusters were chosen to complete these catalogs.

Out of concern that selection effects would bias the results of the scaling relation, I developed a method to characterize this selection function using the structure formation theory reviewed in Section 1.4. Observers using pointed or serendipitous observations are often in a position where they do not have a rigorously defined selection function; the selection function characterization method described below should be generally applicable to these types of samples as well.

First, mock sky realizations are generated by sampling the Tinker et al. [273] mass function given in Equation 1.35 for a grid of mass and redshift values. A conservative mass range is chosen that adequately describes the BOXSZ sample: approximately 9×10^{13} to $4 \times 10^{15} M_{\odot}$ at R_{500}. It has been confirmed that the selection function characterization

is insensitive to any extension of mass range or cluster density in the mock sky realizations. The sum of all the grid points represents the total mean number of clusters in the parameter range of interest. The Tinker et al. [273] mass function (Equation 1.34) parameters given for $\Delta = 300\Omega_m(z)$ ($[A, a, b, c] = [0.200, 1.52, 2.25, 1.27]$) were chosen, since these are the same parameters used in the M10 analysis. Instead of generating a mock sky realization within the specific solid angle observable with *Bolocam* (dV/dz), the sky is over-populated with enough clusters in order not to introduce artificial selection effects. This ends up corresponding to about 10 times the solid-angle observable with *Bolocam* and 40 times the solid angle was ultimately chosen to reduce the noise in the measurement. The exact justification for this approach is discussed in more detail later when the cluster selection process is described.

The process is randomized by assigning each grid point (representing a specific mass and redshift range) to a probability-weighted segment in the interval $[0.0, 1.0]$. These probability weights are determined from the mean number of clusters assigned to the particular grid point by the Tinker mass function. The $[0.0, 1.0]$ interval is then then randomly sampled, and when the segment assigned to a particular grid point is chosen, the mass and redshift of that grid point is assigned to one cluster realization. The interval is repeatedly sampled until the total number of clusters corresponds to the total mean number of clusters of the proposed solid angle, which ends up being about 10^5 clusters. For each of the 45 clusters in the BOXSZ sample, observables are then generated for all mock clusters within $\Delta z = \pm 0.02$ of the given BOXSZ cluster redshift. Next, M_{2500} values are generated from the value of M_{500} for each mock cluster by directly sampling the observed M_{2500} to M_{500} ratio from the MCMC chains generated in connection with the M10b analysis and discussed in section 3.7.

A set, Θ, of observable-mass scaling relations, is applied to the sampled mock cluster masses to generate nominal l,t, and y observables. This process includes covariance between the intrinsic scatter, ρ_{LTY}, which is defined in Section 4.1. It is worth noting that while Θ is the same for all of the clusters for a given realization of the selection function, the M_{500}-M_{2500} ratio is specific to each cluster under investigation. Initially, Θ is constructed using the X-ray-only scaling relations from M10b and the uncorrected best-fit $\theta_{y|m}$.

With a full set of observables for each mock cluster in a particular redshift slice ($\Delta z = \pm 0.02$) of a given BOXSZ cluster, the mock cluster that most closely matches the measured

X-ray properties of the given BOXSZ cluster is selected according to:

$$[m_{i,sim}, l_{i,sim}, t_{i,sim}, y_{i,sim}] = \max(exp((l_i - l_{sim})^2/(s_l)^2 + (t_i - t_{sim})^2/(s_t)^2)), \qquad (4.10)$$

where the subscript sim denotes the values for the mock clusters, and s_l and s_t denote the measurement errors on l and t for the given BOXSZ cluster i. As many of the BOXSZ clusters were selected in part, or entirely, due to their observed l and t, this likelihood function selects the mock clusters with the most similar values of these two observables. Consequently, the underlying mass function is indirectly sampled, which in turn provides the associated distribution of Y_{SZ} values for the given X-ray characteristics of the BOXSZ selection. The true Y_{SZ} value for each selected mock cluster is then perturbed by one of the 1000 noise realizations described in section 3.7. The above process is repeated for each cluster 1000 times—generating 1000 sets of mock BOXSZ observables, or simBOXSZ.

The likelihood function justifies the choice to overpopulate the mass function. Given the rarity of the high mass clusters in the BOXSZ sample, a realistically populated sky produces a very small number of mock clusters from which to select possible counterparts to the true BOXSZ clusters. The nature of the Eddington bias [76] is such that for a mass-dependent observable with a large amount of scatter and a steeply falling mass function, a measurement of this observable is more likely to be represented by a low-mass cluster that has an upwards scattered value than a higher-mass cluster with the observed value lying directly on the given scaling relation. As the lumininosity observables from the BOXSZ clusters have already been measured, it is only desired to sample the underlying mass function. Without populating the sky densely enough, ∼10 skies, the mock luminosities selected from such a sample would be, on average, lower and would not be representative, introducing an additional, unwanted "selection" effect.

An example of the selection process is given in Figure 4.2. The figure depicts the distribution of L_{500} versus T_X for one of the simBOXSZ realizations. The green arrows indicate the position from the observed BOXSZ parameters to the output parameters for a single simBOXSZ realization. Due to the increased density at the low-mass end of the mass function, it is extremely likely to find a cluster in the simulation with the exact luminosity-temperature
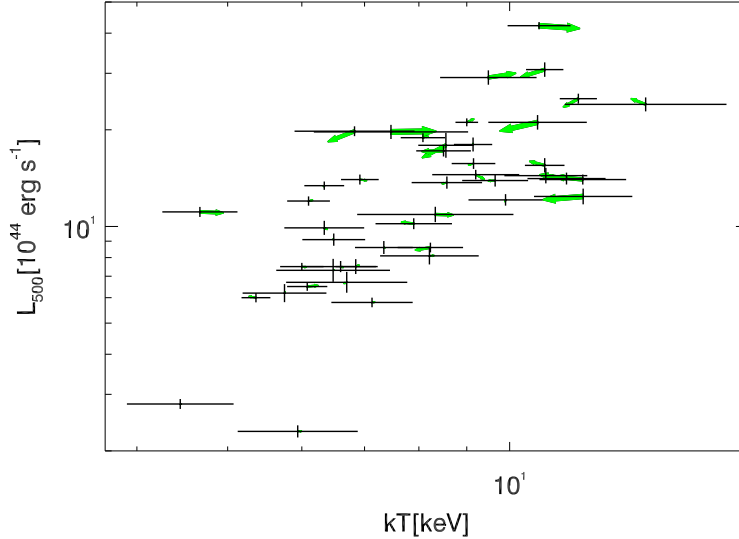
Figure 4.2 Figure depicting one iteration of the selection function simulation for a volume of 10 observable skies. Black points represent the observed L_{500}/T_{500} values. The green arrows point to the position of the simBOXSZ-selected counterparts for a single iteration of the selection function method. The arrows point primarily in the temperature direction, because the relative measurement uncertainty is larger in that direction. Also, there is more variation for hotter, brighter clusters because the mass function is less dense in that region. Averaged over all 1000 iterations, the simBOXSZ values of L_{500} and T_{500} match those of the observed sample and the uncertainty in the measured scaling relations is plotted in Figure 4.6. The size of these arrows decreases for 40 observable skies and changes the characterization of the selection function to less than a fraction of a standard deviation.

parameters as the cluster under consideration. At the more massive end, the difference between the measured and mock parameters is generally within the measurement error. The final cluster density was chosen at the point where increasing the density of clusters does not change the results by more than $\sim 10\%$ of the measurement error, but is low enough to maximize computational speed.

Scaling relations are then fit to each of the simBOXSZ, and the median fit parameters over the 1000 simBOXSZ are computed. The median simBOXSZ scaling relation parameters are then compared to the naive scaling relation fit to the true BOXSZ data. This entire selection process is then iterated, perturbing the input Θ until the median fit parameters to the simBOXSZ clusters matches the best fit parameters to the true BOXSZ data. Comparisons between the BOXSZ and the simBOXSZ-measured $\theta_{l|m}$, $\theta_{t|m}$, and $\theta_{y|m}$ scaling relations are shown in Figures 4.3, 4.4, and 4.5, respectively.
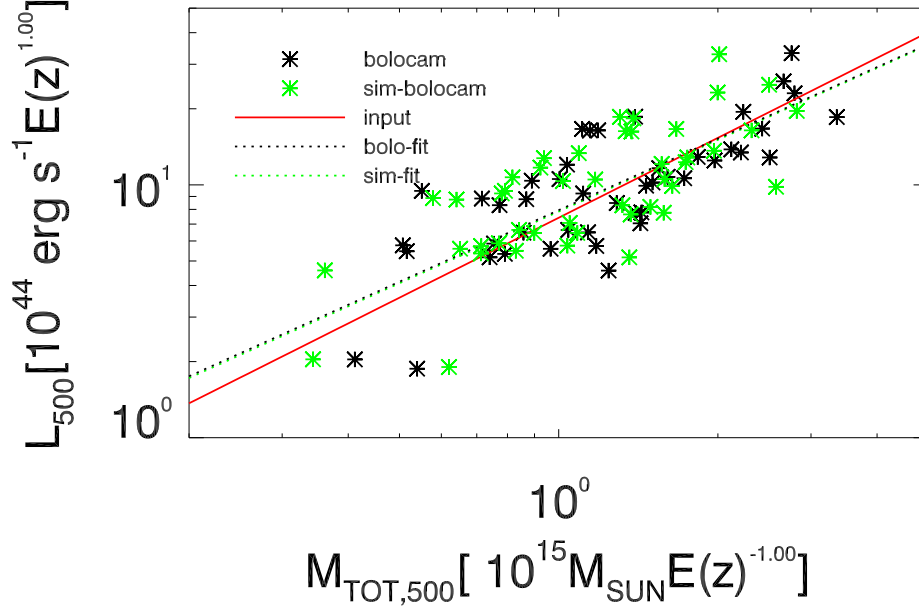
Figure 4.3 Measured BOXSZ values of M_{500} and L_{500} (black asterixes) together with one simBOXSZ realization (green asterixes). The BOXSZ-observed, the simBOXSZ input, and the median overall of the simBOXSZ measured output $\theta_{l|m}$ are represented by the dashed black, solid red, and dashed green lines, respectively. $\theta_{l|m}$ experiences the strongest selection effect, because it is the sole variable in the X-ray selection process for most of the clusters.

In Figure 4.6 the observed and mock scaling relation parameters for the BOXSZ sample together with their covariance are compared. The median simBOXSZ Θ is chosen to match the naive best-fit to the true BOXSZ. Once input values of Θ to the simBOXSZ have converged, so that the output values of Θ from the simBOXSZ match the best-fit parameters of the true BOXSZ data, the values of Θ input to the simBOXSZ are perturbed around their measurement uncertainties to observe the consequent effect on the output values of Θ from the simBOXSZ fits.

The output $\beta_0^{y|m}$ and $\beta_1^{y|m}$ bias is much smaller than the measurement error (i.e. the median fit of the simBOXSZ closely matches the input value), while the intrinsic scatter is biased lower by approximately half of a standard deviation. Referring back to Section 4.2, the bias in intrinsic scatter is therefore almost entirely due to the limitations of the employed fitting method. The selection function has very little impact on the corrected results for two main reasons: first, the low intrinsic scatter of the signal with fixed cluster mass reduces the overall level of Eddington bias. Second, the low amount of covariance
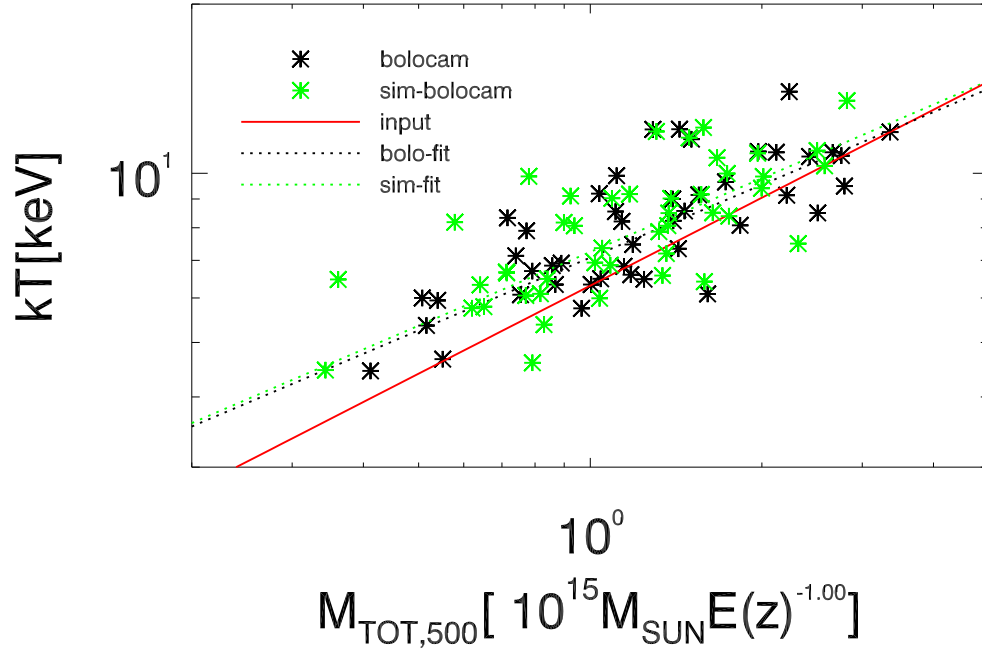
Figure 4.4 Analogous to Figure 4.3 but for T_X-M_{500}
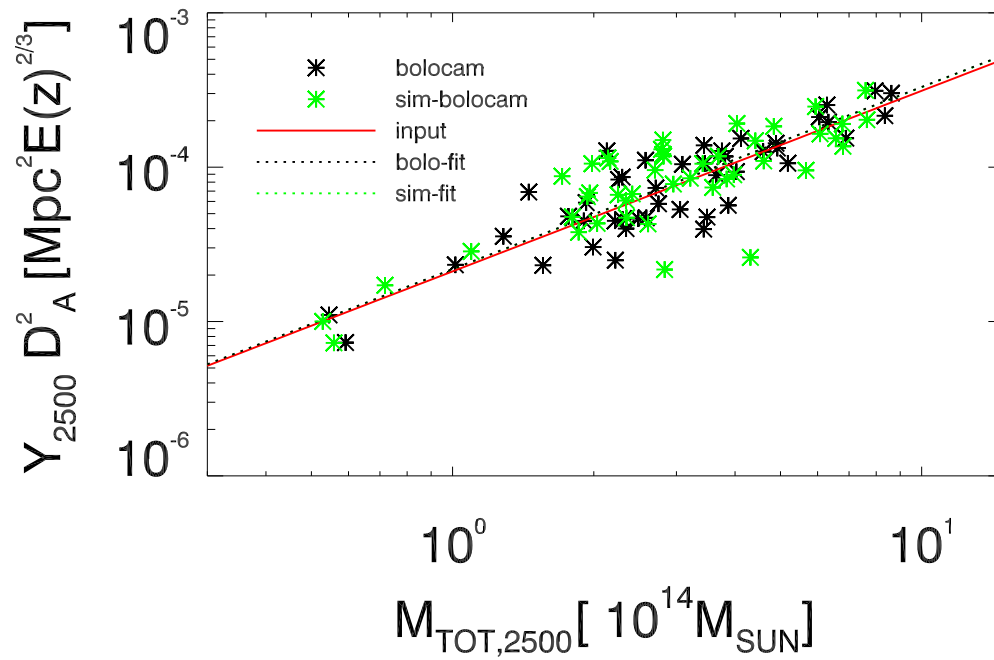
Figure 4.5 Analogous to Figure 4.3 but for Y_{2500}-M_{2500}

Table 4.2.   Scaling Relations Corrections for BOXSZ Cluster Sample.

θ	$\Delta\beta_1$	$\Delta\beta_0$	$\Delta\sigma$
$Y_{2500} - M_{2500}$	0.02	0.02	-0.02
$T_X - M_{500}$	-0.07	0.05	-0.01
$L_{500} - M_{500}$	-0.12	0.03	0.02

Note. — The measure output minus the input scaling relation parameters for the simBOXSZ. While selection effects can be identified for the luminosity scaling relations, Y_{SZ} suffers little selection bias.

between the luminosity and the SZE signal ensure very little cross-over selection effects between the SZE and luminosity. Finally, lower mass clusters received longer integration times, so the introduction of a Malmquist bias due to a hard flux cut-off (such as with a survey of uniform depth) does not necessarily apply for the BOXSZ scaling relations. The final corrections to the scaling relations are presented in Table 4.2.

4.4   Physically Motivated $\theta_{y|m}$ Consistency Checks

A range of consistency checks have been performed on the data not only to test the robustness of the results, but also to search for possible physical effects that are not described by the parameteriztion chosen for the scaling relations.

First, the redshift dependence on the derived $\theta_{y|m}$ is considered by evenly splitting the sample based on redshift and fitting each subset independently. The results are statistically consistent with each other, indicating that there is no strong redshift dependence of the results. Due to significant correlation between X-ray morphological state and redshift in the BOXSZ cluster sample (almost all of the most disturbed systems are in the high-redshift sub-sample), this test also demonstrates that the results do not depend strongly on cluster morphology. Another important note is that since the physical value of R_{2500} (in Mpc) is relatively constant over the sample, splitting based on redshift also approximately splits the
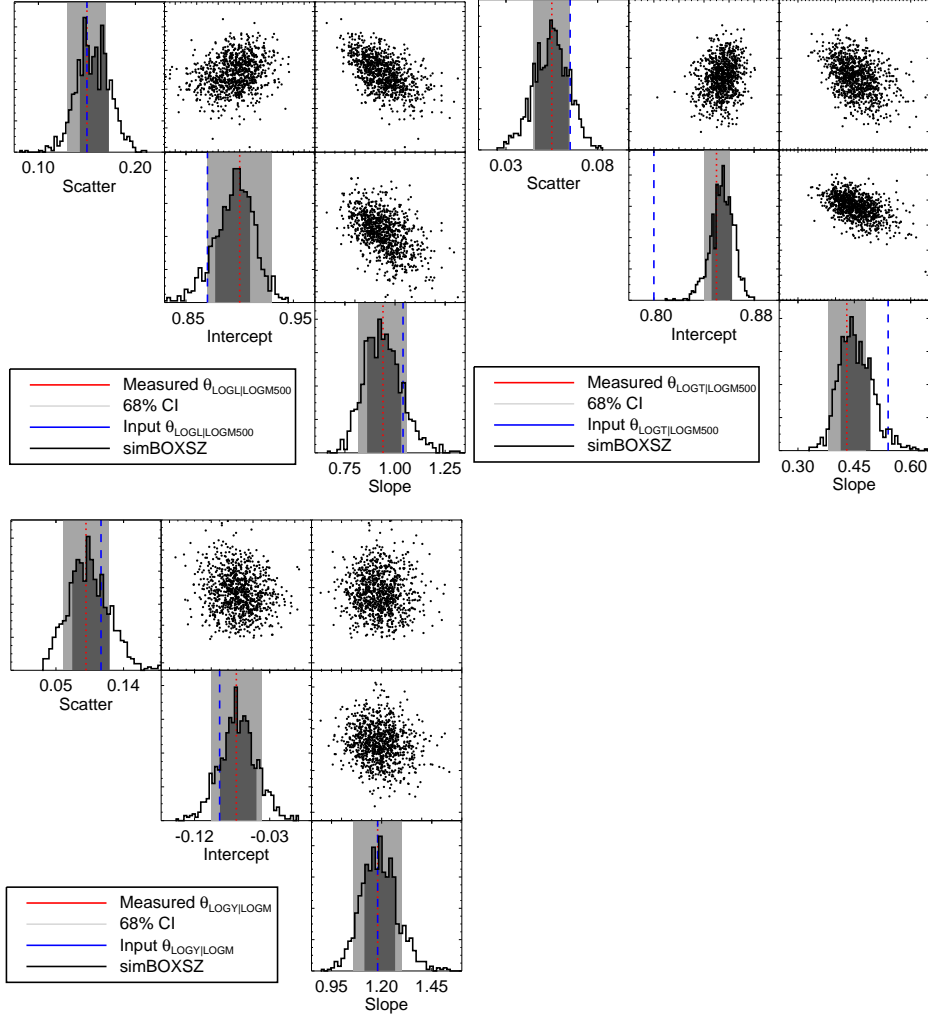
Figure 4.6 Distribution of output simBOXSZ $\theta_{l|m}$, $\theta_{t|m}$, and $\theta_{y|m}$ measurements (black histograms). The dashed blue lines indicate the value of the input scaling relations, and the dashed red-lines indicate the observed BOXSZ values. The light gray shading represents the 68.2-percentile confidence region of the observed BOXSZ parameters, assuming Gaussian noise. The dark gray region indicates the inner 68.2-percentile confidence region of the measured simBOXSZ relations. The covariance in the X-ray only scaling relations is due to the non-zero intercept of the scaling relation, which correlates the slope with the intercept. Note the similarity between the uncertainty due to the Gaussian fitting compared with directly sampling the noise realizations.

sample based on angular size. Therefore, there is also no evidence that the scaling relation results depend on cluster angular size, indicating that the high-pass filtering (and consequent deconvolution, including the signal offset estimation) does not have a significant effect on our results.

The model-dependence of these results is also explored by repeating the measurements of $\theta_{y|m}$, but instead of using the minimal model prescribed by the F-test, $\theta_{y|m}$ is fit to the Y_{2500} values derived from SZE maps, where both the transfer function and the signal offset are determined with the 1-model. While the F-test selected the 1-model for only 16 of the BOXSZ clusters, the corrected 1-model scaling relations are also consistent with the F-test-derived values. This is a promising result in regards to pressure model-derived scaling relations, such as those measured by the Planck Collaboration et al. [224].

Finally, the derived Y_{2500} values and their associated scaling relations are examined by adopting the morphologically-dependent pressure profile parameters given in A10. These results are indistinguishable from the results using the universal A10 profile to constrain the large-scale contributions to Y_{2500}, further indicating that the results do not depend strongly on the adopted parametric model to constrain the signal offset.

4.5 Scaling Relations Discussion

The results of the BOXSZ scaling relations analysis and presented in Table 4.1 will now be discussed. The general theory behind the measurement of these observables was discussed in Section 2.2.2 for T_X, Section 2.2.3 for M_{gas}, and Section 2.3.1 for Y_{SZ}. Sections 3.2 and 3.7 discuss the specific measurement techniques adopted for the BOXSZ analysis. Notably, the fiducial integration radius for the BOXSZ Y_{SZ}, M_{gas}, and M_{tot} values is R_{2500}, while the fiducial integration radius for the BOXSZ T_X is R_{500}. M_{tot} is evaluated using M_{gas} and adopting a constant $f_{gas} = 0.1104$ value with an 8% global systematic gaussian uncertainty.

4.5.1 BOXSZ $T_X|M_{500}$ and $T_X|M_{2500}$

As X-ray observables are derived from the physics of the ICM, their scaling relations are expected to relate to the SZE ones more than any other observational probe. The BOXSZ
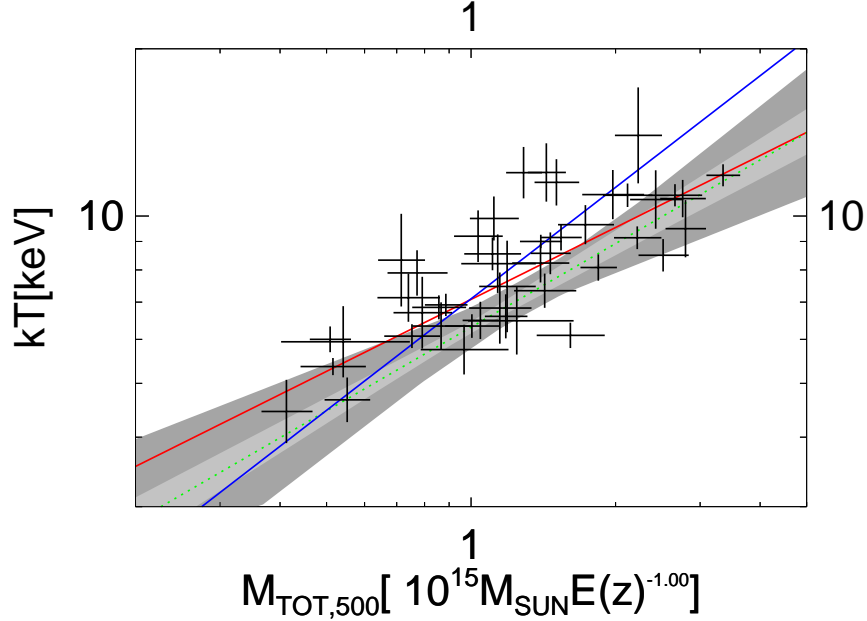
Figure 4.7 Observed T_X-M_{500} scaling relations for the BOXSZ sample. The black data points represent the measured parameter values. The solid red line respresents the uncorrected best-fit to the data. The blue line represents the uncorrected best-fit to the data with a self-similar slope. The green dashed line represents the scaling relations corrected for selection function, and fitting bias effects with 1σ and 2σ confidence contours, depicted by the light gray and dark gray shading, respectively. The T_X-M_{500} is presented mainly in the context of interpreting the Y_{2500}-M_{2500} and Y_{2500}-Y_X results.

cluster sample can be considered, for the most part, a subset of the M10b sample, and therefore the M10b measured X-ray scaling relations are expected to hold for the BOXSZ sample as well. To best compare the X-ray to the SZE scaling relations, however, they should represent the same cluster sample, and the cluster parameters should be measured within the same integration aperture. To understand the sample selection effect, $\theta_{t|m}$ is measured specifically for the BOXSZ subsample and is plotted in Figure 4.7. The red line indicates the uncorrected fit, the blue line is the uncorrected fit to a self-similar slope of 2/3, and the green line is the corrected fit with the 1σ and 2σ confidence intervals shown in light and dark gray, respectively. The selection function makes the slope slightly shallower, indicating the selection preference for hot, low-mass clusters. The corrected BOXSZ-measured $\beta_1^{t|m} = 0.50\pm$ 0.05 is consistent with the M10b-measured $\beta_1^{t|m} = 0.49 \pm 0.04$ for their full cluster sample.

Since the T_X values are the same, any variations in the slope of BOXSZ-measured $\theta_{t|m_{2500}}$ and $\theta_{t|m}$ scaling relations indicates a mass dependency in the concentration (r_{scale}/r_{200})
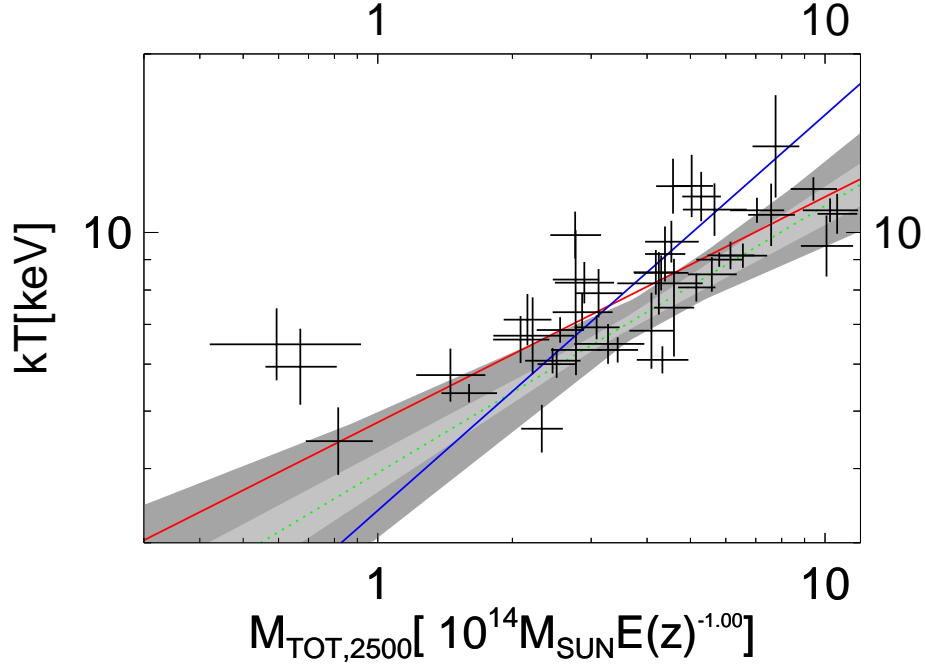
Figure 4.8 Analogous to Figure 4.7 but for the $\theta_{t|m_{2500}}$ scaling relations. The bias incurred by the selection function is not explicitly measured for these scaling relations and the correction to the $\theta_{t|m}$ fit, measured at R_{500}, is used instead.

of the clusters. For ease of calculation, T_X is always determined within the region $[0.15, 1.0]R_{500}$ since the measurements are negligibly different for T_X evaluated between $[0.15, 0.5]R_{500}$ (recall that $0.5R_{500} \approx R_{2500}$).[2] The selection function process derives T_X directly from M_{500}. Since there is scatter between the ratio of M_{2500} and M_{500} ratio for each individual cluster, the $T_X|M_{2500}$ selection effect cannot be directly derived unless a specific $T_X|M_{2500}$ scaling relation is proposed and the implementation of this would be non-trivial. As there is no observational evidence that the two values should behave differently, the $T_X|M_{500}$ selection correction is adopted for the $T_X|M_{2500}$ relation. The BOXSZ-measured $\beta_1^{t|m_{2500}} = 0.45 \pm 0.05$ is approximately 1-σ shallower than the M10b $\beta_1^{t|m}$ value with the BOXSZ $\theta_{t|m_{2500}}$ scaling relation plotted in Figure 4.8. M_{500} is only used in this section to identify the changes in the $\beta_1^{t|m}$ values when going from R_{500} to R_{2500}. any subsequent reference to the BOXSZ X-ray scaling relations will imply $M_{gas,2500}$ and $M_{tot,2500}$.

---

[2]M10 measure $T_{[0.15-1.0]R_{500}}/T_{[0.15-0.5]R_{500}} = 0.957 \pm 0.009$, this result is supported by Vikhlinin et al. [279], who measure $T_{[0.15-1.0]R_{500}}/T_{[0.15-0.5]R_{500}} = 0.9075 + 0.00625T_{[0.15-0.5]R_{500}}$ with a 3% observed scatter in the relation (plotted in Figure 6 of Section 4.1.1 in [279]).
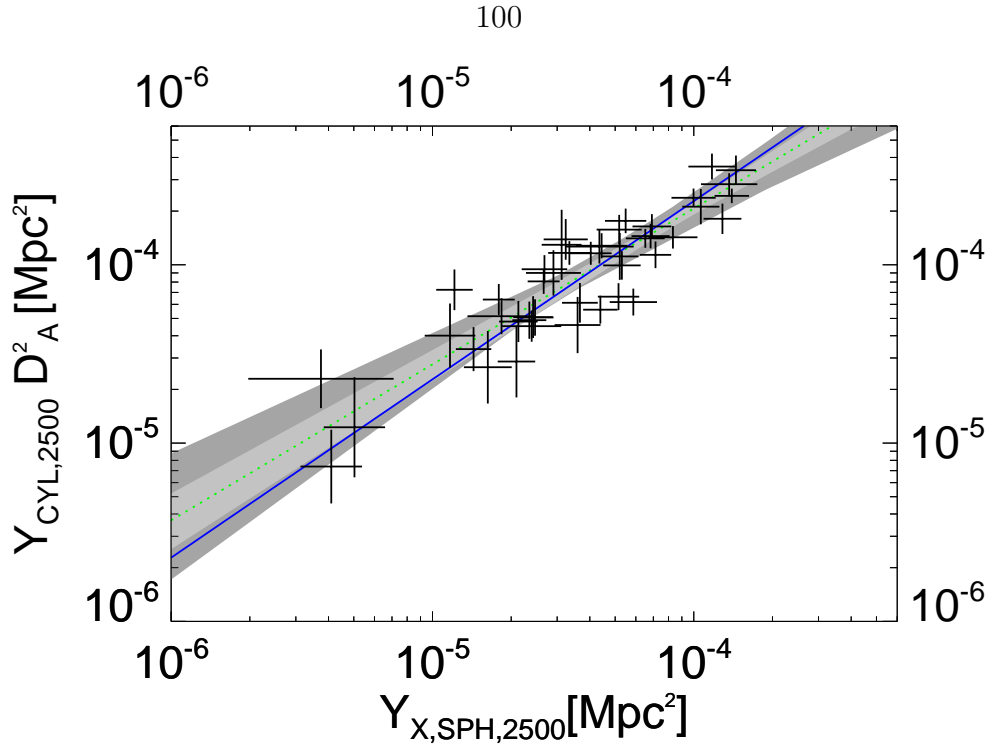
Figure 4.9 Analogous to Figure 4.7 but for the Y_{2500}-Y_X scaling relations. Due to the uncertainty in the covariance in the scatter between these two values, the relation is not corrected for selection effects.

4.5.2 BOXSZ Y_{2500}-Y_X

As discussed in previous sections, Y_X is predicted to be a good approximation for Y_{SZ} in the limit where spectroscopic temperature is equivalent to mass-weighted temperature (Kravtsov et al. [148]). Given the Rozo et al. [244] observation that M_{gas} and T_X observations between different X-ray groups are consistent with each other, the $\theta_{y|y_x}$ relation allows Y_{SZ} measurements between different SZE groups to be compared independent of the choice of mass proxy. This relation is not corrected for selection effects as the fiducial set of scaling relations, Θ, does not account for selection effects for M_{gas}, independent on M_{tot}. The BOXSZ measured $\beta_1^{y|y_x}=0.84 \pm 0.07$ is shallower than unity and the $\theta_{y|y_x}$ scaling relation is plotted in Figure 4.9. This result is in agreement with other analyses (Bonamente et al. [37], Andersson et al. [8], Planck Collaboration et al. [224]). The different analysis results are compiled in Table 4.3 and these results are compared in detail in Section 4.6.
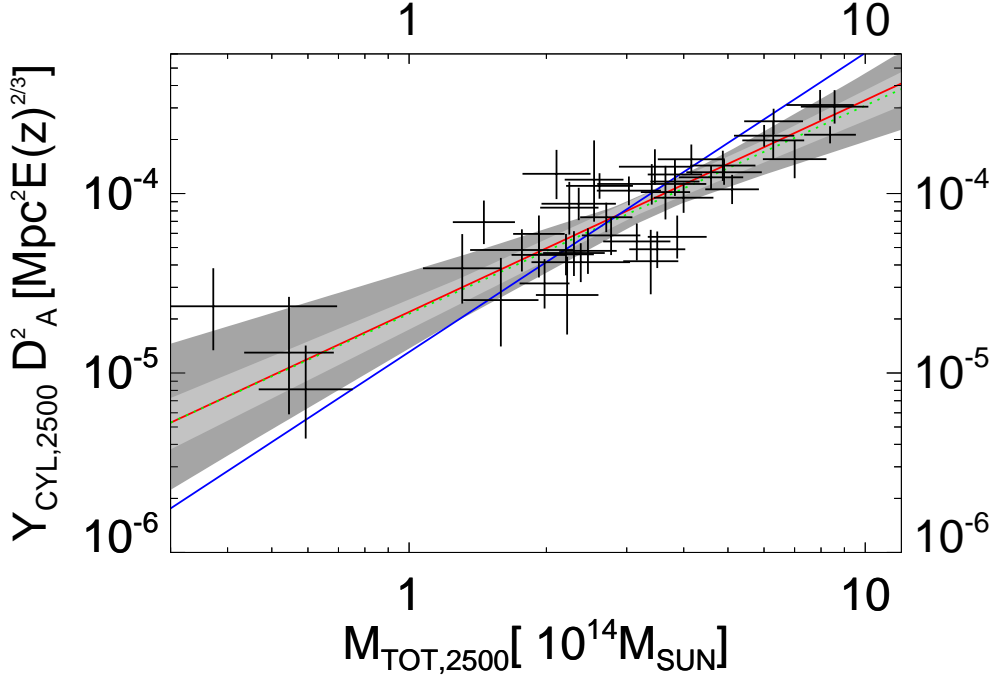
Figure 4.10 Analogous to Figure 4.7 but for the Y_{2500}-M_{2500} scaling relations.

4.5.3   BOXSZ Y_{2500}-M_{2500}

The SZE-mass scaling is a key ingredient for SZE-based cluster cosmology. The BOXSZ-measured $\beta_1^{y|m} = 1.16 \pm 0.12$ —over 4σ shallower than the HSE self-similar slope of 5/3, and the $\theta_{y|m}$ relation is plotted in Figure 4.10 . This result is now compared to $\theta_{y_x|m}$, the X-ray analog of $\theta_{y|m}$. An approximate 2-σ deviation in $\beta_1^{y|m}$ from self-similarity can be identified in the M10b-measured $\beta_1^{y_x|m_{500}} = 1.48 \pm 0.04$. The BOXSZ-measured $\beta_1^{y_x|m} = 1.46 \pm 0.05$ is consistent with these results, which is corrected using the $\theta_{t|m}$ selection correction. The final approximate 2σ deviation is given by the non-unity $\beta_1^{y|y_x} = 0.84 \pm 0.07$ measurement which could be due to non-self-similar scaling between the SZE and the X-ray pressure proxy.

4.6   Comparison with Previous Results

Table 4.3 lists some of the relevant characteristics and main results of the three main SZE-X-ray scaling relation studies used for comparison with the BOXSZ scaling relations analysis: Bonamente et al. [37, hereafter B08], Planck Collaboration et al. [224, hereafter P11], and

Table 4.3.   Sample Characteristics of Various X-ray and SZE Scaling Relations Analyses.

Name	Instrum.	Proxy	β_{ym}^1	σ_{ym}	$\beta_{yy_x}^1$	$\sigma_{yy_x}^1$	N_{cl} LZ:HZ:All	M_{500} $10^{14} M_\odot$
This work	*Bolocam*/CXO	M_{gas}	1.16 ± 0.12	0.11 ± 0.03	0.84 ± 0.07	0.09 ± 0.03	$22 : 23 : 45$	$[3.9, 24.9]$
B08	CXO/OB	HSE	1.66 ± 0.20		$\cdots$		$22 : 16 : 38$	$\sim [2.0, 16.2]$
A11	SPT	Y_X	1.67 ± 0.29	0.09 ± 0.05	0.90 ± 0.17	0.07 ± 0.05	$3 : 12 : 15$	$[3.5, 11.8]$
P11	*Planck*/XMM	Y_X	1.74 ± 0.08	0.10 ± 0.01	0.95 ± 0.04	0.10 ± 0.01	$59 : 3 : 62$	$[2.4, 19.7]$

Note. — A compilation of scaling relations from several SZE analyses discussed in the text that have calibrated M_{tot} using X-ray proxies. The first column indicates the particular SZE-X-ray analysis. The second column indicates the instrument with which the data was taken. (CXO) *Chandra X-Ray Observatory* (OB) OVRO/BIMA. In the second column from the right right, HZ and LZ represent the number of clusters above and below the BOXSZ median redshift of $\langle z \rangle = 0.42$. In addition to the $\beta_1^{y|m}$ results, Bonamente et al. [37, B08] and Planck Collaboration et al. [224, P11] measure $\beta_1^{y|m_{gas}} = 1.41 \pm 0.13$ and 1.39 ± 0.06, respectively. For Andersson et al. [8, A11], the $\beta_1^{y|m}$ values are given for Y_{spher} and the $\beta_1^{y|y_x}$ values are given for Y_{cyl}. Despite the variety in $\theta_{y|m}$ relations, the $\theta_{y|m_{gas}}$ and $\theta_{y|y_x}$ relations are fairly consistent between the various SZE scaling relation studies. This is further supported in light of the Rozo et al. [246] re-analysis of the *Planck* $\theta_{y|y_x}$ relation, where they measure $\beta_1^{y|y_x} = 0.917 \pm 0.039$. The B08 M_{500} values are approximated from the measured M_{2500} values (solely for the purposes of a general comparison) by multiplying them by a factor of 2.

Andersson et al. [8, hereafter A11]. Direct comparison between these different scaling relations, however, is made challenging in light of the differences in the adopted integration apertures and X-ray mass proxies. Specifically, nearly every SZE scaling relations analysis uses a different mass proxy, and these are known to suffer systematic effects, such as those discussed in Section 2.6.1.2. Therefore, the BOXSZ $\beta_1^{y|m}$ measurements will be compared with the $\beta_1^{y|m_{gas}}$ and $\beta_1^{y|y_x}$ measurements of the other studies when available.

B08 present some of the first observed $Y_{SZ}|M_{tot}$ scaling relations between OVRO/BIMA SZE and *Chandra* X-ray observations within $\Delta = 2500$. The B08 sample consists of 38 clusters with a median redshift of $z = 0.30$. The B08 M_{2500} distribution spans approximately an order of magnitude from $1.0 - 8.1 \times 10^{14}$ $M_\odot$. Of the three SZE cluster samples that are considered here, this sample shares most in common with BOXSZ in terms of the physical parameters of the cluster samples under investigation. In fact, BOXSZ shares 21 clusters in common with the B08 sample. In contrast to this analysis, the B08 results are derived from a joint analysis of the SZE and the X-ray data fit to a spherical β-model, the model originally proposed by Cavaliere & Fusco-Femiano [52] and discussed in Section 2.2.1. The

clusters are assumed to be isothermal and in HSE. B08 measure a $\beta_1^{y|m_{gas}} = 1.41 \pm 0.13$ and $\beta_1^{y|m} = 1.66 \pm 0.20$, and do not measure any scaling of f_{gas} with mass or redshift.

Encouraged by the similarities between the two cluster samples, the B08 and BOXSZ measurements are directly compared. Figure 4.11 confirms the high-degree of similarity between the measured observables of the two samples. Using the hydrostatically-derived B08 M_{tot} values, $\theta_{y|m}$ is measured using the same fitting adopted for the current analysis. Very similar values to the BOXSZ sample are derived: $\beta_1^{y|m} = 1.15 \pm 0.15$, $\beta_0^{y|m} = -0.14 \pm 0.03$, and a $\sigma_{y|m} = 0.12 \pm 0.02$. The original B08 best-fit and the new best-fit are also overplotted. It must be noted that the B08 best-fit can be reproduced when fit with the method described in B08. Specifically, as discussed in Section 2.6.1.2, the B08 fitting method does not fit for intrinsic scatter, but instead adds an additional 20% and 10% gaussian scatter to their M_{tot} and Y_{SZ} values, respectively. As with the M_{tot} uncertainty, the 10% uncertainty in Y_{SZ} is dominated by asphericity, the effect of which is approximated based on the measured Y_{SZ} uncertainty of Abell 370 [105]. The magnitude of this additional noise effectively de-weights the B08 mass values (i.e., adds intrinsic scatter in the mass direction), resulting in a steeper slope.

The BOXSZ analysis has defined intrinsic scatter to be the additional amount of Gaussian scatter that is required in the dependent variable to describe departure from a set of scaling relations applied to the independent variable. Uncertainty in the asphericity is a source of intrinsic scatter, and for that reason it was not explicitly accounted for in the statistical error estimation. It is reasonable to assume, that due to the fact that BOXSZ is an exceptional collection of some of the most massive clusters with median redshifts of $z = 0.42$, the intrinsic scatter and systematic uncertainty on f_{gas} for these clusters might be a bit larger. Many of these effects, however, such as asphericity and departures from hydrostatic equilibrium, are most likely correlated for the two variables. A full consideration of these factors is outside of the scope of the present analysis.

The importance of unaccounted levels of intrinsic scatter in M_{tot} and the possible mass dependence of f_{gas} is now explored. As f_{gas} is expected to asymptote at large M_{tot}, by dropping lowest mass clusters, one might observe something closer to self-similarity. Figure 4.12 demonstrates that the incorporation of an additional element of intrinsic scatter in
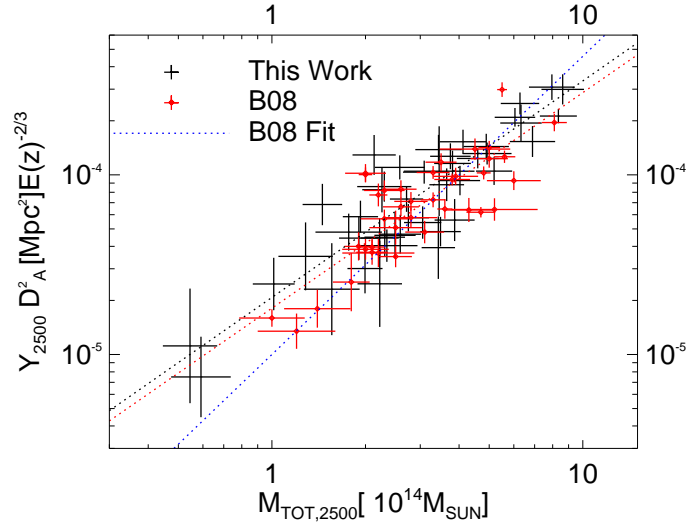
Figure 4.11 Comparison of the Bonamente et al. [37, B08] and the BOXSZ scaling relations. The red line is the best-fit to the B08 values of Y_{2500} and M_{2500} using the adopted fitting formalism for the BOXSZ study but not corrected for selection effects, which are negligible. This fit is quite different from the best-fit given in B08 (blue line) but is very similar to the best-fit BOXSZ scaling relation (black line). The difference in the two fitting methods can be explained by a net de-weighting of the B08 mass measurements with an additional gaussian scatter in M_{tot} to account for systematic uncertainties primarily associated with cluster asphericity.
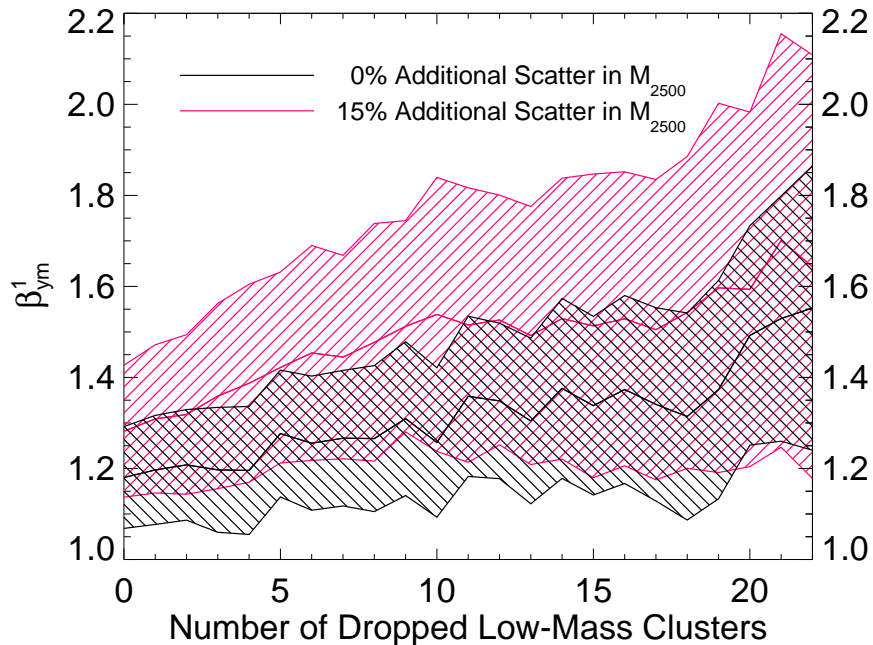
Figure 4.12 The effect that an additional amount of intrinsic scatter has when dropping the lowest mass clusters on the BOXSZ $\theta_{y|m}$ slope. The shaded bands indicate the 68.2-percentile confidence region.

the M_{tot} direction bumps the slope of the scaling relations up by approximately a standard deviation. Furthermore, by dropping more of the lowest mass clusters, the measured relation steepens. By including more intrinsic scatter in the M_{tot} direction and by removing clusters from the sample, however, also increases the error on the measurements making them less significant. With all of these effects taken into account, the entire trend is consistent with the original BOXSZ measured $\beta_1^{y|m}$ value, and by adding an additional amount of intrinsic scatter in the M_{tot} direction, the results become consistent with other observed $\theta_{y|m}$ measurements after removing only 5 clusters. The comparison between the present and the B08 work emphasizes the need for accurate systematic noise modeling.

A11 also measure scaling relations between Y_{SZ} measurements from the South Pole Telescope (SPT) and Y_X-derived M_{500} values using the V09 calibration. The sample consists of 15 SZE-flux selected clusters, with $0.29 < z < 1.08$, within the SPT 178 deg^2 survey. The nature of the SZE flux-limited selection of a deep (though relatively small) survey results in a less massive cluster selection than the BOXSZ sample—all but one of the A11 clusters lie below the BOXSZ median $M_{500} = 9.1 \times 10^{14} M_\odot$. A direct comparison is further hindered, considering the A11 analysis uses R_{500} instead of R_{2500}. A11 measure $\beta_1^{y|m} = 1.67 \pm 0.29$, slightly shallower than their X-ray mass proxy's measured $\beta_1^{y_x|m} = 1.79 \pm 0.15$, which is consistent with their measurement of $\beta_1^{y|y_x} = 0.90 \pm 0.17$ using a cylindrical Y_{SZ}, and is also consistent with the BOXSZ result of 0.85 ± 0.07. While this measurement is very small in itself, my intention is to point out that each group observes the same trend and this is an important factor when attempting to explain the physical origin of the BOXSZ $\beta_1^{y|m}$ deviation and this is a point that must be addressed with further investigation. Although A11 do not specifically measure $\theta_{y|m_{gas}}$, they do measure $\beta_{m_{gas}|t} = 1.79 \pm 0.51$, which again implies a shallower than self-similar $\theta_{t|m}$. A11 use the same LME method as the current analysis and they do not marginalize over uncertainties in statistical error of M_{tot} and Y_{SZ}. Furthermore, because V09 do not measure intrinsic scatter in their $\theta_{y_x|m}$ relation, there is no additional systematic uncertainty included in their M_{tot} estimation.

In contrast to the A11 sample, the P11 sample of the *Planck* Early Cluster Catalog has slightly more clusters (62) than and a mass range ($2 \times 10^{14} < M_{500} < 2 \times 10^{15} M_\odot$) similar to the BOXSZ sample. The P11 sample differs from BOXSZ, primarily because it is weighted

towards a much lower redshift: with 59 of the 62 clusters less than the median BOXSZ redshift. The recent scaling relations derived in Planck Collaboration et al. [227] contain an additional 9 confirmed clusters, but the overlap with the BOXSZ sample is the same as with P11—7 clusters. Because the results from this slightly expanded sample are very similar to P11, they will not be explicitly examined in this analysis. As in A11, P11 derive all cluster parameters within R_{500}, and M_{tot} is obtained from the Y_X proxy (specifically those derived in A10) and measure $\beta_1^{y|m} = 1.72 \pm 0.08$, which is close to the to the measured $\beta_1^{y_x|m} = 1.79$ of their adopted, A10, mass calibration. P11 further measure $\beta_1^{y|m_{gas}} = 1.36 \pm 0.07$, which are both consistent with the current analysis.

The measured BOXSZ $\beta_1^{y|m}$ slope is shallower than would be predicted from the adopted X-ray-mass calibration's derived $\beta_1^{y_x|m}$, indicating that mass calibration alone does not fully explain the shallowness of the $\beta_1^{y|m}$ measurement. The data indicate a mass-dependent scaling between Y_{SZ} and Y_X, with $\beta_1^{y|y_x} = 0.84 \pm 0.07$. This is consistent with the two analyses considered in this work, which have also performed a measurement of $\theta_{y|y_x}$. P11 measure 0.95±0.04, and A11 measure 0.90±0.17. Of note is the R12 re-analysis of the P11 data which measures a shallower $\beta_1^{y|y_x} = 0.917 \pm 0.039$ using the same data presented in P11. R12 also measure $\beta_1^{y|y_x}$ using a subsample of the P11 data and *Chandra* X-ray data obtained from V09 (instead of *Newton*-XMM X-ray data) and obtain a similar result: $\beta_1^{y|y_x} = 0.916 \pm 0.032$. The consistency of these results suggests that $\beta_1^{y|y_x}$ is slightly less than unity, likely indicating that mass-weighted temperature does indeed scale differently with cluster mass than emission-weighted temperature.

4.6.1 M_{tot} Rescaling

The similarities between the $\theta_{y|y_x}$ measurements at different integration apertures compared with the differences between $\theta_{y|m}$ measurements between different groups encourages a closer examination of the adopted M_{gas} mass proxy. While there is strong observational evidence that f_{gas} evolves with mass in groups and low-mass clusters (Vikhlinin et al. [278], Gonzalez et al. [102], Sun et al. [269]), measurements do not clearly indicate how f_{gas} evolves for more massive clusters—if at all (Allen et al. [6], Bonamente et al. [37], Zhang et al. [301], Mahdavi et al. [163]). A recent study by Mahdavi et al. [163] compares X-ray determined masses with

weak lensing masses, indicating that M_{gas} is indeed a lower scatter mass proxy than Y_X for clusters with $T_X > 3$ keV. At radii fixed to the weak lensing R_{500}, they measure a scatter of $15\% \pm 6\%$ uing M_{gas} as a mass proxy, and $23\% \pm 6\%$ using Y_X as a mass proxy .

Let us explore how the measured scaling relations change if we would have assumed f_{gas} to have a mass and redshift dependency. Rozo et al. [245] note that if the Pratt et al. [236] f_{gas} mass dependency and the [161] f_{gas} redshift dependency is used, the P11- and M10-measured M_{tot} values for clusters shared between the two analyses are consistent with each other. Inserting these values into Equation 2.30, derived using the Rozo et al. [245] methodology discussed in Section 2.6.3, yields:

$$f_{gas,P11}(M,z) = 0.13 \left(\frac{M_{tot}}{10^{15} M_\odot}\right)^{0.21} (1+z)^{0.66}, \tag{4.11}$$

$$b_{M10|P11} = \frac{M_{M10}}{M_{P11}} = \left(\frac{f_{gas,P11}(M_{tot},z)}{f_{gas,A08}}\right)^{1.67} = 1.31 \left(\frac{M_{tot}}{10^{15} M_\odot}\right)^{0.35} (1+z)^{1.10}. \tag{4.12}$$

Keep in mind that these values were calibrated using systems with much lower masses than the BOXSZ clusters, and adopting them requires a potentially invalid extrapolation.

When comparing the scaling relations, one must also take into account that a systematic difference in M_{tot} also shifts the R_Δ value, which therefore also systematically changes the aperture within which a given observable X is integrated. This effect is demonstrated in Figure 2.5. Let's assume that X scales self-similarly with R with $X \propto R^\epsilon$ at a specified R_Δ. Since $R_\Delta \propto M_\Delta^{1/3}$, the systematic difference in mass estimates, $b_{A|B}$, that will affect the measured observable X as $b_{A|B}^{\epsilon/3}$. R12 find that for an A10 universal pressure profile, $Y \propto R^{0.82}$ at R_{500} and thererefore the systematic difference in the Y_{SZ}-values would be:

$$b_{Y_{SZ}|P11} = b_{M10|P11}^{0.27}. \tag{4.13}$$

Using Equations 4.12 and 4.13, the effects of a systematic mass difference $b_{M10|P11}$ and $b_{Y_{SZ}|P11}$ will now be examined for the BOXSZ sample. As the redshift scaling does not dramatically affect the results, I only explore the effect of assuming that f_{gas} scales with M_{tot} and set the $(1+z)^{1.10}$ factor to unity. Keep in mind that R12 calculates these values at R_{500} and therefore the results are not precise and indicate the need for further study. Figure
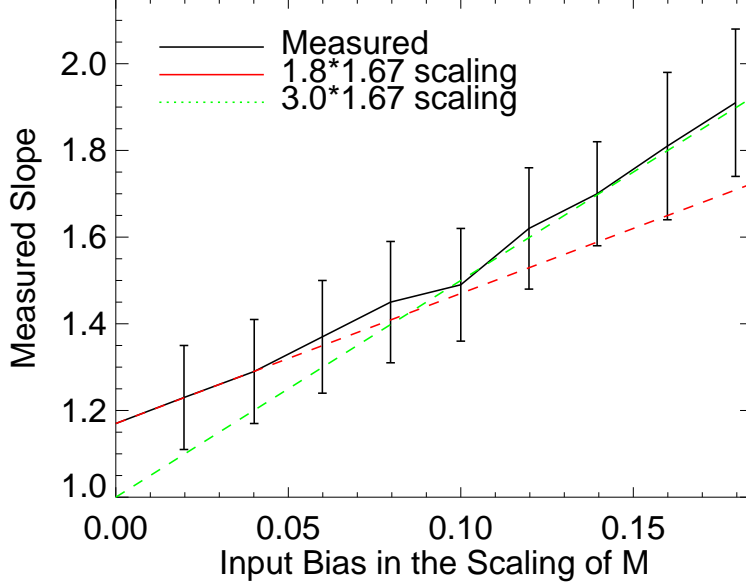
Figure 4.13 The measured $\beta_1^{y|m}$ slope as a function of the mass scaling of f_{gas}, α, where $f_{\text{gas}} \propto M_{tot}^\alpha$. The black lines indicate the measured $\beta_1^{y|m}$ and the uncertainty in their measurement. The red and green dashed lines are approximate fits to lower-levels and higher-levels of f_{gas} scaling with total cluster mass, respectively. In both cases, the slope steepens more than expected from the Rozo et al. [245] method alone.

4.13 demonstrates the effect that the assumption of a different f_{gas} scaling with M_{tot} has on the measured $\beta_1^{y|m}$ relation. The black symbols and lines indicate the slope measured as a function of the assumed scaling, α, where $f_{\text{gas}} = M_{tot}^\alpha$. One would naively expect a $(\beta_1^{y|m} - 0.25) \times 1.67$ scaling in $\beta_1^{y|m}$ with the assumed bias, according to R12, although the figure indicates a much steeper relation. This observation might be due to a combination of factors, for example, the decrease in the the dynamic range of the masses might possibly influence the measurement bias. A full exploration of the true measurement bias is beyond the scope of this thesis, but Figure 4.13 demonstrates how sensitive an application of this bias would be.

4.6.2 Comparison with Simulations

Several different groups have simulated cluster-observable scaling relations and the general consensus is that Y_{SZ} is a robust, low-scatter, self-similar, M_{tot} proxy across a wide variety of physical scenarios. A major impediment, however, in applying these results directly to the

Table 4.4. Summary of Simulated Scaling Relations Analyses. Part I.

Analysis/Code	Selected Scaling Relations			
Kravtsov[148]/ART	16 clusters ($M_{500} = [0.5, 13.0]\ 10^{14} M_\odot$)			
$\Delta = 500$	$M_{tot}|T_X$	$M_{tot}|M_g$	$M_{tot}|Y_X$	$M_{tot}|Y_{SZ}$
All z, all clusters, CSF ... β_1	1.521 ± 0.062	0.921 ± 0.023	0.581 ± 0.009	0.585 ± 0.010
σ	0.195	0.107	0.071	0.067
All z, relaxed, CSF .... β_1	1.533 ± 0.103	0.898 ± 0.051	0.579 ± 0.012	0.564 ± 0.014
σ	0.136	0.115	0.053	0.058
All z, unrelaxed, CSF .... β_1	1.553 ± 0.063	0.931 ± 0.029	0.589 ± 0.010	0.600 ± 0.010
σ	0.186	0.095	0.072	0.059
$z = 0$, all clusters, CSF... β_1	1.524 ± 0.070	0.917 ± 0.028	0.583 ± 0.010	0.584 ± 0.013
σ	0.219	0.090	0.064	0.075
$z = 0.6$, all clusters, CSF.. β_1	1.590 ± 0.086	0.871 ± 0.033	0.571 ± 0.016	0.577 ± 0.012
σ	0.157	0.077	0.075	0.051
Nagai[198]/ART	11 clusters ($M_{500} = [0.5, 13.0]\ 10^{14} M_\odot$)			
	$Y_{SZ}|T_X$	$Y_{SZ}|M_g$	$Y_{SZ}|M_{tot}$	
$\Delta = 2500$ GO............ β_1	2.50 ± 0.17	1.64 ± 0.07	1.68 ± 0.07	
σ	...	...	$\sim 0.10 - 0.15$	
$\Delta = 2500$ CSF .... β_1	2.73 ± 0.19	1.58 ± 0.05	1.77 ± 0.09	
σ	...	...	$\sim 0.10 - 0.15$	
$\Delta = 500$ GO .... β_1	2.45 ± 0.12	1.65 ± 0.08	1.66 ± 0.09	
σ	...	...	$\sim 0.10 - 0.15$	
$\Delta = 500$ CSF .... β_1	2.61 ± 0.17	1.60 ± 0.06	1.73 ± 0.08	
σ	...	...	$\sim 0.10 - 0.15$	

Note. — Simulated scaling relations from Kravtsov et al. [148] using the Eulerian N-body+gasdynamics adaptive mesh refinement ART code. They explore only one physical scenario with cooling and star formation (CSF), but they study the scaling relations at different redshifts and for relaxed and disturbed morphologies. Nagai et al. [198] use 11 of these clusters to study the dependence of the scaling relations with overdensity radius, specifically modelling a gravity-only (GO) scenario for comparison. They do not give specific intrinsic scatter measurements, but note that it is approximately 10-15% for all scenarios.

Table 4.5.   Summary of Simulated Scaling Relations Analyses. Part II.

Analysis/Code	Selected Scaling Relations		
Fabjan[87]/TreePM GADGET	140 clusters ($M_{500} = [0.3, 30] \ 10^{14} M_\odot$)		
$\Delta = 500$	$M_{tot}\vert T_{mw}$	$M_{tot}\vert M_g$	$M_{tot}\vert Y_X$
GO z=0 .... β_1	1.517 ± 0.012	0.981 ± 0.004	0.597 ± 0.003
σ	0.079	0.056	0.107
CSF z=0 .... β_1	1.615 ± 0.016	0.929 ± 0.003	0.591 ± 0.003
σ	0.069	0.042	0.084
GO z=0.50 .... β_1	1.534 ± 0.016	0.991 ± 0.004	0.604 ± 0.003
σ	0.087	0.047	0.111
CSF z=0.50 .... β_1	1.640 ± 0.017	0.929 ± 0.003	0.596 ± 0.003
σ	0.077	0.042	0.091
Fabjan[87]/TreePM GADGET	18 clusters ($M_{500} = [0.3, 20] \ 10^{14} M_\odot$)		
	$M_{tot}\vert T_{mw}$	$M_{tot}\vert M_g$	$M_{tot}\vert Y_X$
CSF+AGN z=0 .... β_1	1.730	0.81	0.54
Battaglia[19]modified GADGET-2	100s of clusters ($M_{500} = [0.8, 10] \ 10^{14} M_\odot$)		
$\Delta = 500$	$Y_{SZ}\vert M_{tot}$		
GO z=0 .... β_1	1.64 ± 0.03		
σ	0.097 ± 0.001		
CSF z=0 .... β_1	1.69 ± 0.03		
σ	0.107 ± 0.001		
AGN z=0 .... β_1	1.73 ± 0.03		
σ	0.130 ± 0.001		

Note. — Fabjan et al. [87] GADGET code simulations of scaling relations. Note that both M_g and Y_x are good mass proxies in gravity-only (GO) and cooling and star formation (CSF) scenarios. The CSF scenario also includes Type-II supernova feedback in the form of galactic winds. While the data for the smaller sample of extended physical simulations is limited mostly to the plots, I have included the numbers as presented in the text, where it is observed that $f_{gas} \propto 0.2$ in the AGN scenario. Battaglia et al. [19] not a similarly strong steepening of the $Y_{SZ} - M_{tot}$ slope with the inclusion of AGN feedback.

Table 4.6.   Summary of Simulated Scaling Relations Analyses. Part III.

Analysis/Code	Selected Scaling Relations		
Stanek [267] GADGET-2	5612 clusters ($M_{500} = \sim[0.3, 10]\ 10^{14} M_\odot$)		
$\Delta = 200$	$T_{mw}\vert M_{tot}$	$T_{sl}\vert M_{tot}$	$Y_{SZ}\vert M_{tot}$
GO z=0 ....β_1	0.650 ± 0.002	0.576 ± 0.005	1.651 ± 0.003
σ	0.102 ± 0.001	0.219 ± 0.002	0.123 ± 0.001
PH z=0 ....β_1	0.559 ± 0.002	0.576 ± 0.002	1.825 ± 0.003
σ	0.058 ± 0.002	0.069 ± 0.001	0.125 ± 0.002

Note. — Stanek et al. [267] scaling relations using the Millenium Gas Simulations (Hartley et al. [112].) In addition to the gravity-only (GO) scenario, clusters are simulated are pre-heated (PH) with an entropy boost at $z = 4$ to match empirical $L_x - T_x$ relations. Note how preheating reduces the intrinsic scatter in the temperature-mass relations and steepend the $Y_{SZ} - M_{tot}$ slope.

present analysis is that they have often been limited in total volume, and therefore include few, if any, extremely massive BOXSZ-like clusters. Kravtsov et al. [148, hereafter K06] were some of the first to include non-thermal physics (cooling and star formation, CSF) in hydrodynamic cluster simulations and measured f_{gas} to scale as $M_{500}^{0.2}$. The K06 results that are relevant to this thesis are presented in Table 4.4. All scenarios indicate a steeper-than-self-similar Y_{SZ} - M_{tot} slope, mostly driven by the mass dependency of f_{gas}. Nagai [197, hereafter N06], extend the analysis for 11 of the K06 clusters, focusing primarily on the Y_{SZ}-$\vert M_{tot}$, $Y_{SZ}\vert M_{gas}$, and $Y_{SZ}\vert T_{mw}$ scaling relations. They simulate both a gravity-only (GO) scenario, and one including CSF and the relevant results are also given in Table 4.4. Due to the small sample size, the error bars on the measured scaling relations are rather large, but indicate a steepening of the $Y_{SZ}\vert M_{tot}$ relation and a shallowing of the $Y_{SZ}\vert M_{gas}$ relation with respect to self-similarity. This effect is largest at $\Delta = 2500$.

Fabjan et al. [87, hereafter F11] simulate a cluster sample that is quite a bit larger and more massive than the N06 sample: 140 of the simulated clusters have M_{500} between approximately $0.3 \times 10^{14} M_\odot$ and $30 \times 10^{14} M_\odot$. F11 perform N-body simulations under several scenarios which can be generically lumped into three categories: GO, CSF, and CSF+AGN

feedback. In contrast to the K06 and N06 results, Y_{SZ} and M_{gas} mass proxies are robust to cooling and star formation, scaling self-similarly, for different redshifts. F11 simulated 18 clusters under a larger variety of different physical scenarios. F11 note that M_{gas} and T_X are dependent on physical processes, particularly AGN feedback, within a cluster. The presence of AGN feedback makes the $M_{tot}|M_{gas}$ scaling significantly shallower: from 1.0 to 0.8, and $M_{tot}|T_{mw}$ scaling relation steeper, from 1.5 to 1.73. Physically this relation results as AGN activity lowers f_{gas} by blowing out gas from the cluster core and heating it in the process. Interestingly, if one put these two relations together, one obtains a $T_{mw}|M_{gas}$ slope of 0.46—which implies $\beta_1^{y|m_{gas}} = 1.46$. These results are supported by Battaglia et al. [19, B12A], who simulate similar physical scenarios and have a similarly-sized cluster sample as F11. The B12 study differs from F11 as it emphasizes the radial-dependence of non-thermal pressure support. The relevant F11 and B12 results are given in Table 4.5.

Stanek et al. [267, hereafter S10] derive observable-mass relations using both a GO scenario, and a scenario in which the gas is preheated (PH) by adding a constant amount of entropy to the simulations at $z = 4$, in order to match $L_x - T_x$ observations at $z = 0$ [112]. The physics of their treatment is strikingly different from the CSF+AGN scenario, although they are able to replicate many of the simulation and observation results in a rather simple fashion. The S10 sample consists of over 4000 clusters for both scenarios—with approximately 10 halos above $M_{500} = 7 \times 10^{14}$ (approximately the median of the BOXSZ sample). The relevant S10 results are given in Table 4.6. S10 observe f_{gas} to scale quadratically with M_{tot} in their PH scenario as $\ln f_{\text{gas}} = s_{14} + \alpha_1 \ln M_{tot} + \alpha_2 \ln(M_{tot})^2$: with $\alpha_1 = 0.310 \pm 0.009$, $\alpha_2 = -0.661 \pm 0.0061$, and s_{14} a constant of proportionality. This relation approaches a constant value for clusters with masses representative of the BOXSZ sample. S10 measure PH $\beta_1^{y|m}$ of 1.825 ± 0.003 to be significantly steeper than self-similar.

S10 also measure both T_{mw} and the spectroscopic-like temperature:

$$T_{sl} = \frac{\int n^2 T^{1/4} dV}{\int n^2 T^{-3/4} dV}, \tag{4.14}$$

as originally defined in Section 2.2.2, which was proposed by Mazzotta et al. [179] for simulations to accurately predict X-ray spectroscopic temperature measurements fit to a single

projected temperature profile. Pre-heating effectively increases the sound speed and lowers the Mach number of the infalling gas, smoothing the internal structure of galaxy clusters [283]. Therefore, in contrast to the F11 results, the S10 T_{sl} is shown to be very sensitive to gas physics. Only T_{mw} in the GO scenario is measured to be consistent with self-similarity. $T_{sl} \sim 0.576 \pm 0.05$ in both scenarios, and $T_{mw} = 0.559 \pm 0.002$ in the PH scenario. Again, if one combines this with an evolving f_{gas}, one obtains a result that would be consistent with the M10 results.

Finally, we will consider the Krause et al. [144, hereafter K12] simulations, which specifically focus on measuring merger-induced deviations from self-similar $Y_{SZ}|M_{tot}$ relation. The K12 sample generally includes non-thermal physics and contains ~ 100 clusters with about 10 clusters distributed evenly in logarithmic space from $10^{13} \lesssim M_{200} \lesssim 10^{15} M_\odot$. K12 notice a merger-induced shallowing of their $Y_{SZ}|M_{tot}$ scaling with $\beta_1^{y|m} = 1.556 \pm 0.014$. This shallowing is attributed to merger-induced events with 50% of the outliers in their sample, undergoing a major merger in the last Gigayear. The slope, again, returns to a self-similar-consistent value, $\beta_1^{y|m} = 1.637 \pm 0.027$, when restricted to clusters above $2 \times 10^{14} M_\odot$, which indicate to be less susceptible to merger effects. Based on these results, merger activity probably does not have much of an effect on the BOXSZ Y_{SZ} measurements.

These simulations, furthermore, make interesting predictions in regards to the intrinsic scatter of cluster observables with mass. The general consensus is that Y_X and Y_{SZ} are low-scatter mass proxies, but there is ambiguity as to the degree to which f_{gas} scales with M_{tot} for different mass ranges and different overdensities. F11 conclude that Y_X and M_{gas} are both low-scatter mass proxies. While they measure Y_X to be less sensitive to cluster physics, they note that M_{gas} has less intrinsic scatter under all physical scenarios, $\sim$4-9%, compared with the measured $Y_X|M_{tot}$ scatter of $\sim$6-12%. S10 measure scatter in T_{sl} to be approximately a factor of three larger, 0.219$\pm$0.002, in the GO compared with the PH scenario. This confirms their observation that pre-heating makes cluster properties more regular. S10 conclude Y_{SZ} to be a robust $\sim 12 \pm 2\%$ scatter mass-proxy for both of the simulated astrophysical scenarios. Similarly, B12 note that AGN feedback and triaxiality bump the intrinsic scatter of the $Y_{SZ}|M_{tot}$ relation from a fiducial value of 11% to 13% at z=0, and 15% at z=1. Further of interest is that while S10 and F11 find the scatter in both M_{gas}, Y_{SZ}, and Y_X to be well-

approximated as log-normal, B12 finds that Y_{SZ} scatter is best approximated with a normal distribution. Furthermore, K12 note a positive skewness to the Y_{SZ} intrinsic scatter which they ascribe to projection effects boosting the Y_{SZ} signal with respect to mass. This effect, again, vanishes completely for the more massive, BOXSZ-like clusters of their sample.

In summary, the BOXSZ-measured $\theta_{y|m}$ scaling relations do not appear to be consistent with simulations. They could, however, be explained if we assume f_{gas} to scale with M_{tot}, where a shallower than self-similar $T_{mw} - M_{tot}$ slope and a steeper than self-similar $M_{gas}|M_{tot}$ slope, particularly within R_{2500}, conspire together to make the $\theta_{y|m}$ relation shallower, where M_{gas} is used as a proxy for M_{tot}. This effect could be partially alleviated by dropping the lowest-mass clusters of the sample. Another explanation might be that the intrinsic scatter of the $M_{tot}|M_{gas}$ relation is larger than previously estimated. To resolve these questions more observational work calibrating the intrinsic scatter of the $M_{tot}|M_{gas}$ relation must be performed for a larger sample of massive clusters using different analysis techniques so that we can determine the correct simulation scenario.

4.6.3   Cosmological Implications

If the scaling relations for extremely massive clusters do indeed depart from self-similarity, this will significantly affect the inferred cosmology from cluster observations. New results from the *Planck* Collaboration indicate tension between σ_8 measurements using the primary CMB, $\sigma_8 = 0.834 \pm 0.027$,[226, hereafter P13CMB], and σ_8 measured using mass measurements of SZE-detected cluster counts, $\sigma_8 = 0.77 \pm 0.02$,[227, hereafter P13SZE]—with several times fewer clusters being detected than predicted. Figure 4.14 compares the *Planck* SZE-detected cluster counts compared with those predicted from the *Planck* primary CMB measurements. As the P13SZE sample is a highly massive sample with a large survey area, the scaling relations should be sensitive to similar biases as the BOXSZ sample. Using the BOXSZ $\theta_{y|m}$ would then imply that P13SZE isn't measuring *fewer* clusters than expected for a given mass—but that a given cluster mass simply produces less SZE signal. The effect of a systematic under-estimate of the mass vs. observable relation is plotted on the right-hand side of Figure 4.15. These results, from Vikhlinin et al. [280], demonstrate that boosting the normalization of the mass vs. observable relation upwards by 9% shifts the
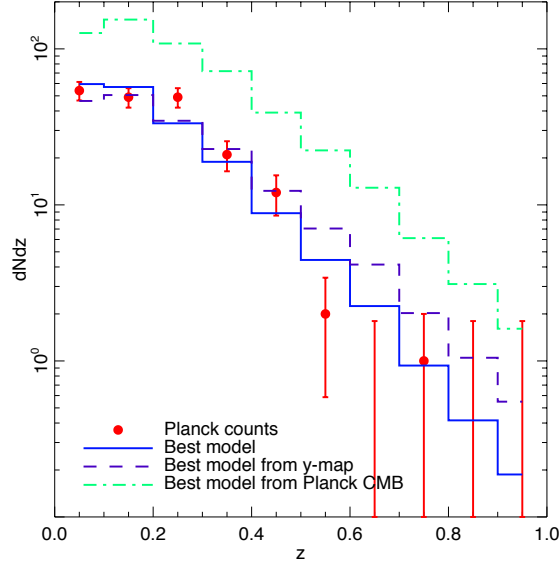
Figure 4.14 Difference between the Planck Collaboration et al. [227] measured cluster counts (red points with error bars) and the predicted Planck Collaboration et al. [226] cluster counts based on CMB measurements (green dashed line). The solid blue line represents the best model prediction while the dashed purple line is estimated from the *Planck* SZ power spectrum. More detailed information is given in Planck Collaboration et al. [226], from which the figure was taken.

σ_8 value upwards by approximately 0.025. Assuming the discrepancy between the CMB and SZE cluster σ_8 measurements is due to mass bias, P13 find that this would imply an overall mass bias of 45%—which is precisely the bias that R13 measure between the M10 and P11 samples for $z > 0.13$.

While highly suggestive, a simple swap of mass proxy is not enough to explain the discrepancy as cluster-based cosmological results using these different mass proxies vary. Vikhlinin et al. [280], for example, measure $\sigma_8 = 0.813 \pm 0.012$ using *Chandra*-X-ray measurements with masses also derived from the Y_X-M_{tot} mass proxy. This is comparable to the M10 cluster-based cosmological analysis (one of the few to have used the M_{gas}-M_{tot} mass proxy) who measure $\sigma_8 = 0.82 \pm 0.05$. Benson et al. [25], however, measure $\sigma_8 = 0.773 \pm 0.088$, which is closer to the P13SZE results, using SZE-derived masses also calibrated with the Y_X-M_{tot} mass proxy.

One must keep in mind that σ_8 and Ω_M constraints using cluster number counts are degenerate, and one can only constrain the product: $\sigma_8 \Omega_M^{\sim 0.3}$. Accounting for this degeneracy,

116
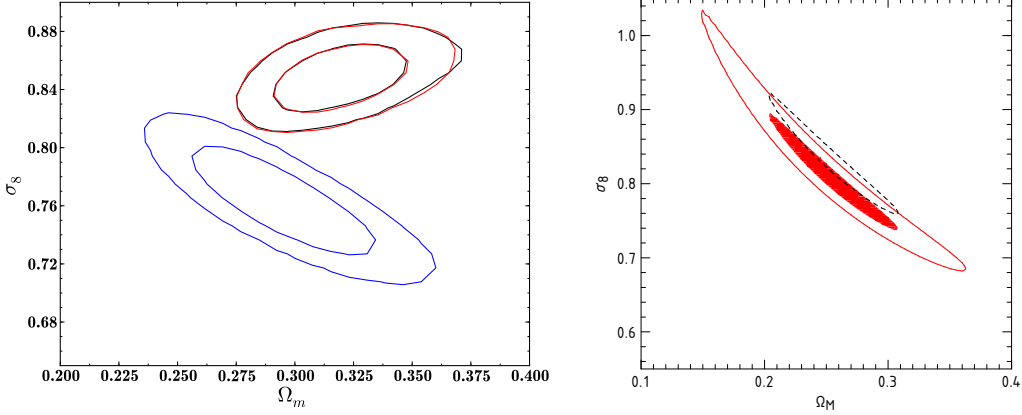
Figure 4.15 Left: The Planck Collaboration et al. [226] Ω_m-σ_8 likelihood measured using the *Planck*-CMB anisotropy spectrum only (red), the *Planck* SZE cluster count mass esimates together with BAO and BBN data (blue), and the combined *Planck* CMB and SZE analysis, allowing the mass bias to float (black). The combined CMB+SZE analysis fits for a positive bias in the cluster mass of approximately 40%. Figure from Planck Collaboration et al. [227]. Right: The measured likelihood of the Ω_m-σ_8 degeneracy as measured using X-ray cluster count mass estimates in Vikhlinin et al. [280] assuming a flat ΛCDM model. The dashed contour shows the effect of adding boosting the mass vs. observable relation by the estimated systematic error of 9%. Figure from Vikhlinin et al. [280]. The two sets of contours in both plots trace the 68% and 95% confidence region.

all of the cluster cosmology analyses measure consistent values for the degenerate Ω_M-σ_8 parameter. Now considering the Ω_M measurements, we reference the WMAP-9 measurement of $\Omega_M = 0.279 \pm 0.025$, and the WMAP-9+BAO+SNe+SZE (ACT+SPT) measurement of $\Omega_M = 0.2865^{+0.0096}_{-0.0095}$. This is comparable with the P13SZE measurement of $\Omega_M = 0.29 \pm 0.02$ whereas P13CMB measure one of the higher values of $\Omega_M = 0.315 \pm 0.017$. The *Planck* $\sigma_8\Omega_M^{0.3}$ covariance for the P13CMB and P13SZE results is plotted in Figure 4.15. In contrast, M10 measure one of the lowest $\Omega_M = 0.23 \pm 0.04$. Clearly, these various cosmological results vary in more complex ways than can be explained by a simple scaling relation, and the possible explanation for this deviation is an exciting new topic for future study.

4.7 Future Scaling Relations Work

In this work, I have presented measurements of the integrated Sunyaev-Zel'dovich effect signal and studied how it scales with X-Ray determined cluster masses. I have sought to account for many sources of bias within the limits of the *Bolocam* SZE data. With a

proper exploration of the systematics, there is the possibilty that Y_{SZ} can be constrained within R_{500}, and this would give insight into the radial dependence of the observed deviation from self-similarity in the $\theta_{y|m}$ relations. Furthermore, it is interesting to explore the mass calibration in itself. To this end, our work with the CLASH collaboration gives us access to high quality weak- and strong-lensing measurements, with which we can calibrate the X-ray data.

Another line of investigation that is currently in the works (mostly led by Seth Siegel and Andisheh Mahdavi) is performing joint, multi-wavelength parametric deprojections. This has the advantage over independent wavelength analyses in that it preserves correlations between the different wavelength data sets.

In the future, we can also expect the quality of of the SZE data to improve. To this end, the Multiwavelength Submillimeter Inductance Camera (MUSIC), which is currently undergoing commissioning at the CSO, is a welcome technological step forward (Golwala et al. [101]). The camera has a larger focal plane than *Bolocam*, and it is simultaneously sensitive to four different wavelengths. This would allow better atmospheric noise removal, a better constraint of the large-scale Y_{SZ} signal, and better constraints of the non-thermal kinetic SZE signal.

Chapter 5

Other Recent *Bolocam* Results

In addition to leading the scaling relation analysis in Chapter 4, I contributed to a range of other results using the *Bolocam* SZE images. Many of these studies deserve special attention, since they form the framework for research in the near future. What has made a particularly strong impression on me is how much individual clusters can teach us about astrophysics and cosmology.

5.1   SZE Pressure Profiles

The limited ability for most SZE data to constrain either large- or small-scale cluster properties implies that pressure models must then be employed to fully characterize this signal. One of the most widely adopted pressure models, discussed in Section 2.2.1, is the generalized NFW (GNFW) model (Nagai et al. [198]) using the Arnaud et al. [15, A10] measured GNFW parameters. The A10 model is employed as the default model in the recent *Planck* SZE analyses, but it is not ideal, since it is X-ray-derived within R_{500} and simulation-derived beyond. With recent advances in the quality of SZE data, several groups are starting to constrain SZE pressure profiles beyond R_{500}. *Planck* is able to constrain the pressure profiles for low-redshift clusters in their sample, and their collaboration has recently published pressure profile measurements for both an individual case study of the Coma cluster [225] as well as for a large sample of 62 nearby massive clusters from the first 14 months of data [230]. In both cases, the *Planck* data show significantly excess pressure ($\gtrsim$ 2-σ) in the region from R_{500} to $\gtrsim 3{\times}R_{500}$ compared with simulations. Similar measurements are also possible us-
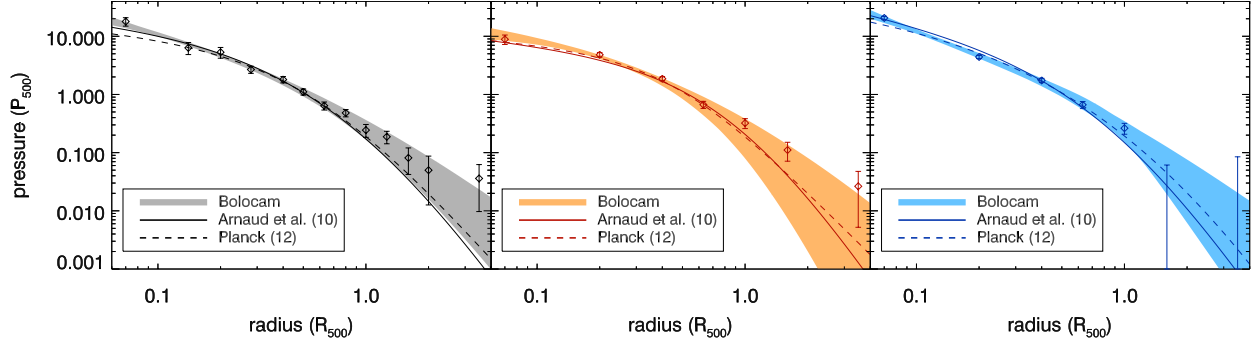
Figure 5.1 Joint GNFW fits, with four free parameters, to the BOXSZ-measured pressure maps. From left to right: full, disturbed, and cool-core cluster sample pressure profile measurements with the shaded 1-σ confidence regions of the fits to the data. These profiles are compared with the Arnaud et al. [15] and the Planck Collaboration et al. [230] best-fit GNFW models, which are depicted with solid and dashed lines, respectively. As the Planck Collaboration et al. [230] does not explicitly fit a disturbed sample, the non-cool-core best fit is given in the center plot. Figure taken from Sayers et al. [256].

ing *Bolocam* SZE data, and Sayers et al. [256] have jointly fit GNFW profiles to the entire BOXSZ cluster sample, and also to cool-core and disturbed cluster sub-samples. The results of this analysis are shown in Figure 5.1. While the BOXSZ pressure profile is systematically higher than either the A10 or the *Planck* measured pressure profiles, all three measurements are consistent with each other within 1-σ. If this excess holds under further scrutiny, this would have important implications for cluster cosmological analyses, which very often rely on these models to model large-scale modes that are often filtered by either a telescope's PSF or in the process of removing astronomical and atmospheric noise from the data.

5.2   Abell 1835: A Case Study in Cluster Triaxiality

An exciting new direction that we hope to explore more intensely in the near future is to constrain galaxy cluster halos in three spatial dimensions using a joint, multi-observational approach. This type of analysis leverages the assets of each observational probe: lensing for the overall mass, X-ray for the gas in the cluster core, and SZE for the gas in the cluster outskirts. Morandi et al. [191] perform a joint X-ray, strong lensing, and SZE analysis of the galaxy cluster Abell 1835. The lensing data is used to construct the projected surface mass distribution, Σ, and the gas data is used to constrain the 3D density and temperature

120

properties of the cluster. Figure 5.2 shows the observed data points together with the projected best-fit model. As can be seen, the SZE data is extremely important to constrain the cluster properties beyond 1 Mpc. One should keep in mind that had weak-lensing data been available, this would also have extended beyond 1 Mpc. The lensing and gas data are linked with a generalized HSE equation that includes a non-thermal component, which, motivated by the simulation results of Shaw et al. [259], is modeled to scale as a power law with radius:

$$\frac{P_{nt}}{P_{tot}} = \xi \left(\frac{R}{R_{200}}\right)^n,$$ (5.1)

where ξ and n are both free parameters constrained in the joint cluster fitting. The final Bayesian fit yields a measurement of $n = 0.77 \pm 0.21$, in agreement with the results from Shaw et al. [259] of $n = 0.80 \pm 0.25$. Hereby, we are the first to constrain the non-thermal pressure support out to the virial radius observationally. The measured normalization, $\xi = 0.177 \pm 0.065$, is approximately 2-σ less than that found in Shaw et al. [259]. The 3D mass profile constrains the minor-to-major axis ratio to be 0.59 ± 0.05 and the intermediate-to-major axis ratio to be 0.71 ± 0.08, with the major axis inclined to the line of sight at 18.3 ± 5.2 degrees. As cluster asphericity and non-thermal pressure support are extremely important for understanding cluster physics, this type of analysis is being extended to a larger sample of galaxy clusters by a member of the *Bolocam* analysis team, Seth Siegel, and our collaborator, Andisheh Mahdavi, using the Joint Analysis for Cluster Observations (JACO) software.[1]

5.3 MACSJ 0717.5: A Case Study of the Kinetic SZE

MACSJ 0717.5 is the most massive and, thus far, the most interesting cluster in the BOXSZ sample. It has the largest known Einstein radius of $\theta_e \approx 55''$[304]. Ma et al. [162] perform a multiwavelength X-ray and optical analysis of the cluster and identify four distinct clusters in a triple merger system, which are identified using the letters A-D in Figure 5.3. In particular, Ma et al. [162] measure system A to have an exceptionally high line-of-sight velocity of 3600^{+252}_{-242}km/s. Mroczkowski et al. [194] perform a joint X-ray/SZE analysis of the MACSJ 0717.5 cluster using *Chandra* X-ray data, MUSTANG 90 GHz data, and *Bolocam*

[1] `http://sfstar.sfsu.edu/cccp/` Mahdavi et al. [164].
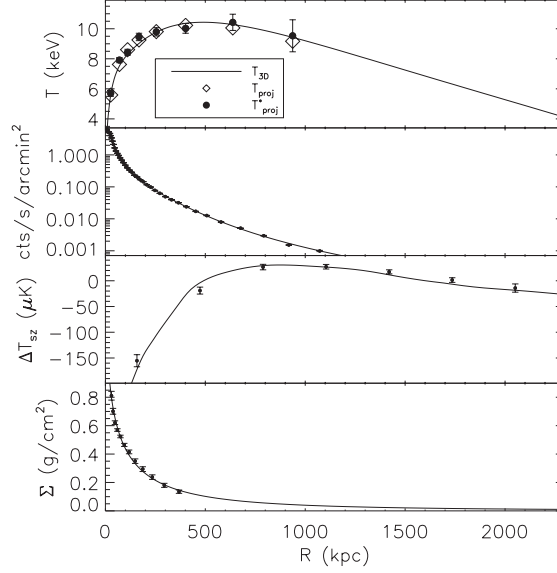
Figure 5.2 From top to bottom: Radially-averaged T_X, X-ray surface-brightness, ΔT_{sz}, and strong-lensing derived surface mass profiles of joint 3-dimensional fits (solid lines) to observational data (dots with error bars) of Abell 1835. The projected theoretical temperature (open diamonds) is also given in the upper plot. ΔT_{sz} is y expressed in units of temperature and is presented convolved with the pipeline transfer function. Figure from Morandi et al. [191].

data at both 140 GHz and 268 GHz. The 90 GHz, 140 GHz, and 268 GHz SZE data have resolutions of $13''$, $58''$, and $31''$, respectively.

Temperature and electron density maps measured with the *Chandra* X-ray data are used to construct pseudo-Y pressure profiles. The SZE data is plotted in Figure 5.3, together with the pseudo-Y contours smoothed to the particular resolution of the SZE observation. One can see how the SZE decrement is boosted at 140 GHz and suppressed at 268 GHz, as would be expected due to the predicted kinetic SZE effect. The observed spectral dependence of the SZE signal is depicted in Figure 5.4. The magenta lines depict the best-fit level of the kinetic SZE signal to the *Bolocam* 140GHz and 268 GHz data. For the B subcluster, the spectral SZE fit which includes a kinetic component, is preferred by slightly over 2-σ. Recently, the *Bolocam* collaboration has obtained more observational data at 268 GHz, which is sensitive enough to confirm or to rule out the kinetic contribution to the SZE signal.
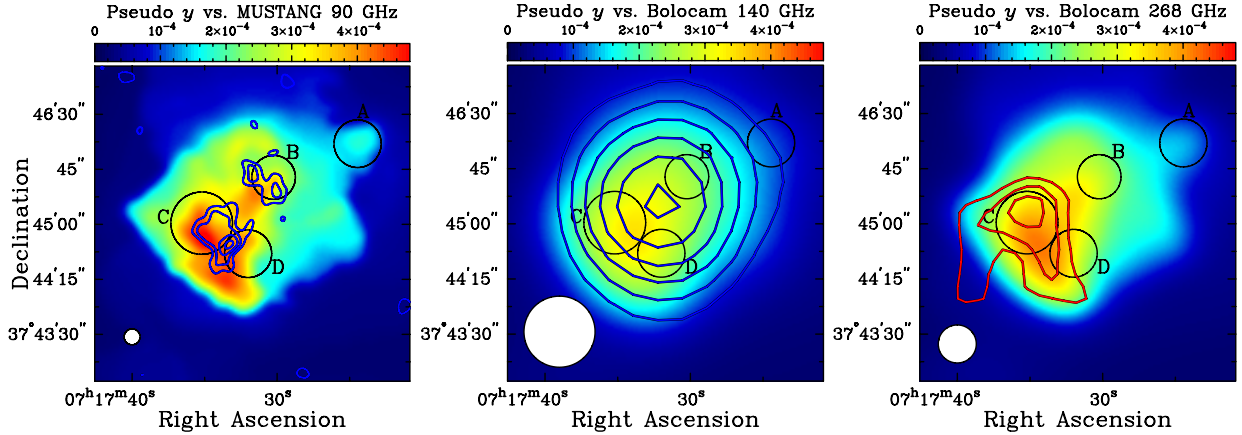
Figure 5.3 Pseudo-Compton Y maps constructed from *Chandra* X-ray data, smoothed to the resolution of the particular SZE observation depicted. The circles labelled as A through D are the four sub-halos identified in Ma et al. [162]. Left: 3-σ, 4-σ, 5-σ, and 6-σ confidence contours of the 90 GHz MUSTANG data. Middle: 5-σ, 10-σ, 15-σ, 20-σ, and 25-σ confidence contours of the *Bolocam* 140 GHz data. Right: 3-σ, 4-σ, and 5-σ confidence contours of the *Bolocam* 268 GHz data. Figure from Mroczkowski et al. [194], which includes more information about the employed smoothing and transfer functions of the data in these figures.
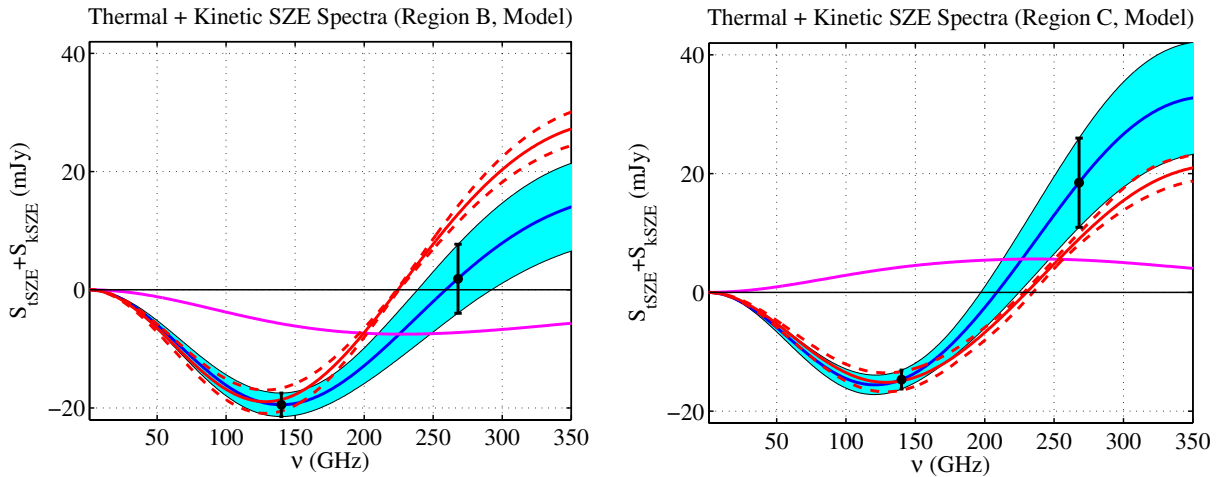
Figure 5.4 Left: 1-σ confidence contours of the best-fit SZE spectrum to the *Bolocam* data (black points with error bars), both accounting for (cyan) and neglecting (red) the kinetic SZE effect for the B subhalos. Magenta: The best-fit kinetic SZE contribution. The likelihood of the data in this region is $< 2.1\%$ for a cluster component velocity less than zero. Right: Similar to the left-hand figure, but for region C, the likelihood of the data in this region is $< 15.7\%$ for a cluster component velocity greater than zero. All flux densities are calculated using parametric fits directly to the data. Figure from Mroczkowski et al. [194], which includes more information, including non-parametric SZE flux density estimates.
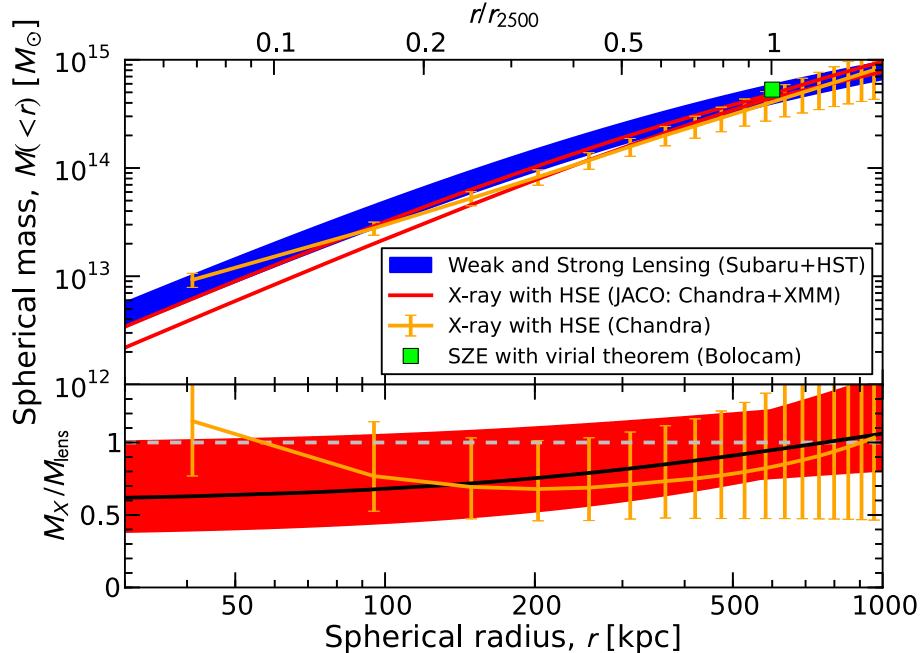
Figure 5.5 Top Panel: Total mass profiles derived for MACSJ 1206.2 using various observational probes. Blue represents the joint weak- (Subaru) and strong- (HST) lensing measurement, with the shading indicating the 1-σ confidence region. The red lines contain the 1-σ confidence region of the best-fit X-ray mass profile, using the JACO software and combining both *Chandra* and *XMM-Newton* observations. The orange line uses only *Chandra* data and assumes an A10 pressure profile. The green square represents the *Bolocam* SZE-only mass constraint on R_{2500} and is in good agreement with the data. Bottom Panel: the difference between the X-ray and lensing mass profiles for both X-ray fitting methods. As can be seen, the X-ray systematically under-estimates the lensing mass. Figure from Umetsu et al. [277].

5.4 Multiwavelength Mass Calibration

Umetsu et al. [277, hereafter U12] and [180, hereafter M13] perform an in-depth cross-calibration of mass profile measurements using strong- and weak-lensing, X-ray, and SZE observational probes for the galaxy clusters MACSJ 1206.2 and MACSJ 01717.5, respectively. The *Bolocam*-measured SZE mass of MASCJ 1206.2 at R_{2500} is consistent with the lensing and X-ray masses. In U12, we identify large-scale structure running from the North-West to the South-East region of MACSJ 1206.2 that, when removed, results in a very regular NFW mass profile. After removing the kinetic SZE contribution in MACSJ 0717.5 for the M13 analysis, we measure an SZE mass profile within 1Mpc/h, which is consistent with X-ray. Both gas mass measurements are below the lensing mass and suggest deviations from HSE.
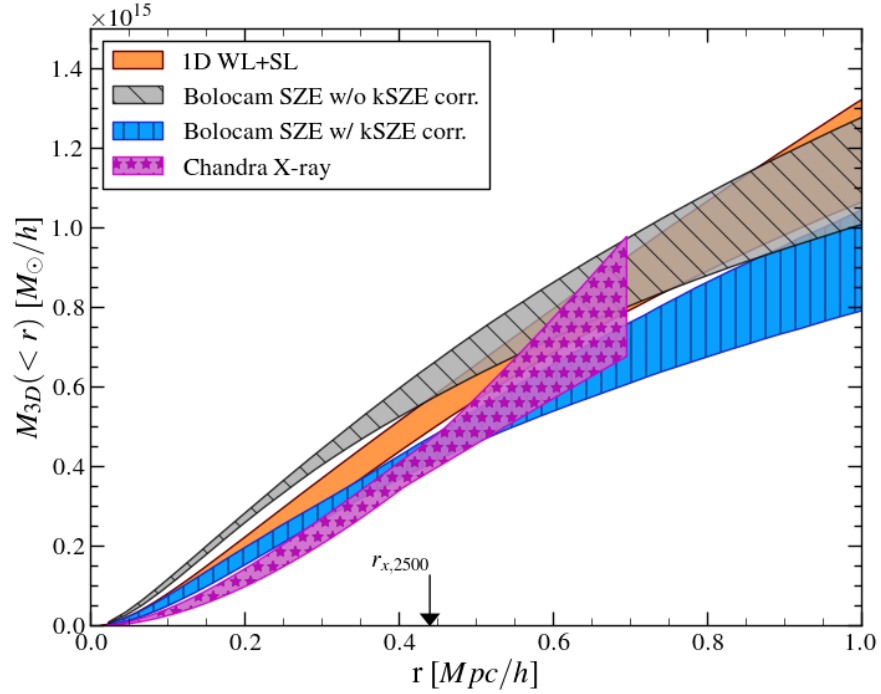
Figure 5.6 Total mass profiles derived for MACSJ 0717.5 using various observational probes. (Orange) Best-fit weak- and strong-lensing NFW profile. (Purple) *Chandra*-only mass profile estimate. (Gray and Blue) *Bolocam* SZE mass profile with and without correcting the kinetic SZE effect, respectively. The X-ray and the SZE data are largely consistent with each other and systematically lower than the lensing profile. The fact that the non-kinetic SZE corrected *Bolocam* mass profiles agree with the lensing data is purely a coincidence. Figure from Medezinski et al. [180].

Appendix A

Galaxy Cluster Catalogs

Understanding the specifics of a particular cluster catalog aids in understanding the characteristics of the clusters that they include. Some cluster catalogs have a well-defined cluster selection process which allows for analytical modeling of selection function effects. For obvious reasons, the first galaxy cluster surveys were compiled using optical observations. However, after the X-ray ROSAT All-Sky Survey (RASS) catalog became available, which includes many clusters at larger redshifts, X-ray has generally provided the basis for many of the current cluster catalogs of all wavelengths.

A.1   Optical Catalogs: Abell, Zwicky, and SDSS

Optically-selected galaxy cluster catalog members generally lie at lower-redshifts and have larger angular extents than their X-ray counterparts. George Abell [1] compiled the first comprehensive catalog of galaxy clusters in 1958 while still a graduate student at Caltech. He personally examined photographic plates taken with the Palomar Sky Survey to identify clusters for his catalog. The original 1958 work contains 2,712 galaxy clusters, and this was extended in 1989 to include the Southern sky, yielding a total of 4,073 galaxy clusters [2]. The Abell catalog has four main selection criteria: richness ($\sim$30 or more member galaxies must be within a specfic magnitude range), compactness ($\sim$50 or more members must be within approximately $1.5h^{-1}$Mpc, expressed in units of the modern-day physical distance parameterization), redshift ($0.02 < z < 0.20$), and finally, clusters should be sufficiently distant from the galactic plane to minimize contamination. Fritz Zwicky was also from

Caltech and also compiled a galaxy cluster catalog between 1961 and 1968 from the Palomar Sky Survey [308]. This catalog contains a total of 9,134 galaxy clusters. As Abell's catalog is more complete at the redshifts and luminosities of interest for cluster cosmology, it is generally favored over Zwicky's catalog.

The Sloan Digital Sky Survey (SDSS) is a more recent optical survey and has been surveying the sky since 2000. The camera is a 120 Megapixel CCD camera with 1.5 deg^2 field of view, and it is mounted on a 2.5m telescope at Apache Point Observatory in New Mexico. It observes in five temporally alternating color bands ($g', r', i', u',$ and z'), spanning from optical to infrared. The instrument has undergone two major upgrades, and the sky surveys are therefore split into three main catagories: SDSS-I (2000-2005), SDSS-II (2005-2008), and SDSS-III (2008-2014+).

The maxBCG catalog (Koester et al. [142]) uses the initial SDSS-I data to identify 13,823 galaxy clusters between $0.1 < z < 0.3$ in 7500 deg^2 of the sky using the red-sequence technique (Gladders & Yee [99]) and a likelihood function that includes the color and magnitude properties of a typical brightest cluster galaxy (BCG). The GMBCG cluster catalog (Hao et al. [111]) builds upon the MaxBCG catalog and identifies 55,424 galaxy clusters using the red-sequence technique between $0.1 < z < 0.55$ in the SDSS-II data release. The GMBBCG catalog covers 8240 deg^2 of the sky and is considered to be volume-limited out to $z = 0.4$.

Looking toward the future, the Dark Enery Survey (DES) will map 5000 deg^2 of the southern sky using five bandpass filters ranging from the visible to infrared (g', r', i', z', Y). The camera is a 520 Megapixel CCD camera with a 3 deg^2 field of view. The camera is mounted and operational on the Blanco 4m telescope in Chile, and the formal survey is expected to start in the Fall of 2013. DES expects to identify more than 20,000 clusters out to $z \gtrsim 1$ using the red sequencing technique (Sánchez & DES Collaboration [250], Flaugher & DES Collaboration [92]).

A.2 X-ray Catalogs: RASS, MACS, and MCXC

The ROSAT All-Sky Survey (RASS) is special, because it is the only all-sky X-ray survey to have ever been conducted and it is the basis of many other galaxy cluster catalogs. The

ROSAT satellite was a joint German, British, and American mission, which launched in 1990 and observed for over eight years. The instrument is sensitive to energies between 0.1 and 2.4 keV, and clusters identified in this catalog are denoted with RXJ (ROSAT, X-ray, and Julian).

Upon completion of the X-ray sky survey, several efforts were undertaken to identify galaxy clusters in the survey. The Brightest Cluster Sample, including its extension (eBCS, Ebeling et al. [73, 72]), contains over 300 confirmed galaxy clusters observed at declinations $> 0°$ and galactic lattitudes of $|b| > 20°$. It is estimated to be approximately 50% complete above $\sim 2.9 \times 10^{-12}$erg/s/cm^2(0.1 − 2.4keV) and 90% complete above $\sim 4.4 \times 10^{-12}$erg/s/cm^2(0.1 − 2.4keV). The ROSAT-ESO Flux Limited X-Ray Galaxy Cluster Survey (REFLEX)(Böhringer et al. [36]), can be considered, in a sense, the southern counterpart of BCS with slightly different selection criteria. REFLEX covers 4.24 steradians of the southern sky and includes 447 galaxy clusters down to a flux limit of 3×10^{12}erg/s/cm^2 (0.1 − 2.5keV). The sample includes X-ray properties and spectroscopic redshift information and is described to be more than 90% complete.

The Massive Cluster Survey (MACS) builds off of the RASS and BCS catalogs, and the selection methodology for this catalog is given in Ebeling et al. [74]. All clusters are observable from Mauna Kea ($-40° > \delta > 80°$), and the initial cuts are based on X-ray flux measurements greater than 1×10^{-12}erg/s/cm^2 between 0.1-2.4 keV, and an X-ray hardness ratio. Of the $\sim$5000 sources that remain, the final list of over 100 clusters is obtained through a rigorous vetting process, which includes visual inspection and follow-up spectroscopic observation. As of this writing, the only subsamples of the MACS catalog that have been published are the high-redshift sample (MACS-DIST), which consists of 12 clusters above $z > 0.5$, Ebeling et al. [71], and the high-flux ratio sample (MACS-BRIGHT), which consists of 34 clusters with nominal X-ray fluxes in excess of 2×10^{-12}erg/s/cm^2(0.1 − 2.4keV)(Ebeling et al. [75]). These samples, including the eBCS sample, are plotted in Figure A.1.

The Meta-Catalog of X-Ray detected Clusters (MCXC) [221] arose in light of the various disjoint X-ray catalogs and the need for a large of X-ray detected cluster sample for the upcoming *Planck* satellite mission as possible. 1743 clusters were obtained by combining all
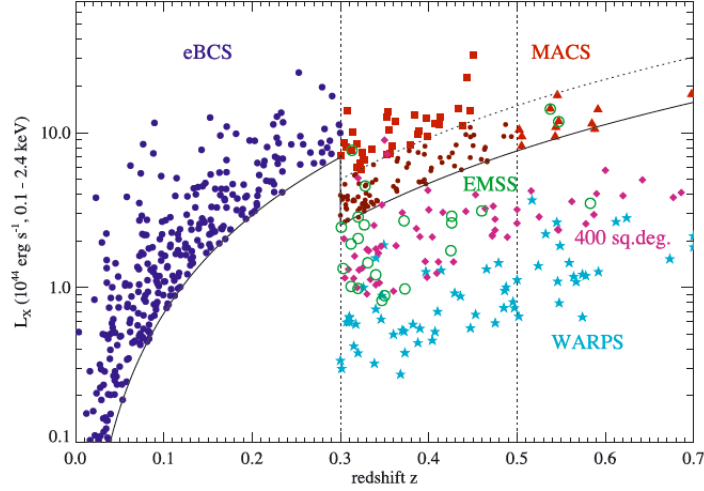
Figure A.1 The L_x-z distribution of of the eBCS (blue) and MACS (red) samples. Red squares and red triangles indicate the MACS-BRIGHT and MACS-DIST samples, respectively. EMSS (Gioia & Luppino [98]), WARPS (Perlman et al. [216]), and the 400 Square Degree (Burenin et al. [46]) project are serendipous surveys (clusters obtained from pointed observations), and therefore they are less complete and have lower flux limits than the complete flux-limited samples, such as the MACS cluster sample. Figure taken from Ebeling et al. [75].

publicly available catalogs based on the ROSAT All Sky Survey-based (NORAS, REFLEX, BCS, SGP, NEP, MACS, and CIZA) cluster catalogs, and also serendipitious (160SD, 400SD, SHARC, WARPS, and EMSS) cluster catalogs. Each cluster has a redshift and an estimated L_{500} $(0.1-2.4\text{keV})$ and M_{500} value. M_{500} values are obtained either directly from Maughan et al. [177] for the MACS catalog, or indirectly by inserting the L_{500} value into the Arnaud et al. [15] measured M-L relationship. In the case where M_{500} is obtained from the M-L relation, L_{500} is estimated in an iterative fashion with M_{500} (as it is weakly dependent on R_{500}). For a general idea on how the BOXSZ cluster sample is distributed relative to the general cluster population, the BOXSZ sample clusters are marked in Figure A.2, where the parameters are obtained from the MCXC catalog. While BOXSZ has very full coverage of the most massive, high redshift clusters known (thanks to the complete MACS high-redshift sample), the completeness of this coverage quickly tapers at low redshifts.

A new all-sky X-ray survey is scheduled to launch in 2014: the extended ROentgen Survey with an Imaging Telescope Array (eROSITA). eROSITA will perform the second
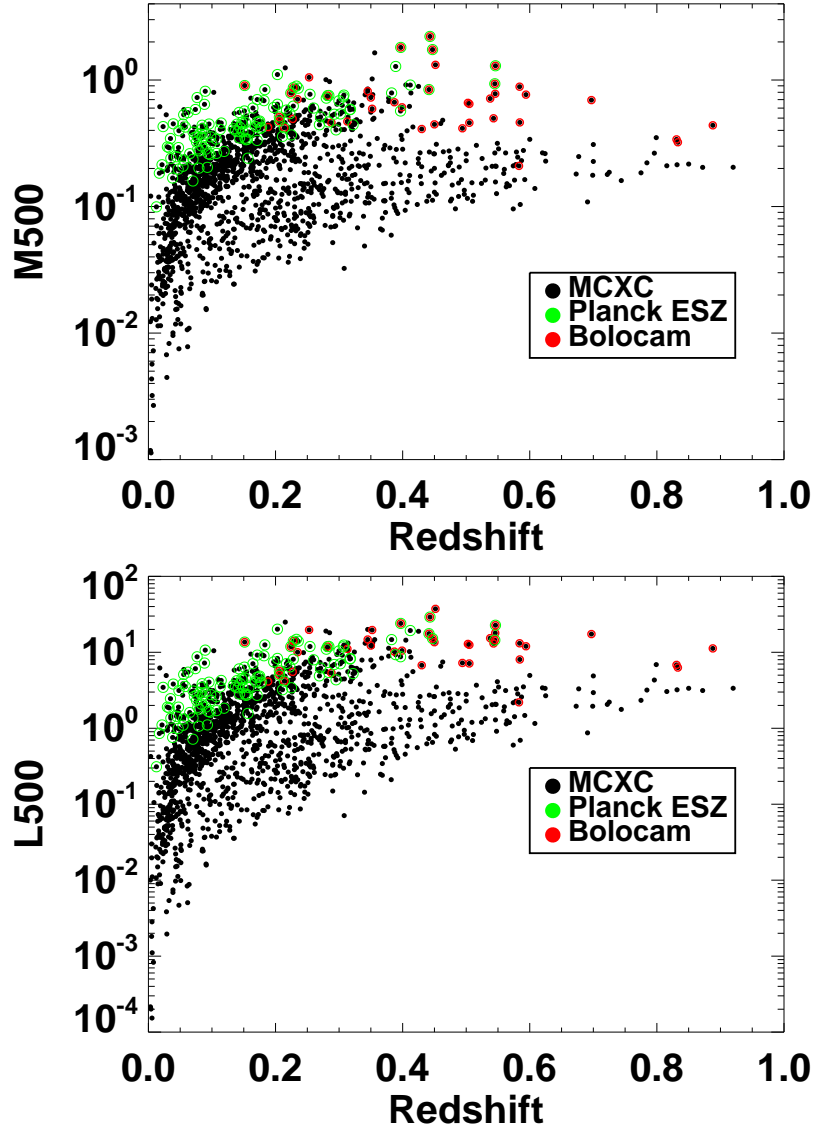
Figure A.2 M_{500} (upper) and L_{500} (lower) measurements given in the Meta-Catalogue of X-ray detected Clusters (MCXC), Piffaretti et al. [221] (black dots), which includes almost all of the confirmed X-ray detected galaxy clusters. While M_{500} values for a small fraction of the clusters, mostly the MACS cluster sample, are available, the bulk of the M_{500} values are estimated from the L-M relation given in Arnaud et al. [15]. Intrinsic scatter is not included, and therefore these values are more correlated than they would be if the parameters had been measured using standard X-ray techniques. Overplotted are the BOXSZ cluster sample (open green circles) and Planck Collaboration et al. [223, ESZ] early release cluster sample (smaller, open red circles) but retaining the L_{500} and M_{500} given in the MCXC catalog. As can be seen, the ESZ catalog covers a much lower redshift than the BOXSZ sample, and there are quite a few X-ray luminous clusters that are undetected with the SZE.

all-sky survey in the soft X-ray band (0.5-2.0 keV), and it will be the first ever hard X-ray (2.0-10.0 keV) survey of the sky. The survey will take 4 years, and it will be 20 times more sensitive than ROSAT. What is most amazing is that eROSITA will discover all massive galaxy clusters away from the Galactic plane, which the team estimates to be between 50-100 thousand galaxy clusters out to $z \geq 1$ (Merloni et al. [183]).

X-ray selected cluster catalogs have also been derived for targeted observations at other wavelengths. One such example is the Local Cluster Substructure Survey (LoCuSS,Smith et al. [262]), which aims to calibrate masses across X-ray, SZE, and weak- and strong-lensing. The original sample consisted of $\sim$12 clusters, selected to be very bright ($L_x \geq 8 \times 10^{44}$erg/s, 0.1-2.4 keV) and lie in a narrow redshift slice, $0.17 \leq z \leq 0.25$, where gravitational lensing is optimized. Ultimately, LoCuSS hopes to observe over 100 galaxy clusters. Okabe et al. [207] perform a weak-lensing analysis on 30 clusters. Marrone et al. [171] measure Y_{SZ} scaling relations using the Sunyaev-Zel'dovich Array (SZA) and strong-lensing measurement for 14 LoCuSS clusters, and Marrone et al. [172] measure the Y_{SZ} weak-lensing mass scaling relations with 18 LoCuSS clusters.

Accurate mass-profile calibration for a representative sample of clusters is one of the primary goals of the Cluster Lensing And Supernova survey with Hubble (CLASH, Postman et al. [233]). The catalog is built around a 524-orbit multi-cycle treasury *Hubble Space Telescope* (HST) program observing a total of 25 galaxy clusters in 16 filters ranging from IR to UV. Twenty clusters are X-ray-selected, and the remaining 5 clusters were chosen specifically for being known strong lenses (Postman et al. [233]). Many of the clusters were chosen to be massive and dynamically relaxed, with 16 clusters chosen from the Allen et al. [6] sample of 20 clusters. The CLASH program's scientific goals have compelled the collaboration to calibrate their data using a wide variety of observational probes, including: weak lensing, X-ray, and the SZE. All of the clusters have $T_X \geq 5$ keV and redshifts $z \sim 0.2$, which is compatible with the cluster parameter region that *Bolocam* is senstive to. This has led to a close *Bolocam*-CLASH collaborative effort, and the CLASH cluster catalog is entirely contained with the BOXSZ sample.
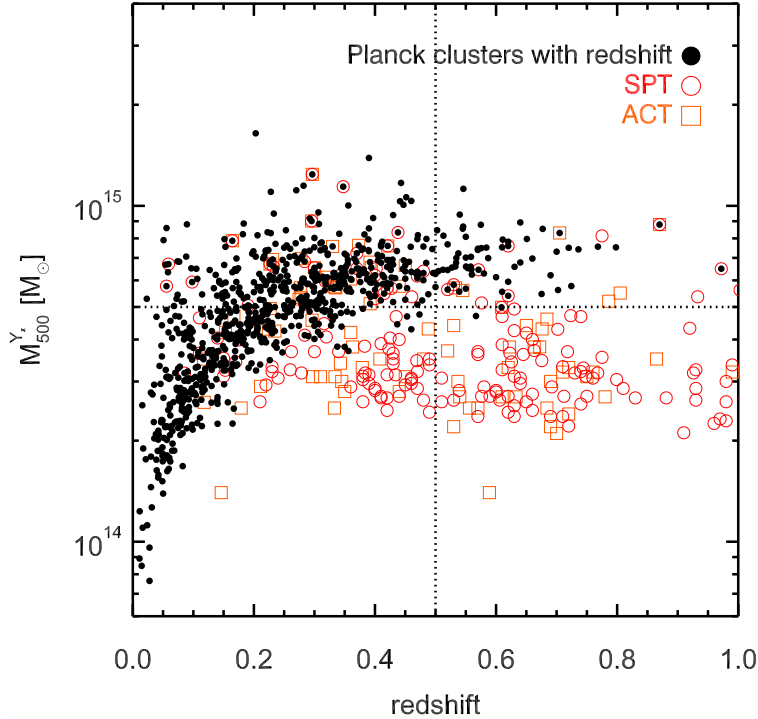
Figure A.3 Redshifts and Y_X-based mass estimates for the SPT (Williamson et al. [292]), ACT (Hasselfield et al. [113]), and Planck (Planck Collaboration et al. [228]) cluster catalogs. As can be seen for high-redshift clusters, detection is fairly independent with redshift. Figure taken from Planck Collaboration et al. [228].

A.3   SZE Catalogs: Planck, ACT, and SPT

We are positioned at an age where copious, high-quality SZE data are just beginning to come available. Three main SZE surveys have come online during the last several years: the South Pole Telescope (SPT), the Atacama Cosmology Telescope (ACT), and the Planck satellite. The resolution of the ground based instruments, similar to *Bolocam*, complement the spatial coverage of Planck satellite observations. Mass estimates and redshift measurements for all three of these SZE surveys is plotted in Figure A.3.

The SPT SZE focal plane contains 960 detectors, formed out of six detector segments, which are individually senstive to 100 GHz, 150 GHz, and 220 GHz, and each detector has a FWHM PSF of 1.6′, 1.2′, and 1.0′, respectively (Carlstrom et al. [49]). The first SPT survey mapped 720 deg², identified 224 cluster candidates, 158 of which were confirmed clusters, and 138 of these were first detected with SPT (Reichardt et al. [242]). The median redshift for the sample is $\langle z \rangle = 0.57$, and it attains a survey depth of 18 μK_{CMB}-arcmin. The final

SPT survey has mapped 2500 deg^2 (Williamson et al. [292]) and has reached a comparable depth to the first SPT survey, with a full list of cluster candidates and detected clusters yet to be published.

ACT is a ground-based SZE survey instrument quite similar to SPT. It too has three bands, 148 GHz, 218 GHz, and 277 GHz, with FWHM PSFs of $1.4'$, $1.0'$, and $0.9'$, respectively (Swetz et al. [272]). ACT has surveyed approximately 1000 deg^2, consisting of a 455 deg^2 survey (36μK deep, Marriage et al. [170]), and a 504 deg^2 survey ($\sim59\mu$K deep, Hasselfield et al. [113]). The instrument has detected 91 optically confirmed clusters at a median redshift of $\langle z \rangle = 0.44$, and ~30 of these clusters are new discoveries. Both SPT and ACT have undergone major upgrades in recent years and are currently undergoing ambitious observation campaigns. We can expect these catalogs to grow several-fold in the coming years.

The Planck satellite recently released its SZE-selected cluster catalog, covering an area of $\sim35,000$ deg^2, and containing 1227 cluster candidates, 683 of which were previously known and 178 of which are new cluster detections, which have been confirmed Planck Collaboration et al. [228]. The 143 GHz band of the Planck satellite has a FWHM sensitivity of $\sim7'$. Three different algorithms were used for selection (Herranz et al. [115], Melin et al. [181], Carvalho et al. [51]) which utilize spectral information from all spectral bands of the Planck satellite, from 100 GHz to 857 GHz, and all clusters with S/N> 4.5 were selected. The clusters have a median redshift of $\langle z \rangle \approx 0.15$, although there is significant coverage out to redshift 1.0.

Bibliography

[1] Abell, G. O. 1958, Astrophys. J. Suppl., 3, 211

[2] Abell, G. O., Corwin, Jr., H. G., & Olowin, R. P. 1989, Astrophys. J. Suppl., 70, 1

[3] Ackermann, M., Ajello, M., Allafort, A., et al. 2013, Science, 339, 807

[4] Ahmed, Z., Akerib, D. S., Armengaud, E., et al. 2011, Phys. Rev. D, 84, 011102

[5] Allen, S. W., & Fabian, A. C. 1998, Mon. Not. R. Astron. Soc., 297, L63

[6] Allen, S. W., Rapetti, D. A., Schmidt, R. W., et al. 2008, Mon. Not. R. Astron. Soc., 383, 879

[7] Alpher, R. A., Bethe, H., & Gamow, G. 1948, Physical Review, 73, 803

[8] Andersson, K., Benson, B. A., Ade, P. A. R., et al. 2011, Astrophys. J., 738, 48

[9] Angloher, G., Bauer, M., Bavykina, I., et al. 2012, European Physical Journal C, 72, 1971

[10] Applegate, D. E., von der Linden, A., Kelly, P. L., et al. 2012, ArXiv e-prints

[11] Arlen, T., Aune, T., Beilicke, M., et al. 2012, Astrophys. J., 757, 123

[12] Arnaud, M., & Evrard, A. E. 1999, Mon. Not. R. Astron. Soc., 305, 631

[13] Arnaud, M., Pointecouteau, E., & Pratt, G. W. 2005, Astron. Astrophys., 441, 893

[14] —. 2007, Astron. Astrophys., 474, L37

[15] Arnaud, M., Pratt, G. W., Piffaretti, R., et al. 2010, Astron. Astrophys., 517, A92

[16] Ascasibar, Y., & Markevitch, M. 2006, Astrophys. J., 650, 102

[17] Austermann, J. E., Aird, K. A., Beall, J. A., et al. 2012, in —, Vol. 8452, Society of Photo-Optical Instrumentation Engineers (SPIE) Conference Series, ed. W.S. Holland, & J. Zmuidzinas, 84521E

[18] Bartelmann, M., & Schneider, P. 2001, Phys. Reports, 340, 291

[19] Battaglia, N., Bond, J. R., Pfrommer, C., & Sievers, J. L. 2012, Astrophys. J., 758, 74

[20] Battaglia, N., Bond, J. R., Pfrommer, C., Sievers, J. L., & Sijacki, D. 2010, Astrophys. J., 725, 91

[21] Bautz, M. W., Miller, E. D., Sanders, J. S., et al. 2009, Pub. Astronom. Jap., 61, 1117

[22] Bennett, C. L., Kogut, A., Hinshaw, G., et al. 1994, Astrophys. J., 436, 423

[23] Bennett, C. L., Bay, M., Halpern, M., et al. 2003, Astrophys. J., 583, 1

[24] Benoît, A., Ade, P., Amblard, A., et al. 2003, Astron. Astrophys., 399, L25

[25] Benson, B. A., de Haan, T., Dudley, J. P., et al. 2013, Astrophys. J., 763, 147

[26] Bernabei, R., Belli, P., Cappella, F., et al. 2010, European Physical Journal C, 67, 39

[27] Bertone, G., Hooper, D., & Silk, J. 2005, Phys. Reports, 405, 279

[28] Bertschinger, E. 1985, Astrophys. J. Suppl., 58, 39

[29] —. 1998, ARA&A, 36, 599

[30] Bevington, P. R., & Robinson, D. K. 1992, Data reduction and error analysis for the physical sciences (New York, NY, USA: McGraw-Hill, 2nd ed.)

[31] Birkinshaw, M., Gull, S. F., & Northover, K. J. E. 1978, Nature, 275, 40

[32] —. 1978, Mon. Not. R. Astron. Soc., 185, 245

[33] Bock, J. J., Chen, D., Mauskopf, P. D., & Lange, A. E. 1995, Space Science Rev., 74, 229

[34] Boggess, N. W., Mather, J. C., Weiss, R., et al. 1992, Astrophys. J., 397, 420

[35] Böhringer, H., & Werner, N. 2010, Astron. Astrophys. Rev., 18, 127

[36] Böhringer, H., Schuecker, P., Guzzo, L., et al. 2004, Astron. Astrophys., 425, 367

[37] Bonamente, M., Joy, M., LaRoque, S. J., et al. 2008, Astrophys. J., 675, 106

[38] Bond, J. R., Cole, S., Efstathiou, G., & Kaiser, N. 1991, Astrophys. J., 379, 440

[39] Bond, J. R., Efstathiou, G., & Silk, J. 1980, Physical Review Letters, 45, 1980

[40] Bond, J. R., & Szalay, A. S. 1983, Astrophys. J., 274, 443

[41] Borgani, S., Fabjan, D., Tornatore, L., et al. 2008, Space Science Rev., 134, 379

[42] Bower, R. G., Lucey, J. R., & Ellis, R. S. 1992, Mon. Not. R. Astron. Soc., 254, 589

[43] Bryan, G. L. 2000, Astrophys. J. Lett., 544, L1

[44] Bryan, G. L., & Norman, M. L. 1998, Astrophys. J., 495, 80

[45] Buote, D. A., & Humphrey, P. J. 2012, Mon. Not. R. Astron. Soc., 421, 1399

[46] Burenin, R. A., Vikhlinin, A., Hornstrup, A., et al. 2007, Astrophys. J. Suppl., 172, 561

[47] Burns, J. O., Skillman, S. W., & O'Shea, B. W. 2010, Astrophys. J., 721, 1105

[48] Carlstrom, J. E., Joy, M., & Grego, L. 1996, Astrophys. J. Lett., 461, L59

[49] Carlstrom, J. E., Ade, P. A. R., Aird, K. A., et al. 2011, Pub. Astronom. Pac., 123, 568

[50] Carroll, S. M. 2004, Spacetime and geometry. An introduction to general relativity (San Francisco, CA, USA: Addison Wesley)

[51] Carvalho, P., Rocha, G., & Hobson, M. P. 2009, Mon. Not. R. Astron. Soc., 393, 681

[52] Cavaliere, A., & Fusco-Femiano, R. 1976, Astron. Astrophys., 49, 137

[53] Chase, S. T., Joseph, R. D., Robertson, N. A., & Ade, P. A. R. 1987, Mon. Not. R. Astron. Soc., 225, 171

[54] Chervenak, J. A., Irwin, K. D., Grossman, E. N., et al. 1999, Applied Physics Letters, 74, 4043

[55] Chluba, J., Nagai, D., Sazonov, S., & Nelson, K. 2012, Mon. Not. R. Astron. Soc., 426, 510

[56] Cholis, I., Dobler, G., Finkbeiner, D. P., Goodenough, L., & Weiner, N. 2009, Phys. Rev. D, 80, 123518

[57] Coe, D., Fuselier, E., Benítez, N., et al. 2008, Astrophys. J., 681, 814

[58] Condon, J. J., Cotton, W. D., Greisen, E. W., et al. 1998, Astron. J, 115, 1693

[59] Conroy, C., Wechsler, R. H., & Kravtsov, A. V. 2007, Astrophys. J., 668, 826

[60] Copeland, E. J., Sami, M., & Tsujikawa, S. 2006, International Journal of Modern Physics D, 15, 1753

[61] Crain, R. A., Eke, V. R., Frenk, C. S., et al. 2007, Mon. Not. R. Astron. Soc., 377, 41

[62] Day, P. K., LeDuc, H. G., Mazin, B. A., Vayonakis, A., & Zmuidzinas, J. 2003, Nature, 425, 817

[63] de Bernardis, P., Ade, P. A. R., Bock, J. J., et al. 2000, Nature, 404, 955

[64] De Grandi, S., & Molendi, S. 2002, Astrophys. J., 567, 163

[65] de Korte, P. A. J., Beyer, J., Deiker, S., et al. 2003, Review of Scientific Instruments, 74, 3807

[66] Devlin, M. J., Ade, P. A. R., Aretxaga, I., et al. 2009, Nature, 458, 737

[67] Dicke, R. H., Peebles, P. J. E., Roll, P. G., & Wilkinson, D. T. 1965, Astrophys. J., 142, 414

[68] Dicker, S. R., Korngut, P. M., Mason, B. S., et al. 2008, in —, Vol. 7020, Society of Photo-Optical Instrumentation Engineers (SPIE) Conference Series, ed. W. D. Duncan, W. S. Holland, S. Withington, & J. Zmuidzinas, 702005

[69] Dobbs, M., Halverson, N. W., Ade, P. A. R., et al. 2006, New Astron. Rev., 50, 960

[70] Dolag, K., Vazza, F., Brunetti, G., & Tormen, G. 2005, Mon. Not. R. Astron. Soc., 364, 753

[71] Ebeling, H., Barrett, E., Donovan, D., et al. 2007, Astrophys. J. Lett., 661, L33

[72] Ebeling, H., Edge, A. C., Allen, S. W., et al. 2000, Mon. Not. R. Astron. Soc., 318, 333

[73] Ebeling, H., Edge, A. C., Fabian, A. C., et al. 1997, Astrophys. J. Lett., 479, L101

[74] Ebeling, H., Edge, A. C., & Henry, J. P. 2001, Astrophys. J., 553, 668

[75] Ebeling, H., Edge, A. C., Mantz, A., et al. 2010, Mon. Not. R. Astron. Soc., 407, 83

[76] Eddington, A. S. 1913, Mon. Not. R. Astron. Soc., 73, 359

[77] Einasto, J. 1969, Trudy Inst. Astrofiz. Alma-Ata, 5, 97

[78] —. 1969, Astrofizika, 5, 137

[79] Einasto, J., & Haud, U. 1989, Astron. Astrophys., 223, 89

[80] Einstein, A. 1905, Annalen der Physik, 322, 891

[81] Eisenstein, D. J., & Hu, W. 1999, Astrophys. J., 511, 5

[82] Eke, V. R., Navarro, J. F., & Frenk, C. S. 1998, Astrophys. J., 503, 569

[83] Evrard, A. E. 1990, Astrophys. J., 363, 349

[84] Evrard, A. E., Bialek, J., Busha, M., et al. 2008, Astrophys. J., 672, 122

[85] Fabian, A. C., Hu, E. M., Cowie, L. L., & Grindlay, J. 1981, Astrophys. J., 248, 47

[86] Fabian, A. C., Willingale, R., Pye, J. P., Murray, S. S., & Fabbiano, G. 1980, Mon. Not. R. Astron. Soc., 193, 175

[87] Fabjan, D., Borgani, S., Rasia, E., et al. 2011, Mon. Not. R. Astron. Soc., 416, 801

[88] Finoguenov, A., Jones, C., Böhringer, H., & Ponman, T. J. 2002, Astrophys. J., 578, 74

[89] Finoguenov, A., Ponman, T. J., Osmond, J. P. F., & Zimer, M. 2007, Mon. Not. R. Astron. Soc., 374, 737

[90] Fixsen, D. J., & Mather, J. C. 2002, Astrophys. J., 581, 817

[91] Fixsen, D. J., Kogut, A., Levin, S., et al. 2011, Astrophys. J., 734, 5

[92] Flaugher, B., & DES Collaboration. 2013, in —, Vol. 221, American Astronomical Society Meeting Abstracts, 335.02

[93] Freedman, W. L. 2000, Phys. Reports, 333, 13

[94] Friedmann, A. 1922, Zeitschrift fur Physik, 10, 377

[95] Fukuda, Y., Hayakawa, T., Ichihara, E., et al. 1998, Physical Review Letters, 81, 1158

[96] Furlanetto, S. R., & Loeb, A. 2004, Astrophys. J., 611, 642

[97] George, M. R., Fabian, A. C., Sanders, J. S., Young, A. J., & Russell, H. R. 2009, Mon. Not. R. Astron. Soc., 395, 657

[98] Gioia, I. M., & Luppino, G. A. 1994, Astrophys. J. Suppl., 94, 583

[99] Gladders, M. D., & Yee, H. K. C. 2000, Astron. J, 120, 2148

[100] Glenn, J., Bock, J. J., Ade, P. A., et al. 1998, in SPIE Conference Series, ed. T. G. Phillips, Vol. 3357, 326–334

[101] Golwala, S. R., Bockstiegel, C., Brugger, S., et al. 2012, in —, Vol. 8452, Society of Photo-Optical Instrumentation Engineers (SPIE) Conference Series, ed. W.S. Holland, & J. Zmuidzinas, 845205

[102] Gonzalez, A. H., Zaritsky, D., & Zabludoff, A. I. 2007, Astrophys. J., 666, 147

[103] Gott, J. R., & Slepian, Z. 2011, MNRAS, 416, 907

[104] Gottlöber, S., & Yepes, G. 2007, Astrophys. J., 664, 117

[105] Grego, L., Carlstrom, J. E., Joy, M. K., et al. 2000, Astrophys. J., 539, 39

[106] Griffin, M. J., & Orton, G. S. 1993, Icarus, 105, 537

[107] Gull, S. F., & Northover, K. J. E. 1976, Nature, 263, 572

[108] Guth, A. H. 1981, Phys. Rev. D, 23, 347

[109] Haig, D. J., Ade, P. A. R., Aguirre, J. E., et al. 2004, in —, Vol. 5498, Society of Photo-Optical Instrumentation Engineers (SPIE) Conference Series, ed. C. M. Bradford, 78–94

[110] Hanany, S., Ade, P., Balbi, A., et al. 2000, Astrophys. J. Lett., 545, L5

[111] Hao, J., McKay, T. A., Koester, B. P., et al. 2010, Astrophys. J. Suppl., 191, 254

[112] Hartley, W. G., Gazzola, L., Pearce, F. R., Kay, S. T., & Thomas, P. A. 2008, Mon. Not. R. Astron. Soc., 386, 2015

[113] Hasselfield, M., Hilton, M., Marriage, T. A., et al. 2013, ArXiv e-prints

[114] Henry, J. P., & Arnaud, K. A. 1991, Astrophys. J., 372, 410

[115] Herranz, D., Sanz, J. L., Hobson, M. P., et al. 2002, Mon. Not. R. Astron. Soc., 336, 1057

[116] High, F. W., Stalder, B., Song, J., et al. 2010, Astrophys. J., 723, 1736

[117] Hill, R. S., Weiland, J. L., Odegard, N., et al. 2009, Astrophys. J. Suppl., 180, 246

[118] Hoekstra, H. 2003, Mon. Not. R. Astron. Soc., 339, 1155

[119] Hogg, D. W. 1999, ArXiv Astrophysics e-prints

[120] Holder, G. 2012, ArXiv e-prints

[121] Holzapfel, W. L., Wilbanks, T. M., Ade, P. A. R., et al. 1997, Astrophys. J., 479, 17

[122] Hu, W., & Dodelson, S. 2002, ARA&A, 40, 171

[123] Hubble, E. 1929, Proceedings of the National Academy of Science, 15, 168

[124] Irwin, K. D., & Hilton, G. C. 2005, Transition-edge sensors (Spring Berlin/Heidelberg), 81–97

[125] Itoh, N., Kohyama, Y., & Nozawa, S. 1998, Astrophys. J., 502, 7

[126] Jee, M. J., & Tyson, J. A. 2009, Astrophys. J., 691, 1337

[127] Jee, M. J., Dawson, K. S., Hoekstra, H., et al. 2011, Astrophys. J., 737, 59

[128] Jeltema, T. E., Hallman, E. J., Burns, J. O., & Motl, P. M. 2008, Astrophys. J., 681, 167

[129] Jenkins, A., Frenk, C. S., White, S. D. M., et al. 2001, Mon. Not. R. Astron. Soc., 321, 372

[130] Jimenez, R., Bernardi, M., Haiman, Z., Panter, B., & Heavens, A. F. 2007, Astrophys. J., 669, 947

[131] Jing, Y. P., Suto, Y., & Mo, H. J. 2007, Astrophys. J., 657, 664

[132] Jones, M., Saunders, R., Alexander, P., et al. 1993, Nature, 365, 320

[133] Jullo, E., Kneib, J.-P., Limousin, M., et al. 2007, New Journal of Physics, 9, 447

[134] Jungman, G., Kamionkowski, M., & Griest, K. 1996, Phys. Reports, 267, 195

[135] Kaastra, J. S., & Mewe, R. 1993, Astron. Astrophys. Suppl., 97, 443

[136] Kaiser, N. 1986, Mon. Not. R. Astron. Soc., 222, 323

[137] Kartaltepe, J. S., Ebeling, H., Ma, C. J., & Donovan, D. 2008, Mon. Not. R. Astron. Soc., 389, 1240

141

[138] Keisler, R., Reichardt, C. L., Aird, K. A., et al. 2011, Astrophys. J., 743, 28

[139] Kelly, B. C. 2007, Astrophys. J., 665, 1489

[140] Khedekar, S., Churazov, E., Kravtsov, A., et al. 2013, Mon. Not. R. Astron. Soc., 431, 954

[141] Kiviranta, M., Seppä, H., van der Kuur, J., & de Korte, P. 2002, Low Temperature Detectors, 605, 295

[142] Koester, B. P., McKay, T. A., Annis, J., et al. 2007, Astrophys. J., 660, 239

[143] Korngut, P. M., Dicker, S. R., Reese, E. D., et al. 2011, Astrophys. J., 734, 10

[144] Krause, E., Pierpaoli, E., Dolag, K., & Borgani, S. 2012, Mon. Not. R. Astron. Soc., 419, 1766

[145] Kravtsov, A. V., & Borgani, S. 2012, ARA&A, 50, 353

[146] Kravtsov, A. V., Klypin, A., & Hoffman, Y. 2002, Astrophys. J., 571, 563

[147] Kravtsov, A. V., Nagai, D., & Vikhlinin, A. A. 2005, Astrophys. J., 625, 588

[148] Kravtsov, A. V., Vikhlinin, A., & Nagai, D. 2006, Astrophys. J., 650, 128

[149] Lahav, O., Lilje, P. B., Primack, J. R., & Rees, M. J. 1991, Mon. Not. R. Astron. Soc., 251, 128

[150] Lake, G. 1980, in IAU Symposium, Vol. 92, Objects of High Redshift, ed. G. O. Abell & P. J. E. Peebles, 305–312

[151] LaRoque, S. J., Bonamente, M., Carlstrom, J. E., et al. 2006, Astrophys. J., 652, 917

[152] Larson, R. B. 1969, Mon. Not. R. Astron. Soc., 145, 271

[153] Lau, E. T., Kravtsov, A. V., & Nagai, D. 2009, Astrophys. J., 705, 1129

[154] Lau, E. T., Nagai, D., Kravtsov, A. V., & Zentner, A. R. 2011, Astrophys. J., 734, 93

[155] Lemaître, G. 1927, Annales de la Societe Scietifique de Bruxelles, 47, 49

[156] —. 1931, Nature, 127, 706

[157] Lemson, G., & Kauffmann, G. 1999, Mon. Not. R. Astron. Soc., 302, 111

[158] Liedahl, D. A., Osterheld, A. L., & Goldstein, W. H. 1995, Astrophys. J. Lett., 438, L115

[159] Lightman, A. P., & Schechter, P. L. 1990, Astrophys. J. Suppl., 74, 831

[160] Lin, Y.-T., Mohr, J. J., & Stanford, S. A. 2003, Astrophys. J., 591, 749

[161] Lin, Y.-T., Stanford, S. A., Eisenhardt, P. R. M., et al. 2012, Astrophys. J. Lett., 745, L3

[162] Ma, C.-J., Ebeling, H., & Barrett, E. 2009, Astrophys. J. Lett., 693, L56

[163] Mahdavi, A., Hoekstra, H., Babul, A., et al. 2013, Astrophys. J., 767, 116

[164] —. 2007, Astrophys. J., 664, 162

[165] Mantz, A., Allen, S. W., Ebeling, H., & Rapetti, D. 2008, Mon. Not. R. Astron. Soc., 387, 1179

[166] Mantz, A., Allen, S. W., Ebeling, H., Rapetti, D., & Drlica-Wagner, A. 2010, Mon. Not. R. Astron. Soc., 406, 1773

[167] Markevitch, M., Forman, W. R., Sarazin, C. L., & Vikhlinin, A. 1998, Astrophys. J., 503, 77

[168] Markevitch, M., Gonzalez, A. H., David, L., et al. 2002, Astrophys. J. Lett., 567, L27

[169] Markevitch, M., & Vikhlinin, A. 2007, Phys. Reports, 443, 1

[170] Marriage, T. A., Acquaviva, V., Ade, P. A. R., et al. 2011, Astrophys. J., 737, 61

[171] Marrone, D. P., Smith, G. P., Richard, J., et al. 2009, Astrophys. J. Lett., 701, L114

143

[172] Marrone, D. P., Smith, G. P., Okabe, N., et al. 2012, Astrophys. J., 754, 119

[173] Mather, J. C., Fixsen, D. J., Shafer, R. A., Mosier, C., & Wilkinson, D. T. 1999, Astrophys. J., 512, 511

[174] Mathiesen, B. F., & Evrard, A. E. 2001, Astrophys. J., 546, 100

[175] Maughan, B. J., Giles, P. A., Randall, S. W., Jones, C., & Forman, W. R. 2012, Mon. Not. R. Astron. Soc., 421, 1583

[176] Maughan, B. J., Jones, C., Jones, L. R., & Van Speybroeck, L. 2007, Astrophys. J., 659, 1125

[177] Maughan, B. J., Jones, L. R., Pierre, M., et al. 2008, Mon. Not. R. Astron. Soc., 387, 998

[178] Mauskopf, P. D., Bock, J. J., del Castillo, H., Holzapfel, W. L., & Lange, A. E. 1997, Appl. Optics, 36, 765

[179] Mazzotta, P., Rasia, E., Moscardini, L., & Tormen, G. 2004, Mon. Not. R. Astron. Soc., 354, 10

[180] Medezinski, E., Umetsu, K., Nonino, M., et al. 2013, ArXiv e-prints

[181] Melin, J.-B., Bartlett, J. G., & Delabrouille, J. 2006, Astron. Astrophys., 459, 341

[182] Menanteau, F., González, J., Juin, J.-B., et al. 2010, Astrophys. J., 723, 1523

[183] Merloni, A., Predehl, P., Becker, W., et al. 2012, ArXiv e-prints

[184] Merritt, D., Graham, A. W., Moore, B., Diemand, J., & Terzić, B. 2006, Astron. J, 132, 2685

[185] Merten, J., Cacciato, M., Meneghetti, M., Mignone, C., & Bartelmann, M. 2009, Astron. Astrophys., 500, 681

[186] Mewe, R., Gronenschild, E. H. B. M., & van den Oord, G. H. J. 1985, Astron. Astrophys. Suppl., 62, 197

[187] Meyer, S. S., Jeffries, A. D., & Weiss, R. 1983, Astrophys. J. Lett., 271, L1

[188] Mohr, J. J., Fabricant, D. G., & Geller, M. J. 1993, Astrophys. J., 413, 492

[189] Molnar, S. M., Hearn, N., Haiman, Z., et al. 2009, Astrophys. J., 696, 1640

[190] Molnar, S. M., Hearn, N. C., & Stadel, J. G. 2012, Astrophys. J., 748, 45

[191] Morandi, A., Limousin, M., Sayers, J., et al. 2012, Mon. Not. R. Astron. Soc., 425, 2069

[192] Mroczkowski, T. 2011, Astrophys. J. Lett., 728, L35

[193] —. 2012, Astrophys. J. Lett., 746, L29

[194] Mroczkowski, T., Dicker, S., Sayers, J., et al. 2012, Astrophys. J., 761, 47

[195] Muñoz-Cuartas, J. C., Macciò, A. V., Gottlöber, S., & Dutton, A. A. 2011, Mon. Not. R. Astron. Soc., 411, 584

[196] Muchovej, S., Mroczkowski, T., Carlstrom, J. E., et al. 2007, Astrophys. J., 663, 708

[197] Nagai, D. 2006, Astrophys. J., 650, 538

[198] Nagai, D., Kravtsov, A. V., & Vikhlinin, A. 2007, Astrophys. J., 668, 1

[199] Nagai, D., & Lau, E. T. 2011, Astrophys. J. Lett., 731, L10

[200] Nagai, D., Vikhlinin, A., & Kravtsov, A. V. 2007, Astrophys. J., 655, 98

[201] Navarro, J. F., Frenk, C. S., & White, S. D. M. 1995, Mon. Not. R. Astron. Soc., 275, 720

[202] —. 1996, Astrophys. J., 462, 563

[203] Navarro, J. F., Hayashi, E., Power, C., et al. 2004, Mon. Not. R. Astron. Soc., 349, 1039

[204] Nelson, K., Rudd, D. H., Shaw, L., & Nagai, D. 2012, Astrophys. J., 751, 121

[205] Niemack, M. D., Ade, P. A. R., Aguirre, J., et al. 2010, in —, Vol. 7741, Society of Photo-Optical Instrumentation Engineers (SPIE) Conference Series, ed. W.S. Holland, & J. Zmuidzinas, 77411S

[206] Nozawa, S., Itoh, N., Kawana, Y., & Kohyama, Y. 2000, Astrophys. J., 536, 31

[207] Okabe, N., Takada, M., Umetsu, K., Futamase, T., & Smith, G. P. 2010, Pub. Astronom. Jap., 62, 811

[208] Oort, J. H. 1932, Bul. Astron. Instit. Netherlands, 6, 249

[209] Page, L., Jackson, C., Barnes, C., et al. 2003, Astrophys. J., 585, 566

[210] Palaio, N. P., Rodder, M., Haller, E. E., & Kreysa, E. 1983, International Journal of Infrared and Millimeter Waves, 4, 933

[211] Pariiskii, Y. N. 1972, Astron. Zhurn., 49, 1322

[212] —. 1973, Sov. Astron., 16, 1048

[213] Peacock, J. A. 1999, Cosmological Physics (Cambridge, UK: Cambridge University Press)

[214] Peebles, P. J. E. 1980, The large-scale structure of the universe (Princeton, N.J.: Princeton University Press)

[215] Peebles, P. J. E., & Yu, J. T. 1970, Astrophys. J., 162, 815

[216] Perlman, E. S., Horner, D. J., Jones, L. R., et al. 2002, Astrophys. J. Suppl., 140, 265

[217] Perlmutter, S., Aldering, G., Goldhaber, G., et al. 1999, Astrophys. J., 517, 565

[218] Peter, A. H. G., Rocha, M., Bullock, J. S., & Kaplinghat, M. 2012, ArXiv

[219] Peterson, J. R., & Fabian, A. C. 2006, Phys. Reports, 427, 1

[220] Peterson, J. R., Paerels, F. B. S., Kaastra, J. S., et al. 2001, Astron. Astrophys., 365, L104

[221] Piffaretti, R., Arnaud, M., Pratt, G. W., Pointecouteau, E., & Melin, J.-B. 2011, Astron. Astrophys., 534, A109

[222] Planck Collaboration, Ade, P. A. R., Aghanim, N., et al. 2011, Astron. Astrophys., 536, A1

[223] —. 2011, Astron. Astrophys., 536, A8

[224] —. 2011, Astron. Astrophys., 536, A11

[225] —. 2012, ArXiv e-prints

[226] —. 2013, ArXiv e-prints

[227] —. 2013, ArXiv e-prints

[228] —. 2013, ArXiv e-prints

[229] —. 2013, Astron. Astrophys., 550, A129

[230] —. 2013, Astron. Astrophys., 550, A131

[231] Pointecouteau, E., Arnaud, M., & Pratt, G. W. 2005, Astron. Astrophys., 435, 1

[232] Poole, G. B., Fardal, M. A., Babul, A., et al. 2006, Mon. Not. R. Astron. Soc., 373, 881

[233] Postman, M., Coe, D., Benítez, N., et al. 2012, Astrophys. J. Suppl., 199, 25

[234] Pratt, G. W., & Arnaud, M. 2002, Astron. Astrophys., 394, 375

[235] Pratt, G. W., Böhringer, H., Croston, J. H., et al. 2007, Astron. Astrophys., 461, 71

[236] Pratt, G. W., Croston, J. H., Arnaud, M., & Böhringer, H. 2009, Astron. Astrophys., 498, 361

[237] Pratt, G. W., Arnaud, M., Piffaretti, R., et al. 2010, Astron. Astrophys., 511, A85

[238] Press, W. H., & Schechter, P. 1974, Astrophys. J., 187, 425

[239] Rasia, E., Ettori, S., Moscardini, L., et al. 2006, Mon. Not. R. Astron. Soc., 369, 2013

[240] Readhead, A. C. S., Lawrence, C. R., Myers, S. T., et al. 1989, Astrophys. J., 346, 566

[241] Reichardt, C. L., Shaw, L., Zahn, O., et al. 2012, Astrophys. J., 755, 70

[242] Reichardt, C. L., Stalder, B., Bleem, L. E., et al. 2013, Astrophys. J., 763, 127

[243] Riess, A. G., Filippenko, A. V., Challis, P., et al. 1998, Astron. J, 116, 1009

[244] Rozo, E., Evrard, A. E., Rykoff, E. S., & Bartlett, J. G. 2012, ArXiv e-prints

[245] Rozo, E., Rykoff, E. S., Bartlett, J. G., & Evrard, A. E. 2012, ArXiv e-prints

[246] Rozo, E., Vikhlinin, A., & More, S. 2012, Astrophys. J., 760, 67

[247] Rudy, D. J., Muhleman, D. O., Berge, G. L., Jakosky, B. M., & Christensen, P. R. 1987, Icarus, 71, 159

[248] Ruhl, J., Ade, P. A. R., Carlstrom, J. E., et al. 2004, in —, Vol. 5498, Society of Photo-Optical Instrumentation Engineers (SPIE) Conference Series, ed. C. M. Bradford, 11–29

[249] Sakharov, A. D. 1966, Soviet Journal of Experimental and Theoretical Physics, 22, 241

[250] Sánchez, E., & DES Collaboration. 2010, Journal of Physics Conference Series, 259, 012080

[251] Sandell, G. 1994, Mon. Not. R. Astron. Soc., 271, 75

[252] Sayers, J. 2007, PhD thesis, California Institute of Technology

[253] Sayers, J., Czakon, N. G., Bridge, C., et al. 2012, Astrophys. J. Lett., 749, L15

[254] Sayers, J., Czakon, N. G., & Golwala, S. R. 2012, Astrophys. J., 744, 169

[255] Sayers, J., Golwala, S. R., Ameglio, S., & Pierpaoli, E. 2011, Astrophys. J., 728, 39

[256] Sayers, J., Czakon, N. G., Mantz, A., et al. 2013, Astrophys. J., 768, 177

[257] Sayers, J., Mroczkowski, T., Czakon, N. G., et al. 2013, Astrophys. J., 764, 152

[258] Sereno, M., & Zitrin, A. 2012, Mon. Not. R. Astron. Soc., 419, 3280

[259] Shaw, L. D., Nagai, D., Bhattacharya, S., & Lau, E. T. 2010, Astrophys. J., 725, 1452

[260] Simionescu, A., Allen, S. W., Mantz, A., et al. 2011, Science, 331, 1576

[261] Skielboe, A., Wojtak, R., Pedersen, K., Rozo, E., & Rykoff, E. S. 2012, Astrophys. J. Lett., 758, L16

[262] Smith, G. P., Kneib, J.-P., Smail, I., et al. 2005, Mon. Not. R. Astron. Soc., 359, 417

[263] Song, J., Zenteno, A., Stalder, B., et al. 2012, Astrophys. J., 761, 22

[264] Spergel, D. N., & Steinhardt, P. J. 2000, Physical Review Letters, 84, 3760

[265] Spitzer, Jr., L., & Greenstein, J. L. 1951, Astrophys. J., 114, 407

[266] Stanek, R., Evrard, A. E., Böhringer, H., Schuecker, P., & Nord, B. 2006, Astrophys. J., 648, 956

[267] Stanek, R., Rasia, E., Evrard, A. E., Pearce, F., & Gazzola, L. 2010, Astrophys. J., 715, 1508

[268] Stanford, S. A., Eisenhardt, P. R., & Dickinson, M. 1998, Astrophys. J., 492, 461

[269] Sun, M., Voit, G. M., Donahue, M., et al. 2009, Astrophys. J., 693, 1142

[270] Sunyaev, R. A., & Zel'dovich, Y. B. 1970, Astrophys. Space Sci., 7, 3

[271] —. 1972, Comments on Astrophysics and Space Physics, 4, 173

[272] Swetz, D. S., Ade, P. A. R., Amiri, M., et al. 2011, Astrophys. J. Suppl., 194, 41

[273] Tinker, J., Kravtsov, A. V., Klypin, A., et al. 2008, Astrophys. J., 688, 709

[274] Tinker, J. L., Robertson, B. E., Kravtsov, A. V., et al. 2010, Astrophys. J., 724, 878

[275] Tremaine, S., Gebhardt, K., Bender, R., et al. 2002, Astrophys. J., 574, 740

[276] Umetsu, K., Broadhurst, T., Zitrin, A., Medezinski, E., & Hsu, L.-Y. 2011, Astrophys. J., 729, 127

[277] Umetsu, K., Medezinski, E., Nonino, M., et al. 2012, Astrophys. J., 755, 56

[278] Vikhlinin, A., Kravtsov, A., Forman, W., et al. 2006, Astrophys. J., 640, 691

[279] Vikhlinin, A., Burenin, R. A., Ebeling, H., et al. 2009, Astrophys. J., 692, 1033

[280] Vikhlinin, A., Kravtsov, A. V., Burenin, R. A., et al. 2009, Astrophys. J., 692, 1060

[281] Voit, G. M. 2005, Reviews of Modern Physics, 77, 207

[282] Voit, G. M., & Bryan, G. L. 2001, Nature, 414, 425

[283] Voit, G. M., Bryan, G. L., Balogh, M. L., & Bower, R. G. 2002, Astrophys. J., 576, 601

[284] Wechsler, R. H., Bullock, J. S., Primack, J. R., Kravtsov, A. V., & Dekel, A. 2002, Astrophys. J., 568, 52

[285] Wechsler, R. H., Zentner, A. R., Bullock, J. S., Kravtsov, A. V., & Allgood, B. 2006, Astrophys. J., 652, 71

[286] Weiland, J. L., Odegard, N., Hill, R. S., et al. 2011, Astrophys. J. Suppl., 192, 19

[287] Wetzel, A. R., Cohn, J. D., White, M., Holz, D. E., & Warren, M. S. 2007, Astrophys. J., 656, 139

[288] White, D. A., Jones, C., & Forman, W. 1997, Mon. Not. R. Astron. Soc., 292, 419

[289] —. 1997, Mon. Not. R. Astron. Soc., 292, 419

[290] Wik, D. R., Sarazin, C. L., Ricker, P. M., & Randall, S. W. 2008, Astrophys. J., 680, 17

[291] Wilbanks, T. M., Ade, P. A. R., Fischer, M. L., Holzapfel, W. L., & Lange, A. E. 1994, Astrophys. J. Lett., 427, L75

[292] Williamson, R., Benson, B. A., High, F. W., et al. 2011, Astrophys. J., 738, 139

[293] Wilson, R. W., & Penzias, A. A. 1967, Science, 156, 1100

[294] Woody, D., Padin, S., Chauvin, E., et al. 2012, in —, Vol. 8444, Society of Photo-Optical Instrumentation Engineers (SPIE) Conference Series, ed. L.M. Stepp, R. Gilmozzi, & H.J. Hall, 84442M

[295] Wright, E. L. 1976, Astrophys. J., 210, 250

[296] —. 1979, Astrophys. J., 232, 348

[297] Wu, H.-Y., Hahn, O., Wechsler, R. H., Mao, Y.-Y., & Behroozi, P. S. 2013, Astrophys. J., 763, 70

[298] Yoon, J., Clarke, J., Gildemeister, J. M., et al. 2001, Applied Physics Letters, 78, 371

[299] Ysard, N., & Lagache, G. 2012, Astron. Astrophys., 547, A53

[300] Zemcov, M., Aguirre, J., Bock, J., et al. 2012, Astrophys. J., 749, 114

[301] Zhang, Y.-Y., Laganá, T. F., Pierini, D., et al. 2011, Astron. Astrophys., 535, A78

[302] Zhuravleva, I., Churazov, E., Kravtsov, A., et al. 2013, Mon. Not. R. Astron. Soc., 428, 3274

[303] Zitrin, A., Broadhurst, T., Barkana, R., Rephaeli, Y., & Benítez, N. 2011, Mon. Not. R. Astron. Soc., 410, 1939

[304] Zitrin, A., Broadhurst, T., Umetsu, K., et al. 2009, Mon. Not. R. Astron. Soc., 396, 1985

[305] Zitrin, A., Rephaeli, Y., Sadeh, S., et al. 2012, Mon. Not. R. Astron. Soc., 420, 1621

[306] ZuHone, J. A., Markevitch, M., & Johnson, R. E. 2010, Astrophys. J., 717, 908

[307] Zwicky, F. 1933, Helvetica Physica Acta, 6, 110

[308] Zwicky, F., Herzog, E., & Wild, P. 1968, Catalogue of galaxies and of clusters of galaxies (Pasadena, CA: California Institute of Technology)